Alma Mater Studiorum · Università di Bologna

Scuola di Scienze
Corso di Laurea Magistrale in Fisica del Sistema Terra

Bottom pressure time series study: the ANTARES deep sea observatory case

Relatore:
Prof. Nadia Pinardi

Presentata da:
Sara Zanella

Correlatore:
Prof. Annarita Margiotta
Dott. Stefano Cecchini

Sessione II
Anno Accademico 2015/2016

Alla mia nonna,
per il suo grande coraggio.

Al mio nonno,
che non ha mai perso la sua dignità.

Contents

Abstract

An analysis of bottom pressure variations in the Mediterranean Sea has been carried out. The main aim was to identify low frequency variability of the sea bottom pressure. The observed data have been collected by the ANTARES observatory, 40 km offshore Toulon, in an area of 180x180 m. Three observational time series have been analyzed: L1, L3 and L8 and a long time series, 1 January 2009-31 December 2013, has been constructed from the original ones. A despiking, an averaging over 30 minutes and a gap-filling procedure have been applied.

Two methods of detiding have been proposed, three days average and Doodson Filter, and successively a detrending. Comparison between an harmonic analysis and the Doodson filter shows the similarity of the results. For this reason the detrended and detided with Doodson Filter time series is used in the final part of the work. The detiding made possible to remove the high frequency signals from the bottom pressure and focalize on the residual low frequency signals.

A spectra of the detrended and detided time series showed that sub-seasonal and seasonal signals dominate with the addition of the Chandler wobble frequency of 14 months.

Sommario

Questo elaborato riguarda l'analisi delle variazioni di pressione sul fondale del Mar Mediterraneo. Il primo obiettivo era quello di identificare la variabilità a basse frequenze della pressione sul fondo. I dati osservati sono stati raccolti presso l'osservatorio ANTARES che si trova 40 km al largo di Tolone e ricopre un'area di 180x180 m. Sono state analizzate tre serie temporali, L1, L3 e L8, e da esse è stata ricostruita una serie temporale dall'1 gennaio 2009 al 31 dicembre 2013. Sono state applicate delle procedure di despiking, media su 30 minuti e gap-filling.

Sono stati proposti due metodi di detiding, una media su tre giorni e il filtro di Doodson. Successivamente è stato eseguito un detrending. Un confronto tra l'analisi armonica e il filtro di Doodson mostra una similarità nei risultati. Per questa ragione, per continuare il lavoro, è stata utilizzata la serie a cui era stato tolto il trend e le maree tramite il filtro di Doodson. Togliere le maree ha reso possibile la rimozione dei segnali ad alta frequenza per potersi focalizzare sui segnali rimasti a bassa frequenza.

Uno spettro sulla serie ha mostrato i segnali stagionali dominanti insieme alla cosiddetta Chandler wobble con una frequenza di 14 mesi.

Chapter 1

Introduction

1.1 The Global Ocean Observing System

The Global Ocean Observing System (GOOS) is a permanent global system, whose main aim is to provide description of the state of the oceans in order to see them no more as a multitude of seas but as a single entity and have a global view of the ocean system. GOOS coordinates observations, modelling and analysis of marine and ocean variables to support operational ocean services worldwide. It is designed to:

- Monitor, understand and predict weather and climate
- Describe and forecast the state of the ocean, including living resources
- Improve management of marine and coastal ecosystems and resources
- Mitigate damage from natural hazards and pollution
- Enable scientific research
- Protect life and property on coasts and at sea

GOOS is part of the larger GEOSS (Global Earth Observing System of Systems) and includes observing facilities on land, at sea, in the air and in outer space.

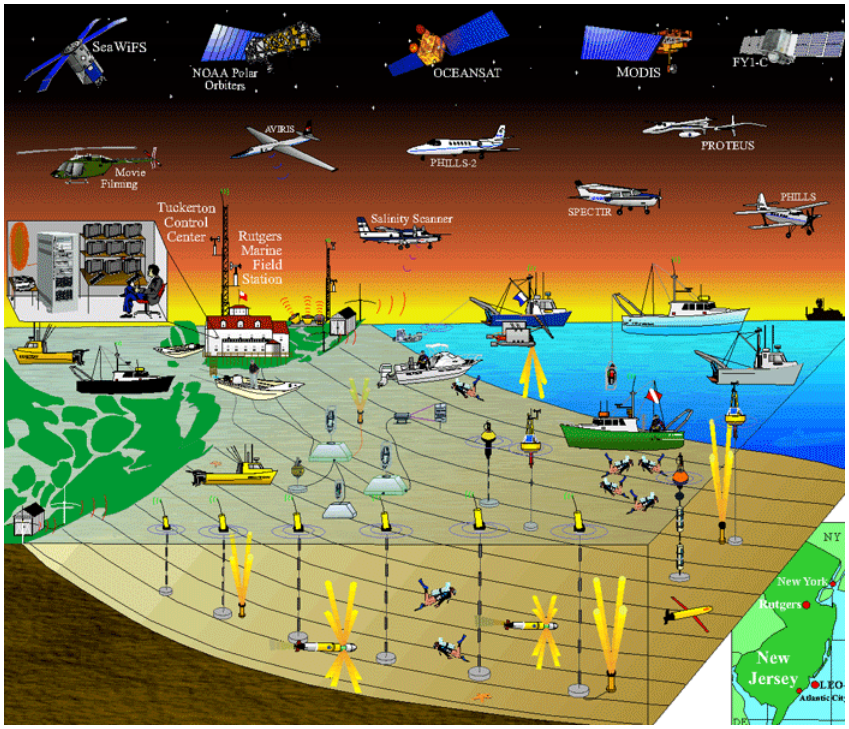

Figure 1.1: GOOS facilities (http://www.whoi.edu/).

These facilities are owned by the Member countries of WMO, which have the responsibility to agree with global schemes in order to make these observations available for each other.

The Joint Technical Commission for Oceanography and Marine Meteorology (JCOMM) stems from the need of a combination of marine meteorological and oceanographic observations. Before 1999 data managements and service prevision programmes were separately coordinated by WMO and UNESCO's IOC. The main role of marine forecast and warning programme was to enhance safety at sea. That brought them to the requirement of more observations. Moreover, many other applications required observational data sets and prognostic products for studying ocean and atmosphere. These necessities made the unification of these two organization possible in 1999, with the constitution of JCOMM.

JCOMM OPA (Observations Programme Area) is responsible of the management of the observing systems dislocated in the oceans. Its task is the development, coordination and maintenance of moored buoy, drifting buoy, ship-based and space-based observational networks and related telecommunications facilities.

The OPA Programmes comprehend the Data Buoy Cooperation Panel (DBCP), the Ship Observations Team (SOT) and the Global Sea Level Observing System (GLOSS).

A schematic of the Ocean Observing System components is displayed in Fig. 1.7. It consists of both fixed and mobile measuring platforms, satellite and in situ observations from ships and land radars. Such complex observing system has just

started to be set up in the ocean and will take the next two decades to be completed and be shared among all communities.

1.1.1 Data Buoy Cooperation Panel

The DBCP task is the coordination of the autonomous data buoys to observe atmosphere and ocean conditions in order to increase the quantity and the quality of data collections where few measurements are taken. The DBCP maintains and coordinates over 1250 drifting buoys and 400 moored buoys. They provide sea-surface temperature, surface current velocity, air temperature and wind speed and direction.

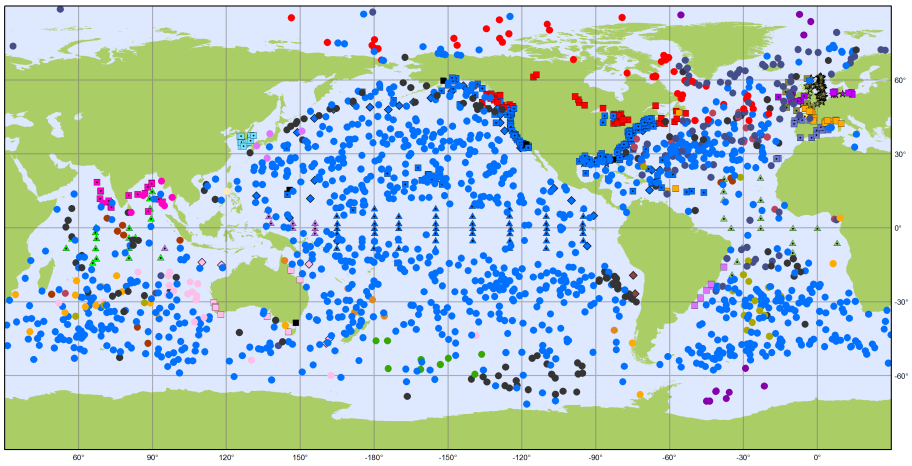

Figure 1.2: Locations of buoys in July 2016. The circles indicate the position of the Drifting Buoys. The square indicate the presence of the Moored Buoys. The triangles stand for the Tropical Moored Buoys. The rhombus are the Tsunameters and the stars indicate position of the Fixed Platforms. Different colors indicate the country that operates on the buoys. Note that the blue markers indicate the USA buoys.

Different kinds of buoys are available worldwide:

The *surface drifting buoys* are attached to a drogue or a sea-anchor, they are easy to deploy and relatively cheap to operate. They make measurements for an average of 18 months of the atmosphere and ocean surface conditions like:

- sea surface temperature (SST)
- sea level pressure (SLP)
- near-surface ocean currents

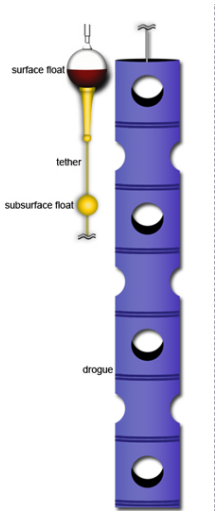

Figure 1.3: An example of surface drifting buoy (http://www.oco.noaa.gov/).

The *Ice buoys* have been used in Arctic and Antarctic regions to track the ice movement. As they have to operate at temperature down to -50°C, they are constructed with low temperature electronics and lithium batteries resistant. They can be equipped with a satellite navigation receiver. They measure:

- air temperature
- seal level pressure
- ice characteristics and movement

The *Moored Buoys* are platforms anchored at fixed locations. They are quite expensive and large. They can reach up to 12 meter long and measure:

- wind, air and sea surface temperature
- salinity
- air pressure
- subsurface temperature

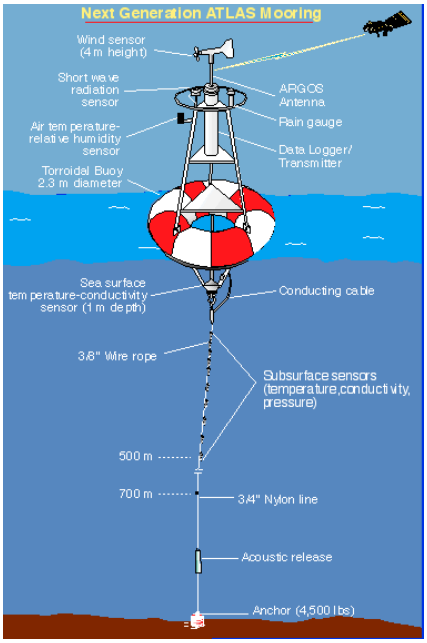

Figure 1.4: A moored buoy (http://www.oco.noaa.gov/).

The *Tropical moored arrays* are arrays or moorings which are used to monitor large scale phenomenon such as El Niño and Southern Oscillation to study the annual variability of global climate. They measure:

- surface meteorology
- subsurface temperature
- subsurface salinity
- subsurface velocity

They are positioned at depth up to 6000 m and the measurement go from the surface to 500 m of depth.

The *Wave Buoys* capture and model information about ocean dynamics on the surface. They measure the spectra, that is the frequency and the size of wave energy to derive the wave height, period and average wave period.

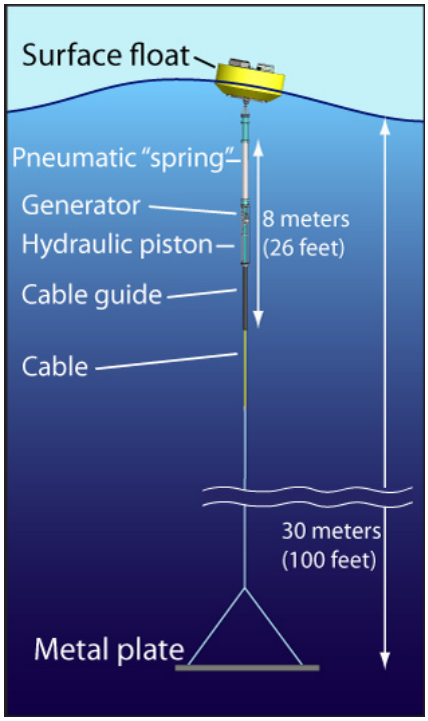

Figure 1.5: A wave buoy (http://www.mbari.org/).

The *OceanSITES reference time series stations* are coordinated by the OceanSITES team and measure:

- air-sea interactions
- deep ocean conditions of many variables over an extended time period.

1.1.2 Ship Observations Team

The Ship Observations Team (SOT) comprehends the VOS (Voluntary Observing Ship Scheme), the ASAP (Automated Shipboard Aerological Programme) and the SOOP (Ship-of-Opportunity Programme). The VOS recorders surface meteorological observations from almost 4000 ships in the world.

1.1.3 Global Sea Level Observing System

The aim of GLOSS is to establish high quality global and regional sea level networks. It counts 290 sea level stations around the world for long term climate change and oceanographic sea level monitoring. The goal of this project is an evenly-distributed sampling of global coastal sea level variations.

1.1.4 Argo Profiling Float Program

Argo is an international programme that uses floats to collect temperature, salinity and current data in the ice-free oceans. The first Argo floats were deployed in 2000

and since then more than 3000 floats have been constructed. It is an instrument 110 cm long equipped with a pressure sensor, a temperature sensor, batteries and a satellite antenna in addition to a number of other sensors.

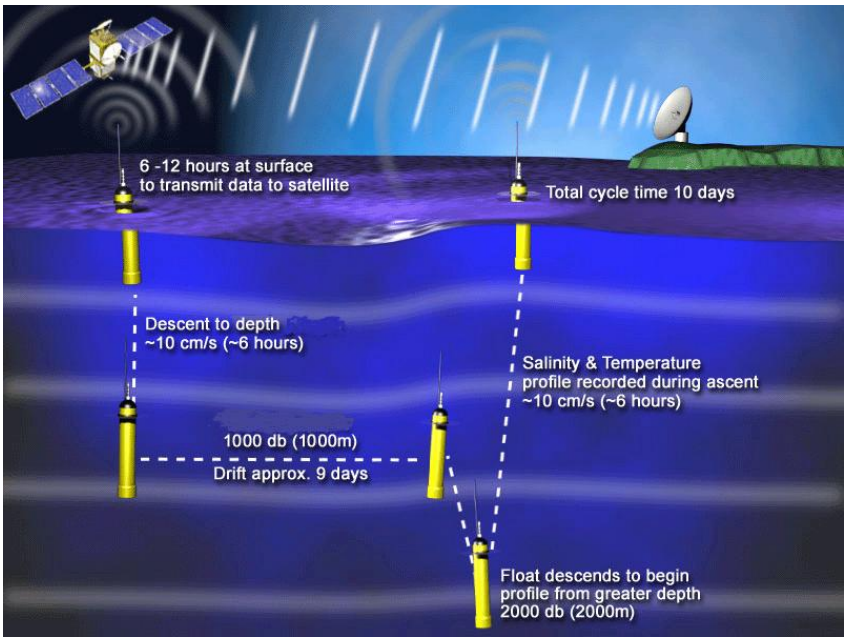

Figure 1.6: The Argo cycle lasts about ten days (http://www-argo.ucsd.edu/).

Its cycle time is about 10 days. As the Argo is thrown by the boat, it immediately sends its position to the satellite. For the next 10 hours the instrument remains at the surface measuring temperature and salinity. It follows a descent at about 1000 m and a drifting of 8-10 days. A new descent up to 2000 m follows. Finally, the Argo ascents measuring temperature and salinity for about 10 hours. At the surface it sends its position and the data to the satellite permitting to have available data within 24 hours. The floats have a design life of about 4 years and costs about $25 thousand per float-life time. Floats are designed to make about 150 such cycles.

1.2 The sub-system of sea floor observations

1.2.1 History

For a long time, oceanographers have desired to measure bottom pressure and observe oceanic pressure field as well as the meteorologists still did with the barometers. The problems in measuring bottom pressure increase when low frequencies measurements are required. In fact, the subtidal dynamic pressure fluctuations are in the range of 0.01-0.1 dbar at pressure of 4000 m and needs instruments with this sensitivity. Moreover, it is not possible to measure the absolute bottom pressure field as the elevation of the sensors on the geoid cannot be defined with sufficient accuracy. For this reason the research on deep water still regards the oscillations of

deep pressure in time and not the absolute values. However, the main difficulty for this kind of studies is the presence of instrumental noise at low frequencies, such as the drift. In other words, the two big problems that scientist have encountered for long time in measuring bottom pressure field have been the low sensitivity of the instruments and the strong instrumental noise at low frequencies. This drift contaminates the observed spectrum at low frequencies. The exact cause of this drift is unknown but it is believed to depend from the temperature, pressure and from the construction of the instrument, as its materials are subjected to high stress. That is why for many years the studies have been concentrated only on high frequencies or tides.

In 1980 J.H.Filloux published his article about bottom pressure fluctuations over a broad frequency range (Filloux,1980). The situation in that period is described at the beginning of the article:'The behaviour of ocean tides away from coast lines and islands is still poorly understood that a program solely dedicated to their observation is justificable' and then 'Although not exactly easy to perform, pressure measurements on the sea floor constitute at present the most effective approach to estimate tidal fluctuations of sea level over the open ocean'. The instrument used for the measures was a Bourdon tube-type transducer. It was localized at the coordinates 18°56'N, 152°29'W, 330 km east of Hilo, Hawaii and recorded ocean bottom pressure for two months. The first problem to solve was the subtraction of the drift component associated with plastic flow of the transducer. The tidal fluctuations appear only as tiny ripples because of the large plastic flow in the transducer due to abyssal pressure. In 57 days of data acquisition the creep had a curve difference of 40 m. Filloux considered that the creep pattern was understood and predictable and so possible to correct. Moreover, in his opinion the transducer could be optimized because several adjustable variables were involved (geometry, cold work level, age hardening, thermal shock stabilization). The most common functions used to approximate the trend were the logarithmic function, the exponential function and the power law. The function that best represented the plastic flow in Filloux research was the power law T^D but D value had to be corrected. He assumed a function of the form

$$A + B \times (T + C)^D \tag{1.1}$$

where A,B,C,D were constants, T the time referred to initiation of data recording with A adjusting the datum, B scaling the time dependence and C representing the time elapsed between pressurization and start of data logging (this was a free parameter because pressurization is not instantaneous but occurs about the 2 hours that it needs to reach the bottom). When this constant had been evaluated, a small transient was still in the series. It was characteristic of the first few days. So, the shape comes from the contribution of two exponential decays with different signs and different time constants. The plastic flow had finally been represented as

$$A + B \times (T + C)^D + \sum_{1}^{2} E_i exp[-(T + C)/F_i] \tag{1.2}$$

where E_i are the amplitudes and F_i the time constants of the exponential transients.

The next step had been the subtraction of the tidal frequencies. The calculation of tidal frequencies came from the estimation of the terms of a Taylor expansion, explained in another article (Filloux, 1971). The most important tidal frequencies found were the diurnal, the semidiurnal and the terdiurnal frequencies. The subtraction of the tidal series from the detrended series had been called residual pressure fluctuations.

At the end of the 80's new performances on bottom pressure measurements for low frequencies have been achieved (Watts and Kontoyiannis, 1989). Watts and Kontoyiannis collected bottom pressure observations in a period from September 1983 to March 1987 in the Gulf Stream at depths between 3300 and 4400 m. The duration of the deployment varied from 3 to 12 months. In that period seven different pressure sensors were used for a total of 17 deployments at 12 sites. The instruments used were Bellows and Bourdon-tube (type of Quartz Crystal resonator transducers). The bellows presented working range between 0-3450 db and the Bourdon-tube between 0-4100 db. The innovative characteristic of this research has been the analysis of the drift in order to remove it. The long-term drift was evident after removing the mean and the tides. A rapid slewing toward higher pressure during the first 12 hours had been observed, due to the time required to the sensor for the thermal equilibrium. The drift during the following 3-12 months was between 0.2-0.85 dbar with a decreasing rate with increasing time. As said before, to investigate the kind of drift, previous studies proposed to use power-law ($(t - t_0)^\beta, 0 < \beta < 1$), logarithmic ($ln(t - t_0)$) or exponential ($exp[-\alpha(t - t_0)]$) functions. The detrending method proposed by Watts and Kontoyiannis was a least-square fit of these three mathematical models to the records. A comparison of the results showed that the exponential law was the best approximation. The mathematical representation of the drift the two authors found for their observations was

$$P_{drift} = P_1[1 - exp(P_2 t)] + P_3 + P_4 t \tag{1.3}$$

where P_i are free parameters determined by the nonlinear regression subroutine and t is the time.

In his article Hughes (Hughes et al.,2012) demonstrates that a single Ocean Bottom Pressure (OBP) time series, can measure ocean mass changes. The OBP measurements have been done in two site of the Pacific Ocean. The first measurements were collected in 2001-2002 with a mooring positioned northern of the equator (125°W, 8.5°N). The second group of measurements have been collected since 2002 and mooring are located symmetrically to the first (125°W, 8.5°S). The basic idea is that, if sea level changes were spatially uniform, then variation of the volume of the ocean could be monitored using a single tide gauge. On the other hand, if spatial

variations are present it is necessary to do sea level measurements on the entire ocean by a satellite altimetry. In the same way, spatially uniform changes in ocean bottom pressure would mean that ocean mass changes could be monitored with a single OBP Recorder. In the area under study, Hughes demonstrated, comparing observed data, model data and satellite data, the possibility to measure ocean mass changes with a single station. This is an important result because it justifies the need of one single bottom pressure sensor to explain the whole area under study when it is characterized by uniform spatially sea level changes.

1.2.2 Bottom pressure sensors

The most common pressure sensors include:

- Vibrating wire
- Capacitance plate transducer
- Strain gauge pressure sensor
- Quartz-crystal resonator transducer (Bourdon-tube and Bellows)

1.2.2.1 Vibrating wire

It is also called Vibrotron sensor. It utilizes pressure-induced strain to vary the frequency of vibration of the wire. Patented in the 1940's by Rieber, is one of the earliest designs. It is composed of a tungsten wire attached to a diaphragm throughed by an alternating current in presence of a magnetic field. Variations in external pressure vary the tautness and so the resonant frequency of the wire.

1.2.2.2 Capacitance plate transducer

It is composed of two parallel capacitance plates and the distance between the two varies as a function of pressure applied to an attached diaphragm. Capacitance is inversely proportional to the plate gap. This instrument has better accuracy and flexibility with respect to the Vibrotron but the mechanical transducers are unstable.

1.2.2.3 Strain gauge pressure sensor

It has been designed in 1970's. The pressure acting on a flexible element causes a mechanical deformation and a variation of the resistance of a conductor. To increase sensitivity and minimize temperature effects its often incorporated a Wheatstone bridge. It has long been used to measure tides. They are not adapted for long-term deep deployments, so they cannot be used when large dynamic range, high sensitivity and low drift are required.

1.2.2.4 Quartz-crystal resonator transducer

It measures the pressure induced from the changes in the vibrational frequency of a quartz beam. Originally (1970's) a piezo-electric resonator was utilized (Hewlett-Packard sensor). The advantages were an increased pressure sensitivity and a decrease of temperature sensitivity. Studies in this field demonstrated that the most important limitations of these instruments were poor pressure sensitivity, significant temperature dependency, restricted frequency response, high power requirements and long-term transducer instability. Newer transducers present long-term stability and greater accuracy.

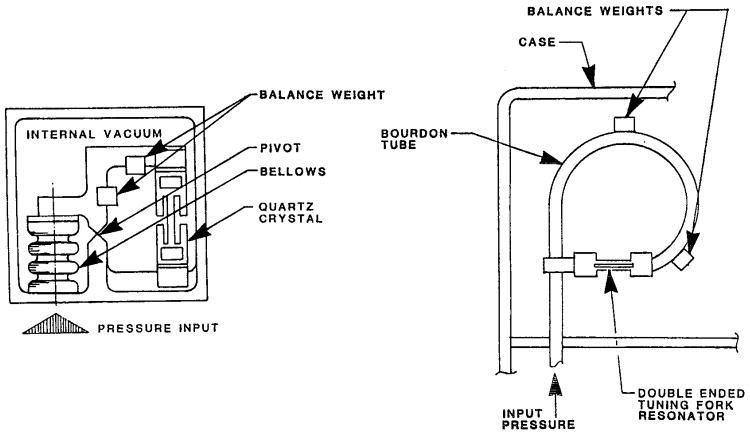

Figure 1.7: Digiquartz pressure transducers, a bellows sensor and a Bourdon-tube sensor (Watts and Kontoiannis, 1989).

1.2.3 What is the bottom pressure

Bottom pressure is the pressure values observed at the sea floor. The pressure at any depth z below the sea surface can be calculated from the hydrostatic equation:

$$\frac{\partial p}{\partial z} = -\rho g \tag{1.4}$$

to obtain

$$p(z) = p_a + \int_{-H}^{0} \rho g dz + \int_{0}^{\eta} \rho_0 g dz = p_a + \int_{-H}^{0} \rho g dz + \rho_0 g \eta \tag{1.5}$$

where ρ is the ocean density, that can be computed using the temperature and the salinity, ρ_0 is the density at the sea surface assumed to be equal to 1025 $kg\,m^{-3}$, H is the water depth, η is the sea surface elevation due to tidal components and barotropic signals, g is the gravity acceleration considered to be constant and equal to 9.81 $m\,s^{-2}$, p_a is the atmospheric pressure.

Converting the pressure at the depth $z = -H$ to water column height one obtains:

$$\underbrace{\frac{p(-H)}{\rho_0 g}}_{h_{eq}} = \underbrace{\frac{p_a}{\rho_0 g}}_{(1)} + \underbrace{\eta}_{(2)} + \underbrace{\frac{1}{\rho_0}\int_{-H}^{0}\rho(z)dz'}_{(3)} \tag{1.6}$$

where term (1) is the atmospheric pressure water column equivalent thickness, term (2) is the sea surface displacement due to tidal and other barotropics signals and term (3) is called the Columnar Density Content (CDC) and is the water column thickness due to the mean density of the ocean and its locally anomalies.

1.3 Previous studies of bottom pressure data in the Mediterranean

Researches of bottom pressure have been carried out (Marcos, 2014) studying the correlation between bottom pressure and sea surface level. Generally, the ocean answer to short time scale (less than 100 days) and long time scale (intra-to inter-annual) is different. In the first case the sea level is related to bottom pressure. In the second case sea level is more related to steric processes than to bottom pressure. Exceptions have been found in some cases, for shallow and shelf areas and semi-enclosed basins. An example is the Mediterranean Sea, where the bottom pressure and the sea level changes show a correspondence even at long time scales. Marcos studied the variability of bottom pressure in the Mediterranean Sea at different time scales and its relationship with sea level at regional and local scales. The dataset used for this study is a reanalysis for the period 1999-2011 from the Copernicus Marine Environment Service (http://marine.copernicus.eu/). The fields of temperature, salinity and sea surface height are daily outputs at the spatial resolution of 1/16° x 1/16° in latitude and longitude and 72 unevenly spaced vertical levels.

The scale of variability of the bottom pressure has been studied. A standard deviation showed a bottom pressure variability between 4 and 8 cm and a sea level variability up to 12 cm.

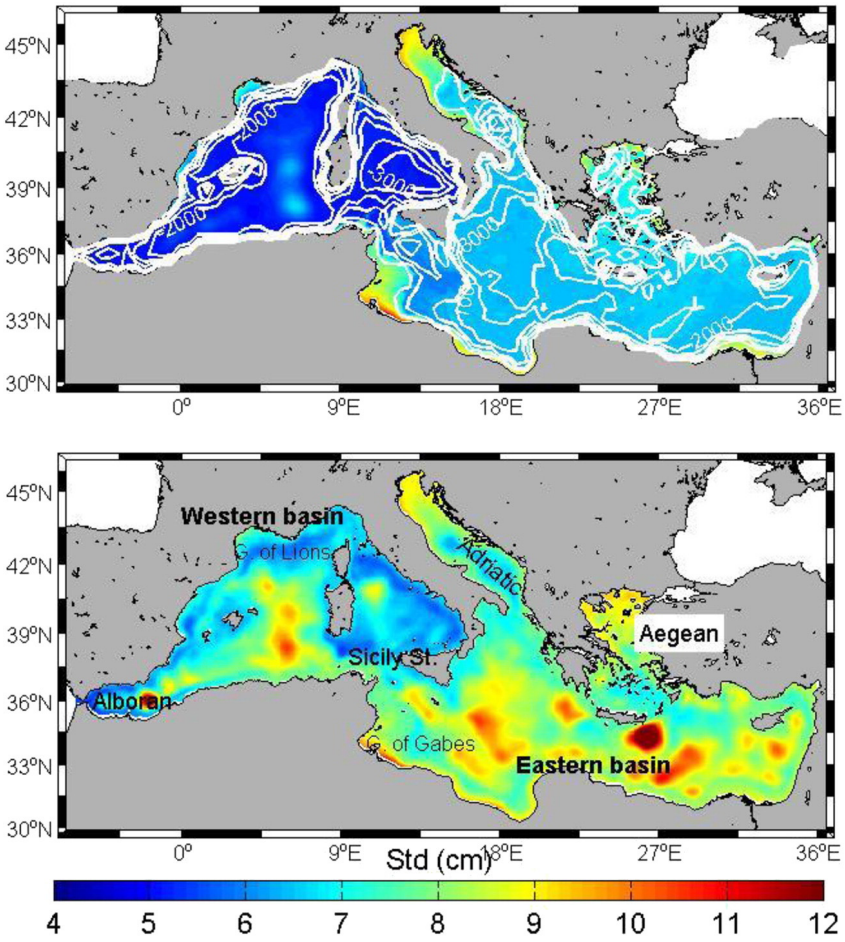

Figure 1.8: Standard deviation of bottom pressure (top) and sea level (bottom) in the Mediterranean Sea from 1999 to 2011.

Large variability in sea level has been found in areas with intense mesoscale activity, for example the western African coast following the Algerian Current and south of Crete in the Eastern Mediterranean. It is important to remember that the spatial distribution is due to regional steric processes. The bottom pressure variability is indeed confined to coastal and shallow water areas. The variability of bottom pressure is higher in the Eastern basin (6.7 cm) while it is smaller in the Western basin (5.3 cm). The sea level standard deviations do not show such a net cut as bottom pressure. The two curves of sea level and bottom pressure variations in that case show a correlation of 0.75.

The second part of the results treats rapid fluctuations of bottom pressure for a period of 60 days. These show an important correlation between bottom pressure and sea surface confirming the barotropic behaviour of high frequencies sea level oscillations, in the Mediterranean Sea as in the oceans.

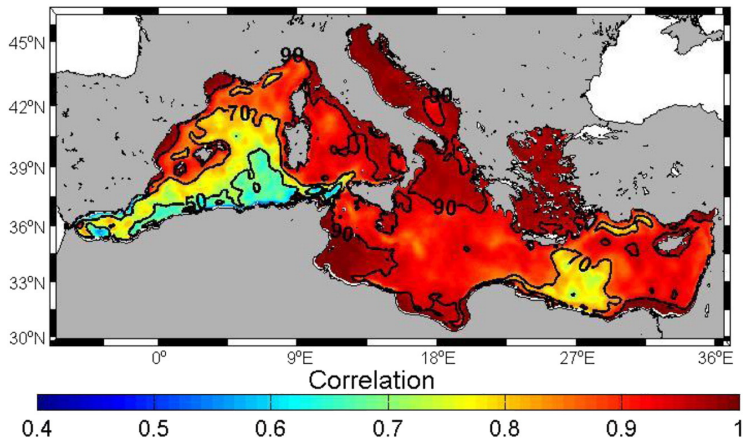

Figure 1.9: Correlation of rapid fluctuations between bottom pressure and sea level.

Another comparison has been carried on considering sea level at two coastal sites (one in the Western basin and one in the Eastern basin) and the bottom pressure of the entire basin. The result is a no-correlation between the rapid bottom pressure and the two basins with the cut line on the Strait of Sicily. However, high correlation has been found within each subbasin. In the same way deep water points, instead of sea level, have been compared to bottom pressure obtaining the same results. The decoupling between the two subbasins is due to topographic effects. The two subbasins have different energy distributions: the Eastern basin peaks at 41 days while the Western basin peaks at 48 and 31 days with lower energy. The origin of these rapid bottom pressure fluctuations has been studied forcing with zonal wind stress the Atlantic side of the Strait of Gibraltar. The results demonstrate that energy due to zonal wind causes rapid barotropic oscillations in the entire basin. The wind stress at Gibraltar transmits energy to the basin in the form of bottom pressure oscillations. This will excite the natural modes of the two subbasins. The two subbasins in the Mediterranean Sea can be seen as a system of coupled oscillators separated by the Strait of Sicily. This means that each subbasin is affected by its own topography and by the presence of the other subbasin.

The seasonal cycle and the low frequency variability of bottom pressure show the specificity of the Mediterranean Sea as it is expected to find high correlation between sea level and bottom pressure as well as for the short time scales. The semi-annual cycle in sea level and bottom pressure are very similar, that confirm that semi-annual sea level variations in the Mediterranean Sea are barotropic.

The mean annual signal of bottom pressure is smaller in Western basin (2.3 cm on average) than in the Eastern basin (4.2 cm on average) but the values are quite constant within each subbasin. The smaller annual cycle in the western basin is partly responsible of the lower values of standard deviations of non-filtered bottom pressure described in Fig. 1.8. The bottom pressure mean annual cycle peaks at the end of November, that means that the annual cycle sea level reaches its maximum at the beginning of October. To note that the annual sea level cycle has the steric effect

as predominant and its the result of two sinusoidal signals, one peaking in September due to the thermal expansion or contraction caused by the heat fluxed at the sea surface and the other peaking in December due to the water mass variations within the basins. The average amplitude of bottom pressure annual cycle is 3.6 cm while in the Northeast Atlantic is 0.5-1 cm. This difference is due to a different origin of the seasonality in the basin: in the Mediterranean Sea the mass-induced annual signal is driven by changes in evaporation, precipitation and river run-off, where the evaporation is the most important.

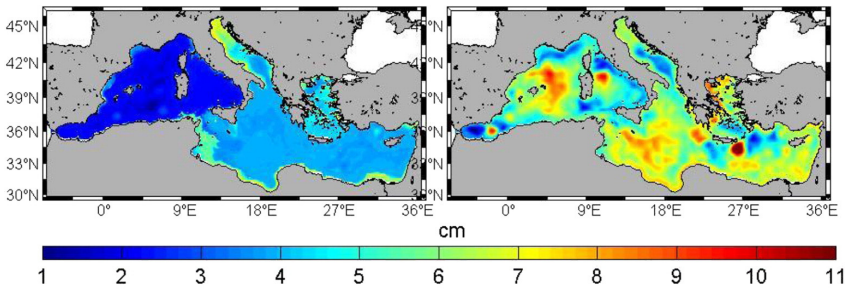

Figure 1.10: Correlation between sea level and bottom pressure for the mean annual cycle.

Low frequency variability using low-pass filter (more than 60 days) shows a decrease of the correlation with respect to high frequencies. However, the correlation is larger than with other regions in the world with similar depth and there is still correlation in shallow waters, indicating again a barotropic nature of the sea level oscillations. A lower correlation is present in deep water where the increase of the period increases the dependence on the depth. The non-seasonal low frequency variability shows a standard deviation between 2 and 7 cm for sea level and about 4 cm for bottom pressure.

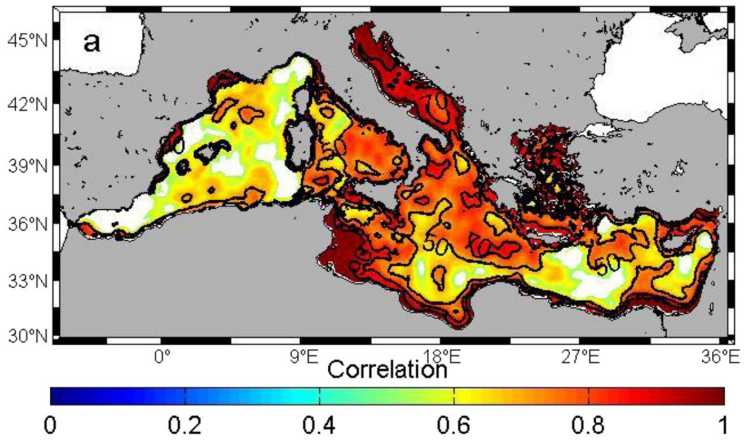

Figure 1.11: Correlation between sea level and bottom pressure for low frequency variability.

As in the case of rapid fluctuations, a comparison between two deep water points and bottom pressure over the whole basin has been done. Correlations of 0.8 and more have been found everywhere showing that bottom pressure signal is coherent within the domain. The coastal region shows lower correlation, indeed, the coastal bottom pressure is influenced by steric changes in the deep ocean that induce bottom pressure changes, for example water mass redistribution in shallow waters.

To summarize, Marcos confirmed the barotropicity of the basin average sea level changes in the Mediterranean Sea at all time scales. This characteristic is usually only for the shallow water. High correlation is more characteristic of shallow water areas on coastal locations. That means that sea level in deep water everywhere in the basin result from the addition of spatially coherent mass-induced component and the local steric variability. The smaller the steric changes the higher the coherence between coastal and open bottom pressure. The Mediterranean Sea is so characterized by correlation between mass-induced sea level changes and bottom pressure over a large area and for long scales. The variability of the mass-induced is mainly related with the exchanges through the Strait of Gibraltar driven by the local sea level changes in Atlantic by the Strait.

1.4 Thesis objectives

The basic aim of this thesis is the investigation of bottom pressure in deep water. Several studies have been carried out to understand the sea level fluctuations and their relationship with other phenomena but the difficulty in collecting data at the bottom of the sea has limited for long time the possibility to study this influence in deep water as well. The improvement of technology and the collaboration with other fields of the physics made this observations possible. An example of this is the ANTARES Observatory, whose bottom pressure data have been used for the analysis discussed in this thesis.

The guidelines of this thesis is the relationship of the sea surface level with external phenomena, the relationship of the sea surface with bottom pressure in deep water and consequently the connection of bottom pressure with the external phenomena.

The first part of the analysis consisted in a treatment of the raw data of bottom pressure, that means to deal with the characteristic of the series due to the instruments. Despiking, averaging and filling have been applied to the raw series of data. The second part required a more physical approach to the series. The detiding and the detrending procedures have been applied. The interpretation of the spectra resulted from the analyzed series followed introducing the oceanographic component in this thesis.

The last part consists of a comparison of the observed data to the model data from the NextData Archive.

Chapter 2

The ANTARES Observatory

ANTARES is a neutrino telescope whose name stands for 'Astronomy with a Neutrino Telescope and Abyss environmental RESearch'. Its main goal is the search for high energy astrophysical neutrinos from Galactic and extra Galactic sources. It has been taking data in its full configuration since 22 May 2008. ANTARES infrastructure is located 40 km offshore from Toulon (Fr) at the coordinates 42°48'N, 6°10E' at a depth of 2478 m.

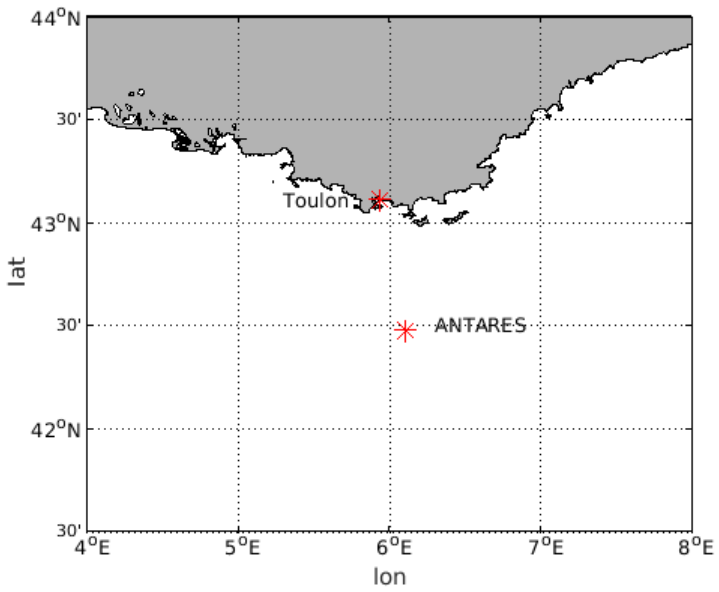

Figure 2.1: Position of ANTARES Observatory.

The detection principle is based on the collection of the Cherenkov photons induced by the charged particles produced in neutrino interactions. The basic unit of the detector is the optical module (OM), consisting of a photomultiplier tube and the associated electronics, contained in a pressure-resistant glass sphere of 17 inch diameter. The OM are mounted on 12 mooring lines whose bases are anchored at the sea bottom about 350 m high. OM are grouped in triplets. Each triplet together with a titanium container for instrumentation and front-end electronics is a "storey". The storeys are distributed along an electro-mechanical cable. Each string carries 25 storeys spaced vertically by 14.5 meters. The strings are distant about 60 meters from each other. Each string is connected to a junction box which

provides power to the detector and guarantees data exchange from/to the offshore detector and an on shore station, located at La Seyne-sur-Mer, thanks to a 40 km long electro-optical cable. In addition to the optical sensors, a number of other instruments for string positioning and for marine and Earth sciences are mounted at the bases, along and in proximity of the strings and connected to the junction box.

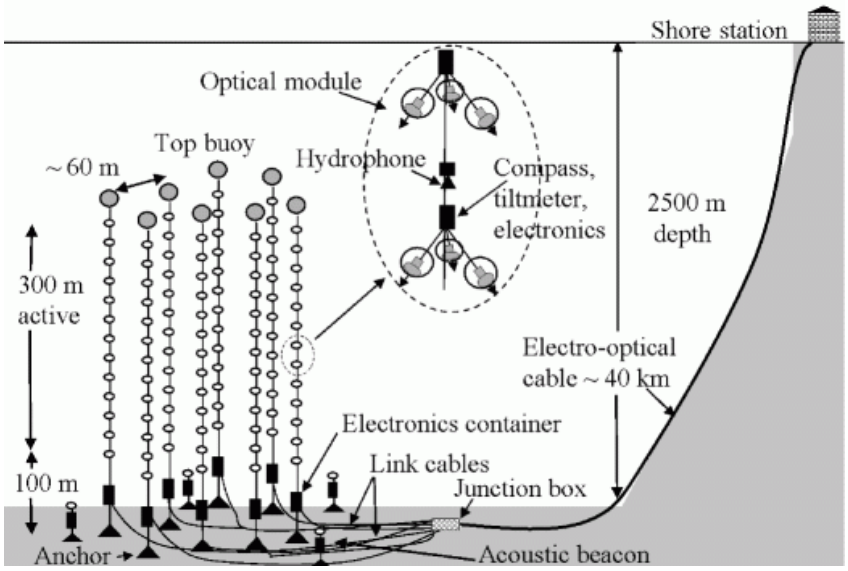

Figure 2.2: Antares scheme.

2.1 ANTARES and sea sciences

Due to its location on a plateau in the deep sea, this infrastructure provides opportunities for innovative measurements in sea sciences. The studies of the phenomena in deep water have always been a problem for the difficulty in the data collection. Many instruments on the depth are not connected with the coast and needs batteries and memories to collect data; the data can be analyzed only when the instruments are removed from the sea. ANTARES infrastructure, instead, guarantee a permanent connection to shore with the capacity for high-bandwidth acquisition of data. It is possible to install sensors for sea parameters measurement giving long-term measurements. This instruments, such as the pressure sensors, are installed on all of the 12 lines of the detector.

The lines are anchored on the seabed with the Bottom String Socket (BSS) and is held vertical by a buoy at the top. The lines are arranged on the floor in an octagonal configuration. It is completed by the Instrumentation Line (IL07) which supports the instruments used to perform environmental measurements.

Objects	Latitude	Longitude	Immersion(m)
Point central ANTARES	42°47.935'N	6°09.942'E	2478
Box junction (JB)	42°47.849'N	6°09.877E	2476
BSS line 1 (L1)	42°47.989'N	6°09.940E	2478
BSS line 2 (L2)	42°47.969'N	6°09.994E	2478
BSS line 3 (L3)	42°47.956'N	6°09.932E	2478
BSS line 4 (L4)	42°47.942'N	6°09.973E	2478
BSS line 5 (L5)	42°47.977'N	6°09.895E	2478
BSS line 6 (L6)	42°47.931'N	6°10.009E	2478
BSS line 7 (L7)	42°47.927'N	6°09.914E	2478
BSS line 8 (L8)	42°47.916'N	6°09.949E	2478
BSS line 9 (L9)	42°47.939'N	6°09.868E	2478
BSS line 10 (L10)	42°47.895'N	6°09.986E	2478
BSS line 11 (L11)	42°47.904'N	6°09.884E	2478
BSS line 12 (L12)	42°47.882'N	6°09.933E	2478

Table 2.1: Lines position.

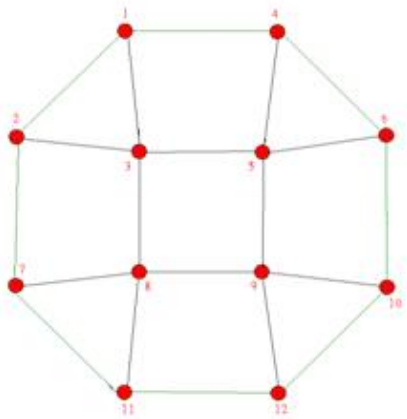

Figure 2.3: Arrangement of the lines and the ocean pressure sensors.

2.1.1 Pressure sensor

The pressure sensors are installed on each BSS line at approximately a depth of 2478 m. The sensors are instruments constructed ad hoc by GENISEA and have the following properties:

- Titanium container
- 48 VDC external power, RS232 serial link
- Pressure sensor DRUCK piezo-electric range 0-300 bars
- Precise calibration at IFREMER-Brest between 190 and 260 bars

- Precision obtained <0.01 bars

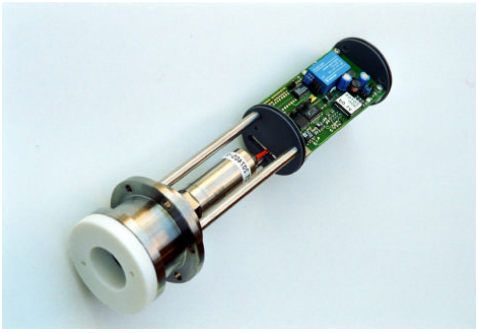

Figure 2.4: The bottom pressure sensor assembled on the anchor.

2.1.2 Other deep-sea infrastructures in the Mediterranean Sea

The Mediterranean Sea offers optimal conditions for the location of the neutrino telescope: clear sea water, long periods of good weather conditions for sea operations, proximity to large industrial, commercial and scientific infrastructures.

The activities for the construction of ANTARES started in 1996 and the observatory became operative on the 22 May 2008. Other deep-sea infrastructure similar to ANTARES are present in the Mediterranean Sea. For all that observatories the main aim of that projects is the investigation in the field of neutrino astronomy and in the field of Earth and Sea science.

NESTOR (Neutrino Extended Submarine Telescope with Oceanographic Research) in located offshore Pylos (Greece) where seabed depth is between 3800 m and 5000 m. It is composed of a semi-rigid structure, called NESTOR tower, 360 m high and with a diameter of 32 m. The basic element of the NESTOR is an hexagonal floor with two optical modules at the apex of each arm, one upward-looking and the other downward-looking.

NEMO (NEutrino Mediterranean Observatory) is a project carried out since 1999 that lead to the construction of that neutrino telescope 80 km off the Sicilian coast at a depth of 3500m. The NEMO Phase-1 became operative in December 2006 with the deployment and connection of a submarine junction box and the construction of 4-floor prototype tower structure hosting 16 Optical Modules. The NEMO Phase-2 is an infrastructure that has recently been completed and is located in the harbor of Portopalo di Capo Passero an connected via optical fiber to the Internet, permitting data distribution in real time to collaborating institutes and counts 32 optical modules.

KM3Net is an on working observatory that will consist in 300 vertical structures called Detection Units (DUs), anchored on the sea floor and kept vertical by subtended buoys. The DUs are connected to shore via a sea-bottom network of electro-optical cables. The project thinks to separate the telescope into a network of more and smaller building blocks. Among other things it would be advantageous

for the distribution of power and data that would become simpler and the impact of possible failures would be reduces to the blocks. The candidate deep-sea sites for the KM3NeT detector are Toulon, Capo Passero and Pylos.

2.2 Tidal motion and Toulon tide gauge station

2.2.1 The equilibrium tide and the main components

The equilibrium tide is the theoretical tide produced by an ideal ocean of uniform depth covers Earth and where there is no friction between the water in the ocean and the ocean floor. The configuration that deals with changes in ocean depth, the existence of continents and the friction between the ocean water and ocean floor is the dynamical theory.

Under such theory the water surface would be a rotational ellipsoid, with the major axis directed toward the moon. About the propagation of the equilibrium tide wave, the rotational ellipsoid describing the surface elevation in the equilibrium case is characterized by two peaks (bulges) and two troughs distributed over the Earth sphere. The wavelength of the equilibrium tidal wave will be approximately half of the earth circumference. In the real ocean tidal wavelengths are in the order of $10^3 km$ and the ocean average depth is about $4km$. Therefore tidal waves travel as shallow water waves with a velocity of $c = (gH)^{1/2}$ where H is the bottom depth.

The Tide Generating Force (TGF) is the force originated by the composition of the centrifugal and the gravitational force. It is possible to obtain TGF due to the sun considering M_s the mass of the Sun and D the Earth-Sun distance. The maximum range in the moon and sun equilibrium tides is scaled by the same factor. The larger mass of the sun is compensated by its larger distance, and the sun TGF is less then half the moon's.

Tidal component	Period (solar hour)	Description	Nature
M2	12.42	Principal lunar	semi-diurnal
S2	12.00	Principal solar	semi-diurnal
N2	12.66	Larger lunar elliptic	semi-diurnal
K2	11.97	Luni-solar	semi-diurnal
K1	23.93	Luni-solar diurnal	diurnal
O1	25.82	Principal lunar diurnal	diurnal
P1	24.07	Principal solar diurnal	diurnal
Q1	26.87	Larger lunar elliptic	diurnal
MF	327.90	Lunar fortnightly	long term
MM	661.30	Lunar monthly	long term
SSA	4383.00	Solar semi annual	long term
M4	6.21		compound
MS4	6.10		compound

Table 2.2: Main tidal components (http://www.phy.ornl.gov/).

The main effects on the tides are therefore due to the revolution of the Moon around the Earth and the revolution of the Earth around the Sun. To solve the TGF for that configurations is so necessary to resolve that waves by a large number of harmonic constituents. The main constituents are explained in Tab. 2.2.

Important for this study are the diurnal and semi-diurnal components. The M2 component that is the component due to the position of the Moon around the Earth will lead to two high and two low tides per day. The particularity is that the two high tides will occur every 12 hour and 25 minutes and the timing of high and low tides will be delayed by approximately 50 minutes from one day to the next. This is because the lunar day is 24 hours 50 minutes long and so the Moon crosses the same meridian at that range time, 50 minutes later the solar day that is 24 hours.

The moon declination is also to consider. Declination is 0° when the moon is overhead the equator and 28.5° approximately one week later (27.3/4 days). That will define the lunar month and consequently, spring tide and neap tide due to the different moons. For the spring tide (the new moon and the full moon), the tidal range is higher then average, with high tide higher and low tide lower. On the other hand, for neap tide (the first quarter and third quarter moon) the high tide is lower and the low tide is higher.

The same considerations can be applied to the Earth-Sun system.

2.2.2 Diurnal, semidiurnal and mixed semidiurnal tides

The first cause of the elevation of the sea surface is due to the astronomical interaction between Earth and planets, such as the Moon and the Sun. This interactions basically bring to one or two peaks during the day due to the rotation of the Earth on its axis. The fact that Earth in not a perfect sphere and the presence of large continents block the westward passage of the tidal bulges as the Earth rotates bringing to different elevations of the two high tides and the two low tides during the day. Moreover the locally characteristic of the tides will be affected by the kind of basin. There are three basic tidal patterns: the diurnal tide, the semidiurnal tide and the mixed semidiurnal. The most common pattern is the semidiurnal tide, presenting two high tides and two low tides each day, where the two high and the two low peaks have about the same height. If the peaks of the high tides and the peaks of the low tides differ in height they are called mixed semidiurnal tides. The areas where only one peak of high tide is present in one day present diurnal tides.

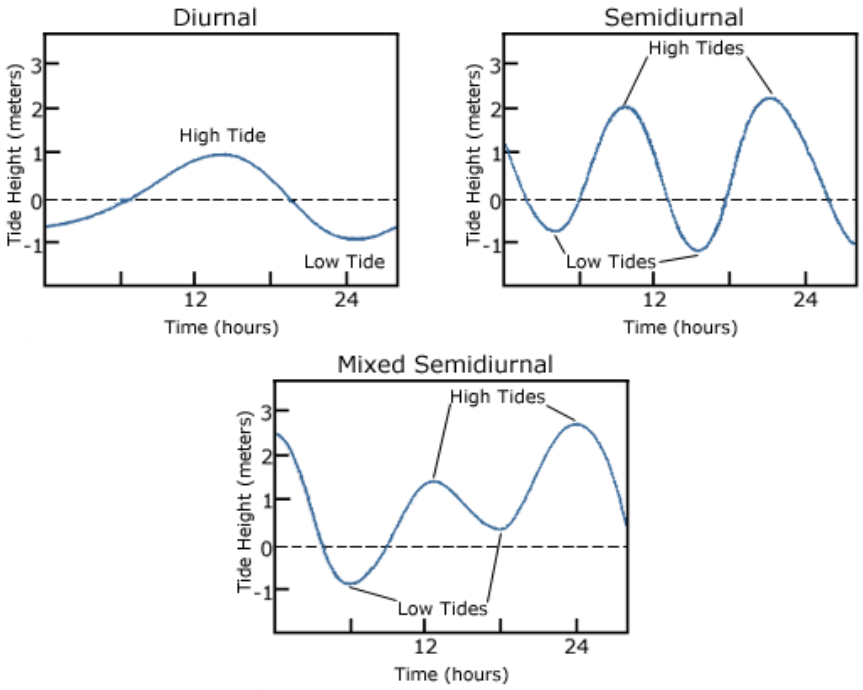

Figure 2.5: An example of diurnal tide, semidiurnal tide and mixed semidiurnal tide (http://oceanservice.noaa.gov/).

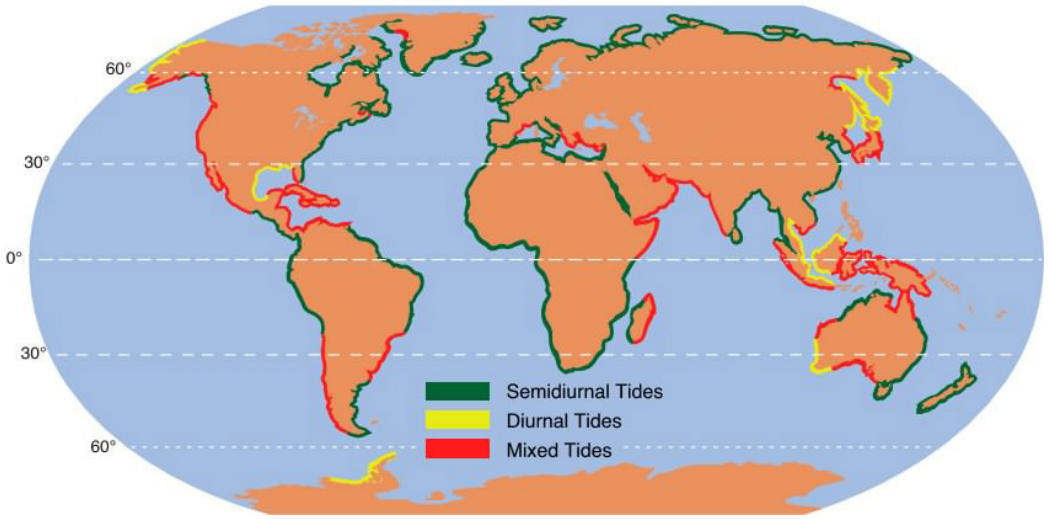

Figure 2.6: Distribution of diurnal, semidiurnal and mixed semidiurnal tides in the world. Notice the semidiurnal tide characterizing the Gulf of Lion.

2.2.3 How to measure the tides

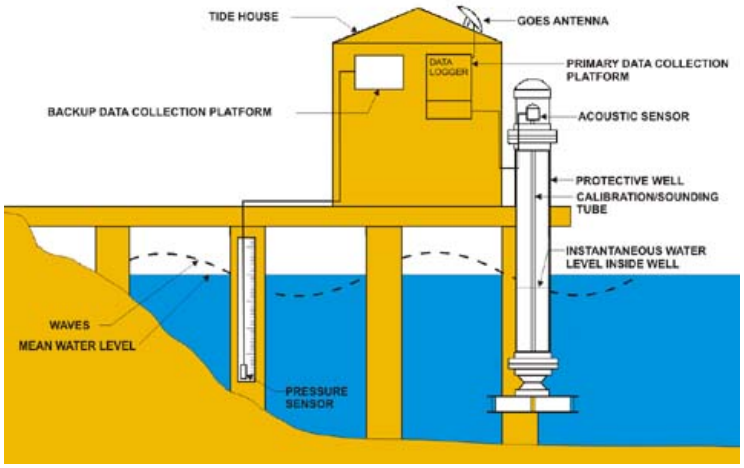

Figure 2.7: An example of tide gauge used by NOAA.

Tide gauge are the instruments finalized to the measurement of the sea level. They consist in a tide house and its instrumentation. The main instrument is a recorder that sends an audio signal down a 1 cm wide sounding tube and measures the time it takes for the reflected signal to travel back from the waters surface. The sounding tube is mounted inside a 15 cm diameter protective well. To support the tide measures other oceanographic and meteorological measures are collected, as wind speed and direction, water current speed and direction, air and water temperature, barometric pressure. The data are collected every six minutes and timing is controlled by a Geostationary Operational Environmental Saltellite (GOES). The station also uses these satellites to transmit their data hourly.

The older tide gauge didn't use acoustic and electronics recorders but mechanical floats. The sea level variation was measured by a recorder driven by a float in a stilling well and water level data were recorded on a continuously running pen and ink strip chart. The records were collected by observers once a month and processed manually. Water levels were recorded at 6 minutes intervals and the clocks were maintained and adjusted by the observers.

2.3 Tides in Toulon

An analysis of the tides in Toulon has been done in order to compare the bottom pressure equivalent tidal signal with the tidal signal measured in Toulon. The position of the tide gauge is 43.12289810 N, 5.91472006 E. In 2008 the tide gauge in Toulon has been modernized with the installation of a radar level sensor, replacing the previous acoustic sensor installed in 1998. The vicinity to the ANTARES site make this tide gauge measures comparable to deep pressure observations. Toulon tide gauge is important because it gives informations about the tides. In Eq. 1.6, in fact, one term indicates the presence of the tides in the bottom pressure. An intercomparison with the observed bottom pressure series will be done successively in 3.7.2. This section want only to describe the characteristics of the tides in that area. The observation series of elevation by Toulon tide gauge has a frequency of 60 minutes. The available data for this study are from 1 January 2008 to 16 October 2013. The tide gauge in Toulon presented some problems in 2011 with some long gaps in the series. For this reason the analysis of the kind of tides in this area is concentrated for 2009 and 2010.

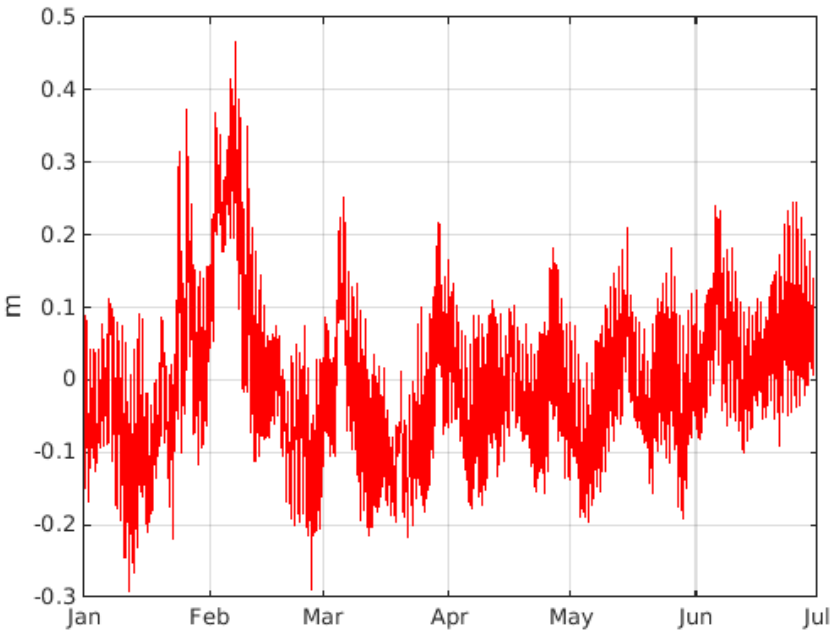

Figure 2.8: Observations of sea surface elevation by tide gauge in Toulon from 01 January to 30 June 2009.

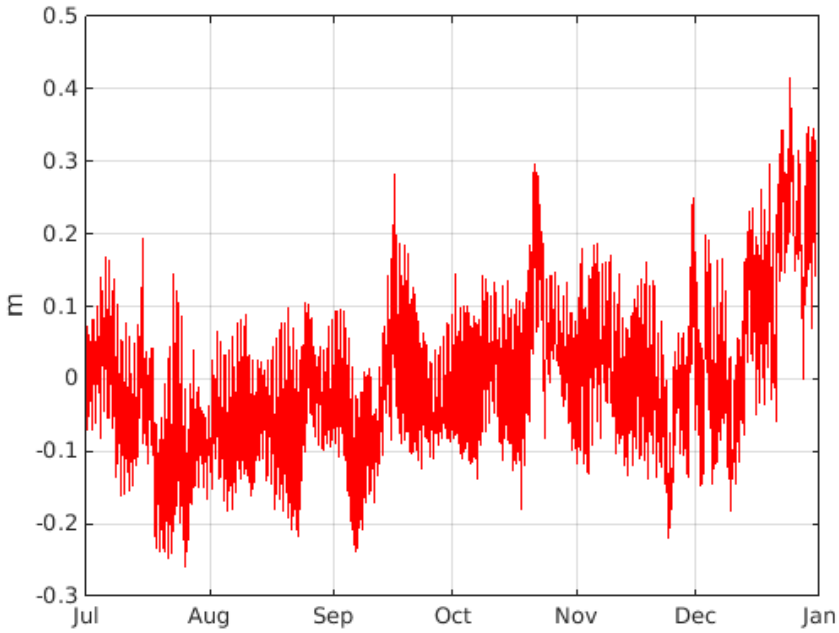

Figure 2.9: Observations of sea surface elevation by tide gauge in Toulon from 01 July to 31 December 2009.

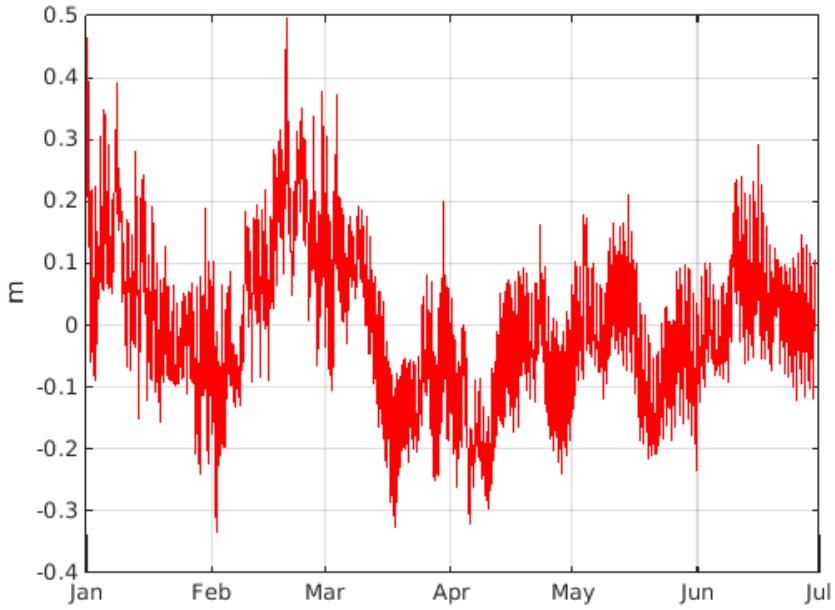

Figure 2.10: Observations of sea surface elevation by tide gauge in Toulon from 01 January to 30 June 2010.

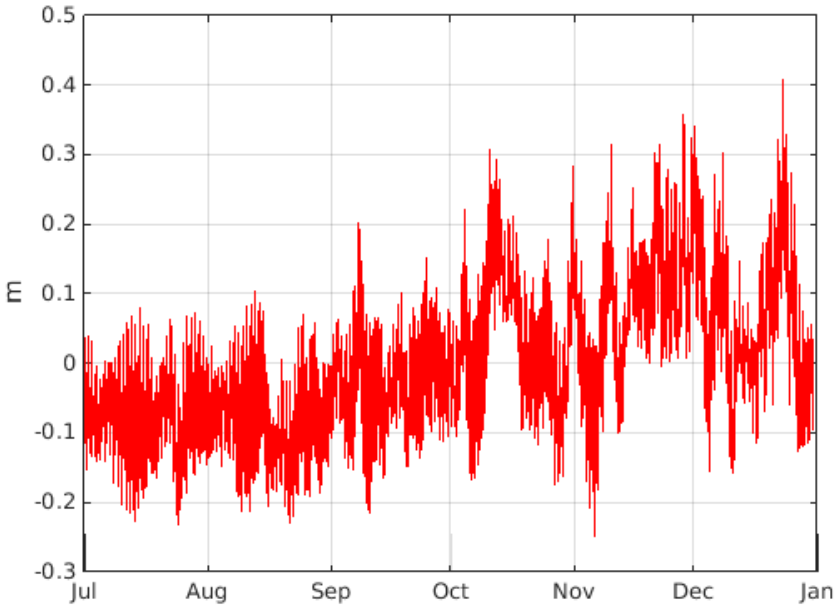

Figure 2.11: Observations of sea surface elevation by tide gauge in Toulon from 01 July to 31 December 2010.

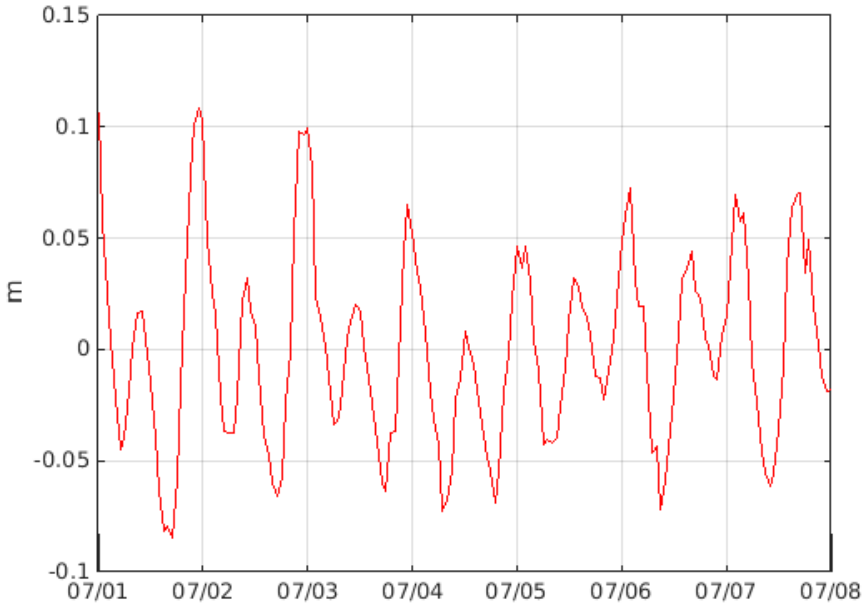

Figure 2.12: Sea surface elevation in Toulon from 1 to 7 July 2010.

Fig. 2.12 shows sea surface elevation from 1 to 7 July 2010. A mixed semidiurnal

tide, which is characteristic of Gulf of Lion, is evident. Two high tides and two low tides and different elevation respectively are evident. The sea level wave measured by the tide gauge in Toulon is composed of many frequencies.

A spectra of the sea surface elevation in Toulon in 2009-2010 has been done.

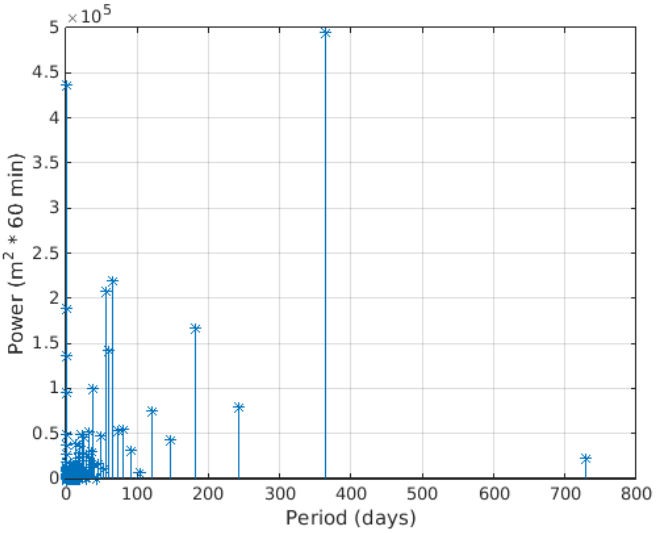

Figure 2.13: Spectra over the years 2009 and 2010 from the tide gauge in Toulon.

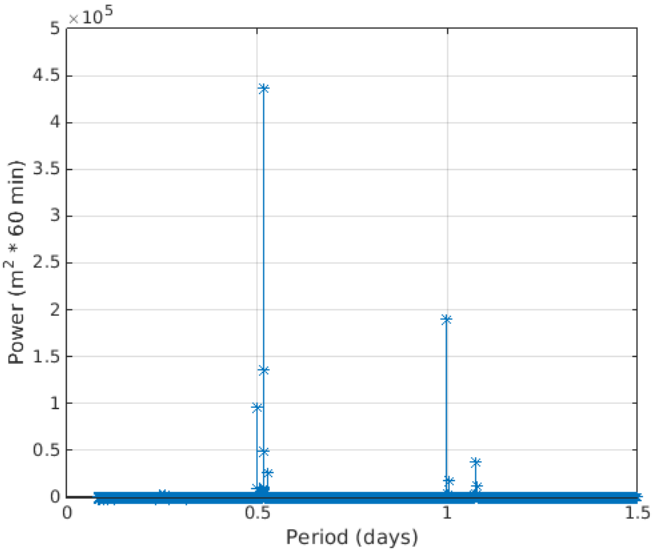

Figure 2.14: Focalization of the diurnal and semidiurnal tidal frequencies for 2009 and 2010 from the tide gauge in Toulon.

A spectra has been done to confirm the importance of diurnal and semidiurnal tides (Fig. 2.14) and some non-tidal frequencies have been found.

Chapter 3

Analysis of observed time series

Only three of these pressure observations are enough long for a study. For this reason the research has been concentrated on three observation series lines: L1, L3 and L8. The observed series from 22 May 2008 to 31 January 2014. A removal of the spikes, an analysis of the gaps and a filling have been performed on the whole period. It has been selected a time interval in a way to guarantee a sort of cyclicity of the phenomena under study. The chosen period is as longest as possible with the available data that is from 1 January 2009 to 31 December 2013. On the selected interval has been performed initially two methods of detiding, a three days averaging and a Doodson Filter. To the detiding followed a detrending. Finally, it has been inverted the order, applying firstly a detrending and subsequently a detiding. Another method of detiding has been applied here, that means an harmonic analysis. These analysis was possible only for limited periods of time.

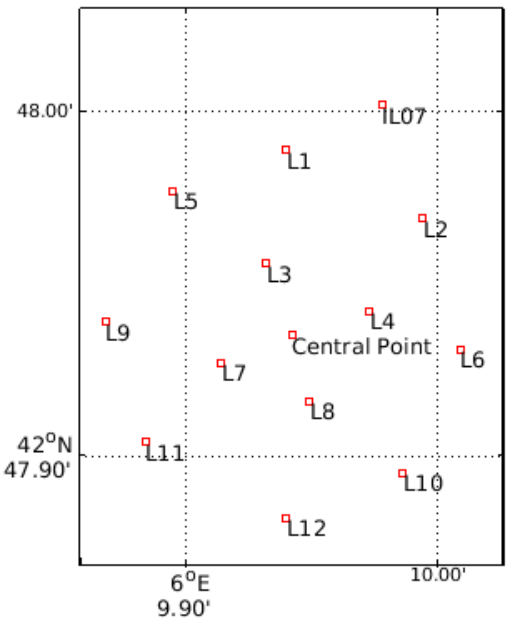

Figure 3.1: Position of the twelve lines by Antares.

Problem	Action	Result	Data set
Spikes	Removal(instrument errors)	Despiked data set	22 May 2008-31 January 2014
Steps	Calibration	Averaged data set	22 May 2008-31 January 2014
Temporal gaps	Filling	Reconstructed Time Series (RTS)	22 May 2008-31 January 2014
Tides 1	Three days average	Detided series (3 days frequency)	4 January 2009-30 December 2013
Tides 2	Doodson Filter	Detided series (daily frequency)	2 January 2009-30 December 2013
Trend 1	Detrending on averaged series (Tides 1)	Detrended series (3 days frequency)	4 January 2009-30 December 2013
Trend 2	Detrending on filtered series (Tides 2)	Detrended series (daily frequency)	2 January 2009-30 December 2013
Trend	Detrending	Detrended series (30 minutes frequency)	1 January 2009-31 December 2013
Tides 1	Three days average	Detided series (3 days frequency)	4 January 2009-30 December 2013
Tides 2	Doodson Filter	Detided series (daily frequency)	2 January 2009-30 December 2013
Tides 3	Harmonic Analysis	Detided intervals (30 minutes frequency)	2 May 2013-18 May 2013; 29 July 2013-29 September 2013

Table 3.1: Schematic of the processing chain used to generate the final RTS for the analysis.

3.1 Negative and positive spikes

The three series presented a large number of negative spikes similar to each other. This spikes have been taken out thanks to a despiking function. The L8 series presented four different positive spikes too. In this case it has been necessary to

apply an ad hoc function before the negative despiking to identify and remove them. In the initial files there were some repeated data probably due to rewriting mistakes. This problem has been solved before the despiking removing the data in which pressure data and date data were the same. Every despiking added gaps of 3 hours.

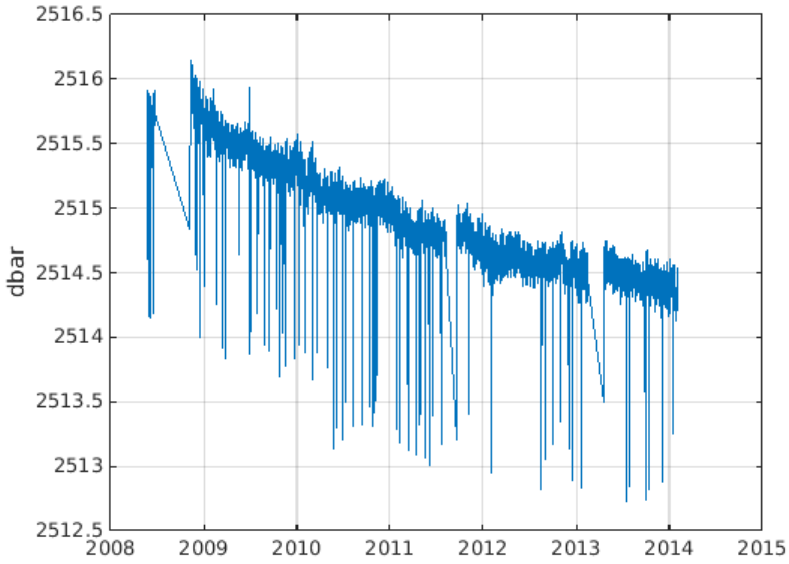

Figure 3.2: L1 series with spikes from 22 May 2008 to 31 January 2014.

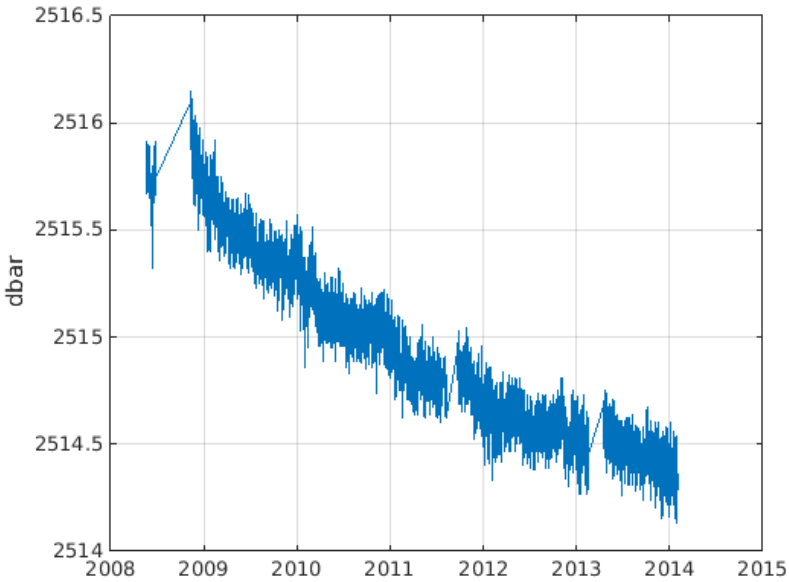

Figure 3.3: L1 series despiked from 22 May 2008 to 31 January 2014.

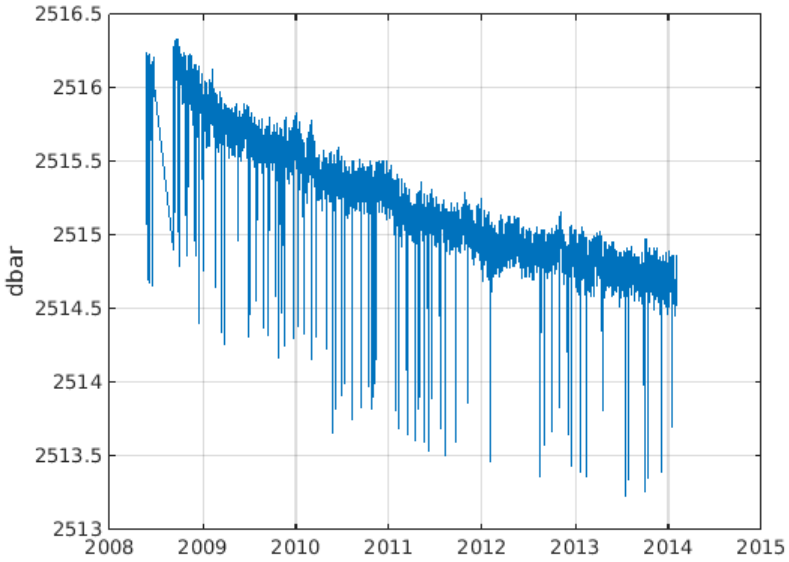

Figure 3.4: L3 series with spikes from 22 May 2008 to 31 January 2014.

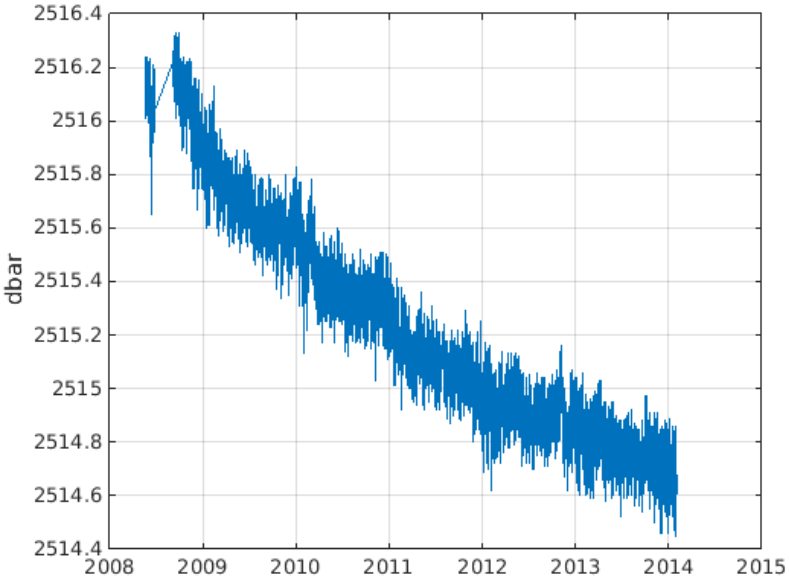

Figure 3.5: L3 series despiked from 22 May 2008 to 31 January 2014.

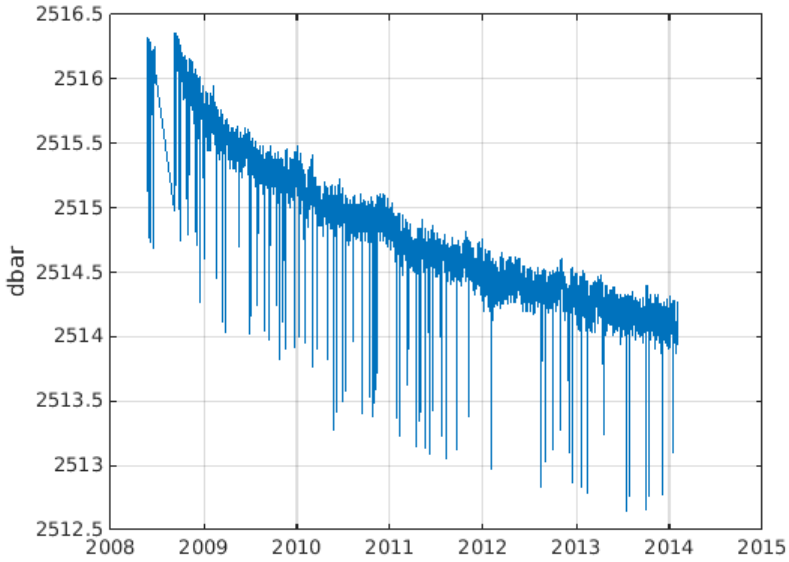

Figure 3.6: L8 series with spikes from 22 May 2008 to 31 January 2014.

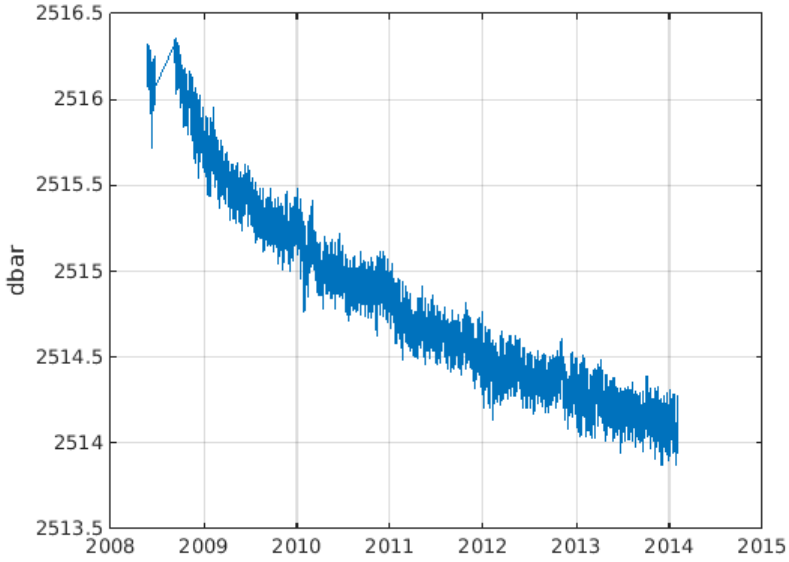

Figure 3.7: L8 series despiked from 22 May 2008 to 31 January 2014.

3.2 Data transmission steps

The frequency of the data set is about 2 minutes but the series shows steps due to the data transmission method. In fact the pressure sensor transmits the observed

data to the coastal station only when the observed value is higher than the instruments sensitivity (0.01 dbar). A calibration has been carried out averaging every 30 minutes. The calculated values have been allocated to the middle point of the averaging interval. As a matter of example, if the first averaging has been calculated from 23.45 to 00.15, the averaged value will be assigned to 00.00. For that reason the frequency of data is 30 minutes and the last data point will be at 23.30 of each day. The condition is that the average is done only if there are a minimum of 8 data points in the interval, i.e. 70% of the total. If not, the data in the interval are deleted.

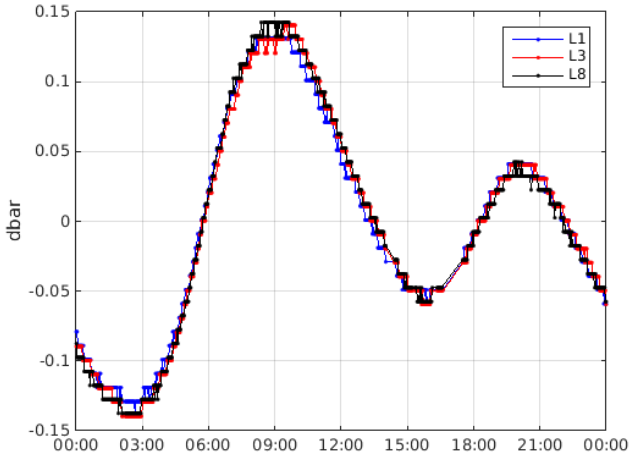

Figure 3.8: Overlay of L1, L3 and L8 series on the 19 November 2009.

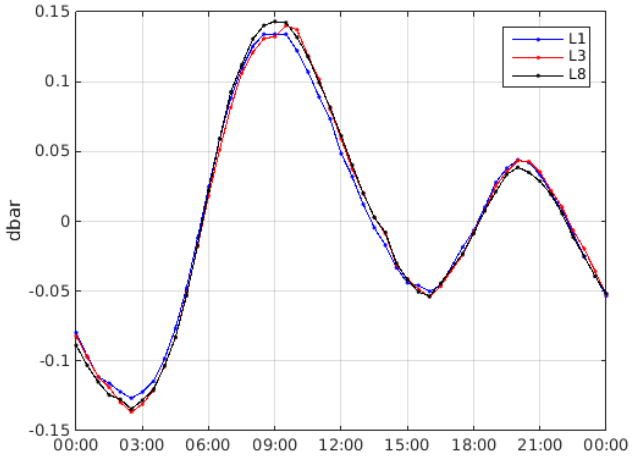

Figure 3.9: Overlay of 30 minutes averaged L1, L3, L8 series on the 19 November 2009.

3.3 Temporal gaps filling

A study of the gaps in the three series L1, L3 and L8 has been carried out. First of all it has been noticed that in some intervals the three series were complementary. Thus, it was chosen to try to complete the gaps of one time series with the data of the others. This method can be justified because the ANTARES lines are positioned at about 70 m distance on a plateau, where it can be assumed that the phenomena recorded are the same in the three stations and sea level changes are spatially uniform.

The series with the gap and the full series are taken from 6 hours before and after the gap. A mean on each series is done. The incomplete series is completed with that data of the 'full series' and reconstructed adding the mean previously subtracted.

An example of filling from 27 May 2009 to 29 May 2009 is shown in Fig. 3.10 and Fig. 3.11. L1 and L3 series show a gap from 27 May 2009 at 19.00 to 28 May 2009 10.00. The gap in L8 series is on the 28 May 2009 from 7.00 to 10.00. Here L8 series completes L1 and L3 series. Three series with a smaller gap, the L8 series three hours gap, are obtained.

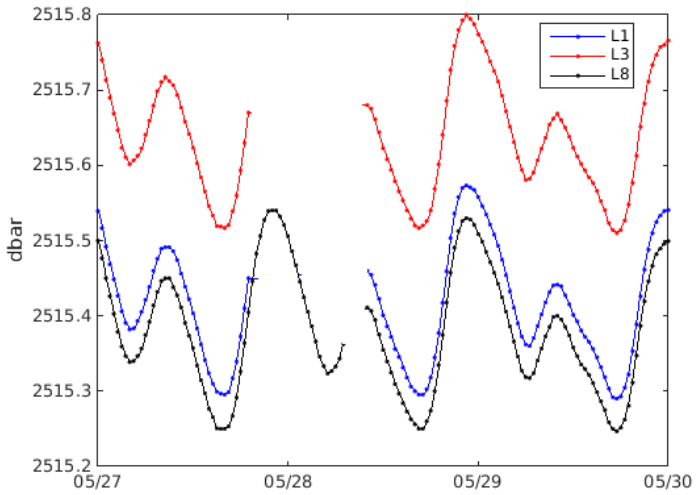

Figure 3.10: Original series L1, L3 and L8. From 27 May 2009 at 19.00 to 29 May 2009 at 10.00 is present a gap in the series L1 and L3. In this case L8 is able partially to complete as it has a gap on the 28 May 2009 from 7.00 to 10.00.

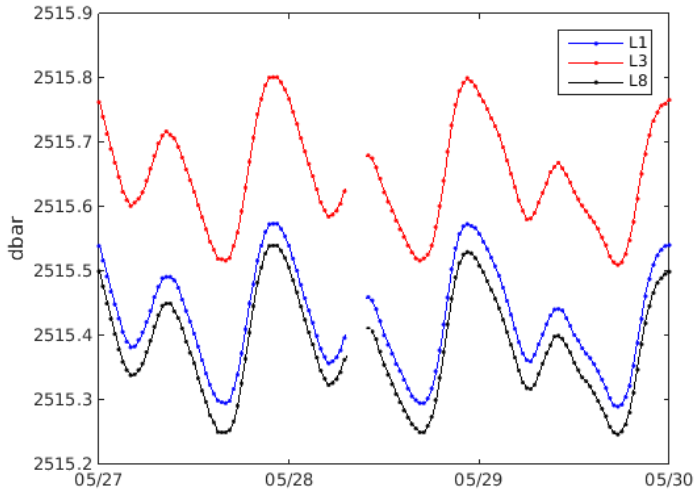

Figure 3.11: Example of filled series. The series L1 and L3 are completed with the series L8. Now only a gap on the 28 May 2009 from 7.00 to 10.00 is in the series.

A posterior quality control has been done. A one day gap has been created in an interval in which the observed data were known and the reconstructed time series has been evaluated. A Root-Mean-Square Deviation evaluation has been done for some chosen intervals. In particular, in the example below, it has been created a gap in the L8 series. The lack has been completed firstly with L1 series and secondly with L8 series. In Tab. 3.2 are some cases.

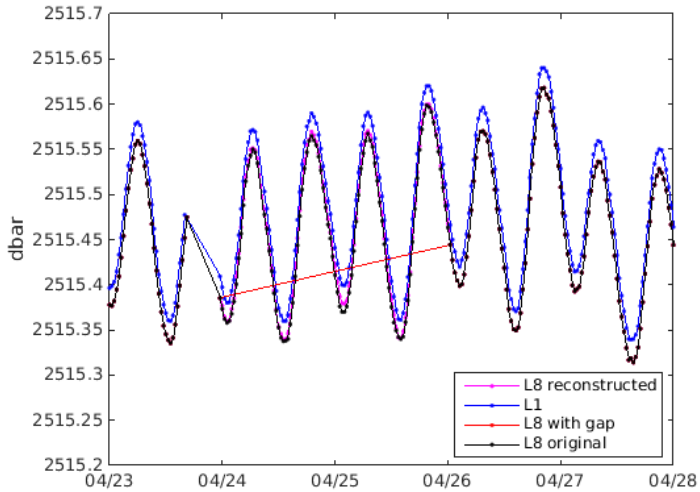

Figure 3.12: Reconstruction of L8 from L1. A gap has been created on 24 and 25 April 2009. The red line is the interval in which a gap has been created.

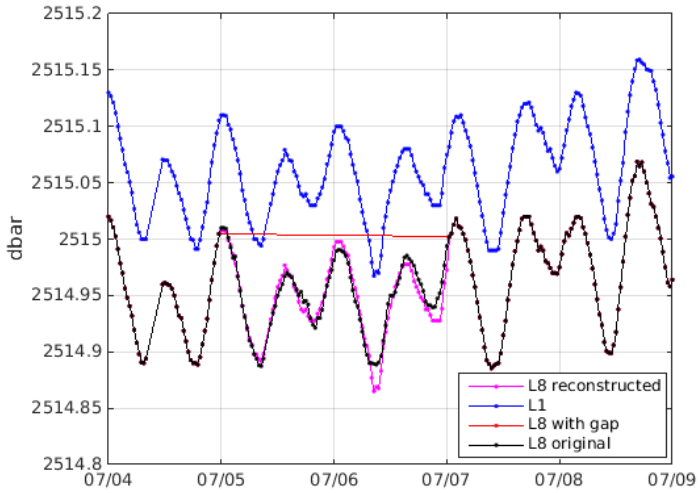

Figure 3.13: Reconstruction of L8 from L1. A gap has been created on 5 and 6 April 2010. The red line is the interval in which a gap has been created.

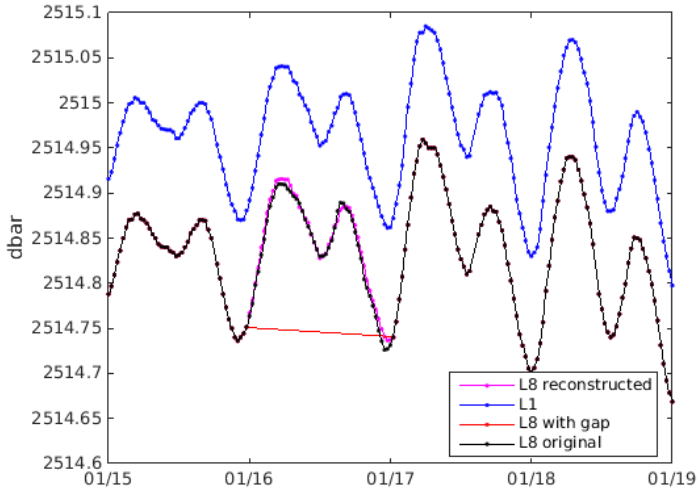

Figure 3.14: Reconstruction of L8 from L1. A gap has been created on 16 January 2011. The red line is the interval in which a gap has been created.

The RMSD has been calculated

$$RMSD = \sqrt{\frac{\sum_{i=1}^{N} (p_i - pr_i)^2}{N}} \tag{3.1}$$

where p_i is the original series interval and pr_i is the reconstructed series interval.

Lines	Created gap	RMSE (dbar)
L8 reconstructed from L1	24/04/2009-26/04/2009	0.0038
L8 reconstructed from L3	24/04/2009-26/04/2009	0.0031
L8 reconstructed from L1	05/07/2010-07/07/2010	0.0058
L8 reconstructed from L3	05/07/2010-07/07/2010	0.0048
L8 reconstructed from L1	16/07/2011-17/07/2011	0.0035
L8 reconstructed from L3	16/07/2011-17/07/2011	0.0043

Table 3.2: Root-Mean-Square Deviation of L8 original interval and L8 reconstructed interval. RMSD has been calculated from the day before to the day after the gap.

The reconstruction can be considered reliable.

3.3.1 Temporal gap analysis

The filling of these three series leads to the composition of an unique series called RTS (Reconstructed Time Series). This series will be nominally positioned in the central point of the ANTARES observatory, that is 42°47.935'N, 6°09.942'E, 2478m depth. It is now possible to study the remaining gaps of the RTS.

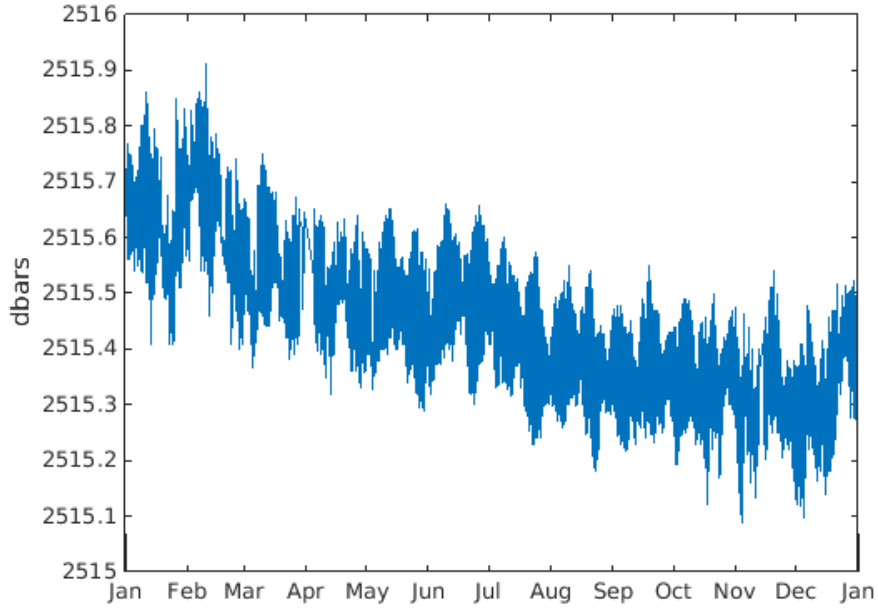

Figure 3.15: RTS in 2009

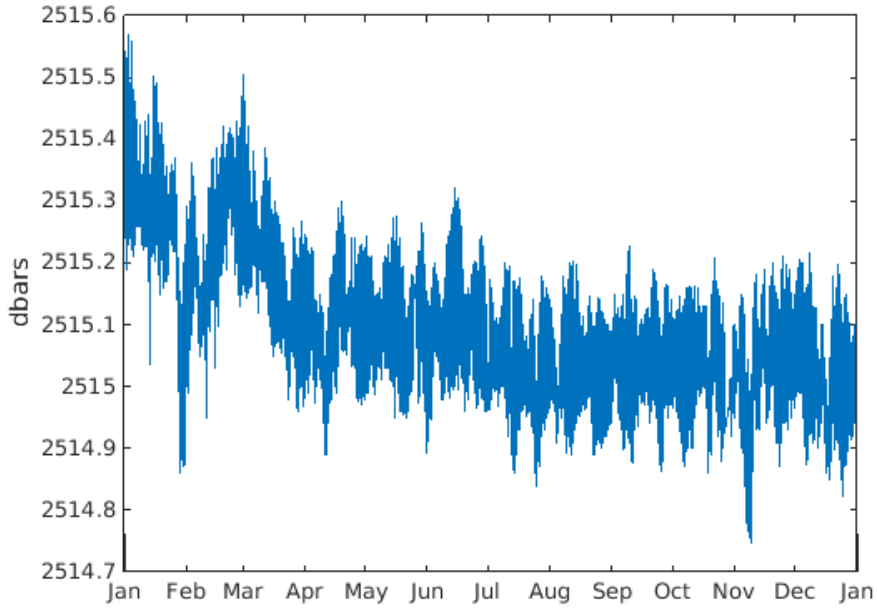

Figure 3.16: RTS in 2010

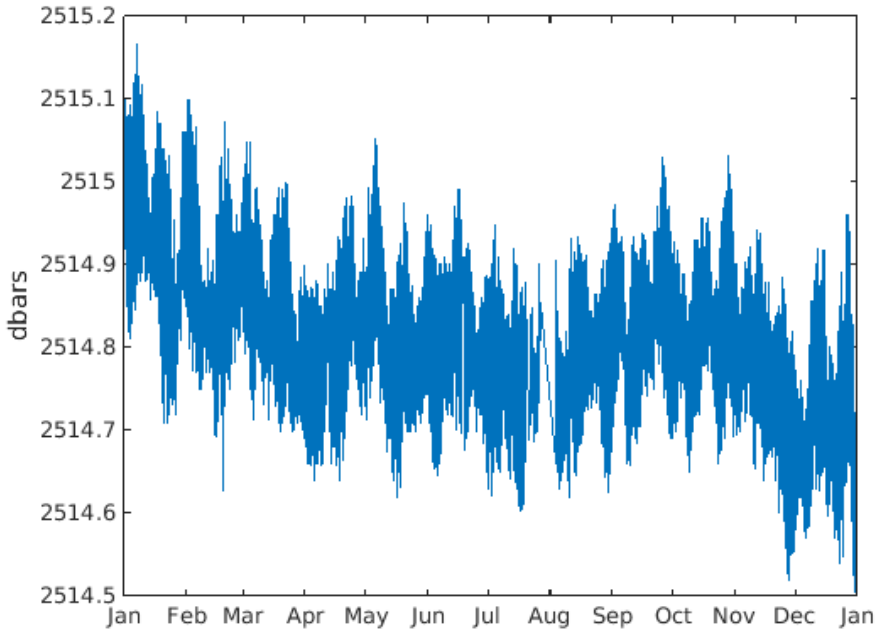

Figure 3.17: RTS in 2011

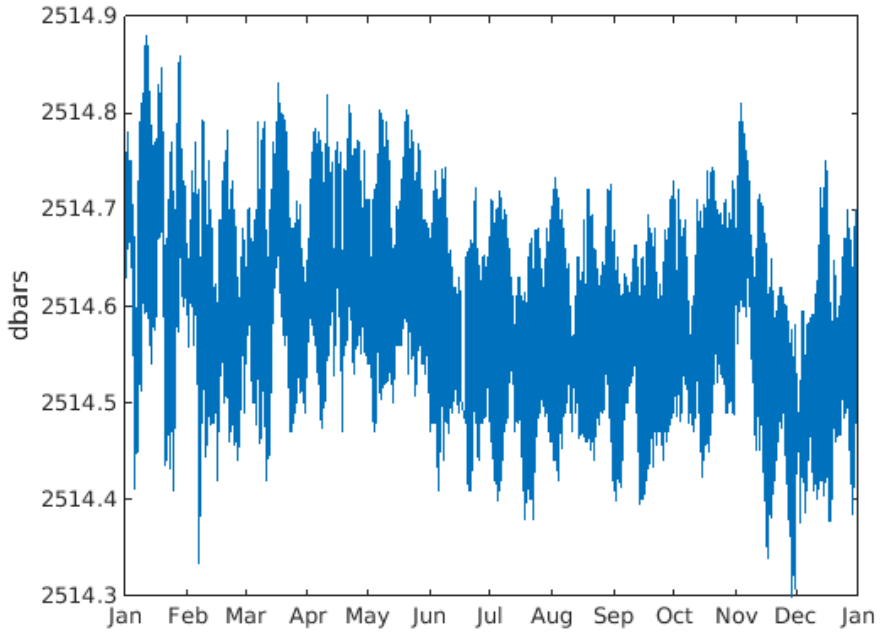

Figure 3.18: RTS in 2012

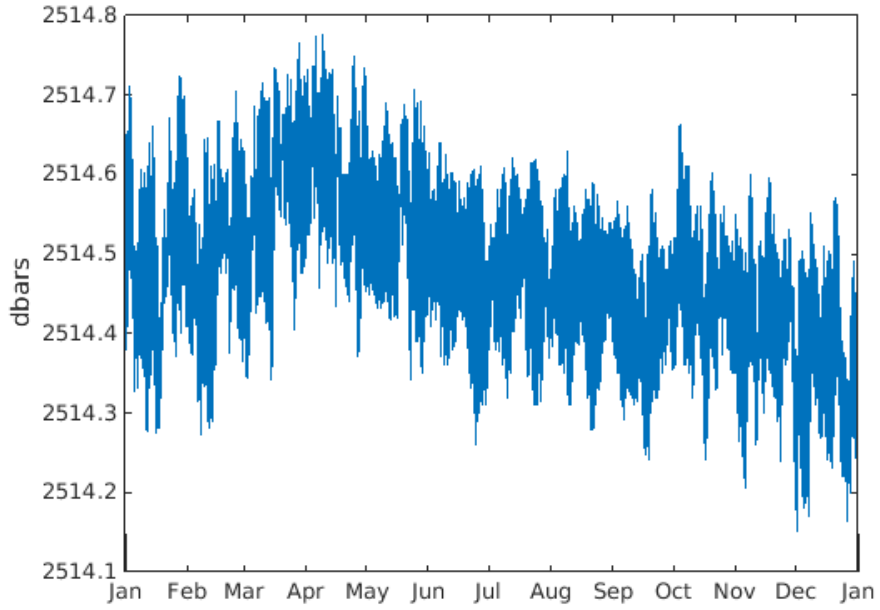

Figure 3.19: RTS in 2013

In the RTS from the 22 May 2008 to the 31 January 2014 there are 436 interruptions bigger than one hour with respect to 90710 data points. The Tab. 3.3 shows the detailed results.

Interruption range	Number of interruptions	Percentage
$>$ 1 hour	436	0.48065
from 1 to 3 hours	247	0.27237
from 3 to 6 hours	85	0.09370
from 6 to 12 hours	51	0.05622
from 12 to 24 hours	31	0.03418
from 1 to 2 days	16	0.01764
from 2 to 3 days	3	0.00331
from 3 to 4 days	0	0
from 4 to 5 days	1	0.00110
$>$ 5 days	2	0.00220

Table 3.3: RTS gaps bigger than 1 hour for the data set from 22 May 2008 to 31 December 2014. $Percentage = \frac{number\ of\ gaps}{number\ of\ total\ data\ in\ the\ interval}$.

	Subinterval of data	Total hours of gap	Length of the data set(days)	Percentage of gaps
1	14/07/10-01/09/10	7.5	48	0.65
2	22/09/10-21/10/10	7	29	1.01
3	18/12/10-27/01/11	4.5	40	0.49
4	19/06/11-19/07/11	6	30	0.83
5	31/08/11-27/10/11	9.5	57	0.69
6	05/11/11-31/01/12	7	87	0.34
7	17/03/12-30/04/12	3	44	0.28
8	05/10/12-10/12/12	20.5	66	1.29
9	17/12/12-22/01/13	1.5	36	0.17
10	18/02/13-16/04/13	5.5	57	0.40
11	02/05/13-18/07/13	1.5	77	0.08
12	29/07/13-29/09/13	1.5	62	0.10
13	24/10/13-31/12/13	8	68	0.49

Table 3.4: Selected subintervals in the RTS that cover a long period of time and with few gaps. $Percentage\ of\ gaps = \frac{total\ hours\ of\ gap}{length\ of\ the\ data\ set\ in\ hours} \times 100$.

There seems to be an improvement in the instrumentation data collection, indeed the number of gaps (considering gaps bigger than one hour) decrease from year to year. These gaps in 2009 are 134, in 2010 are 91, in 2011 are 58, in 2012 are 50 and in 2013 are 23. The total RTS has been analyzed to find subintervals characterised

by few gaps for a period around two months. This selection will be used later to do the detiding using harmonic analysis. 13 subintervals have been identified. In the first column of Tab. 3.4 are some intervals that apparently contain few gaps for a long period. The second column shows the total hours of gaps in the selected interval and the third column represent the number of days in the set. The last column is the percentage of gaps with respect to the length of the series.

3.4 Detiding

3.4.1 Three days average

The first detiding method simply consists in averaging on three days. The main tides in the Mediterranean Sea are the diurnal and the semidiurnal tides with periods around the 12 and the 24 hour and that justifies the choice of three days averaging. The method used in Sec. 3.2 for averaging returns observed data with frequency of 30 minutes. The condition is that the minimum data for applying the averaging on three days is 100 data, that is about 70% of th 144 total data in three days. The RTS obtained has a frequency of three days.

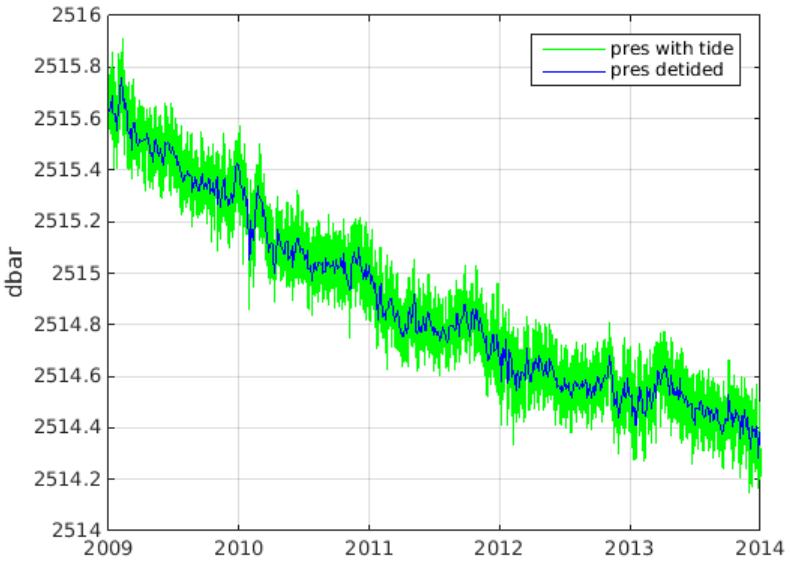

Figure 3.20: Overlay of RTS and detided RTS averaging on three days.

Figure 3.21: Detided RTS averaging on three days.

3.4.2 Doodson filter X0

The Doodson filter was firstly proposed by Arthur Thomas Doodson (1921) and extended by Pugh (1987). The Doodson X0 filter consists in daily means from hourly data obtained applying a low-pass filter. The purpose of this filter is to remove the main tidal frequencies from hourly sea level elevations obtaining a mean value for each day.

$$X_F(t) = \frac{1}{30}\left\{F_0 \cdot X(t) + \sum_{m=1}^{19} F(m) \cdot [X(t+m) + X(t-m)]\right\} \tag{3.2}$$

where $X(t)$ is the central element, with t=12:00 h. F_0 is the weight of the central element and is 0. This element is replaced with the weighted average of all the elements of the window in the 19 hour before and after this value.

The filter is:

$$F(m) = (2, 1, 1, 2, 0, 1, 1, 0, 2, 0, 1, 1, 0, 1, 0, 0, 1, 0, 1) \tag{3.3}$$

which is symmetric $F(m) = F(-m)$.

The observations of RTS have a frequency of half hour. As described, for apply Doodson filter hourly observations are required. Hourly data are obtained averaging and the value obtained has been given to the beginning of each hour.

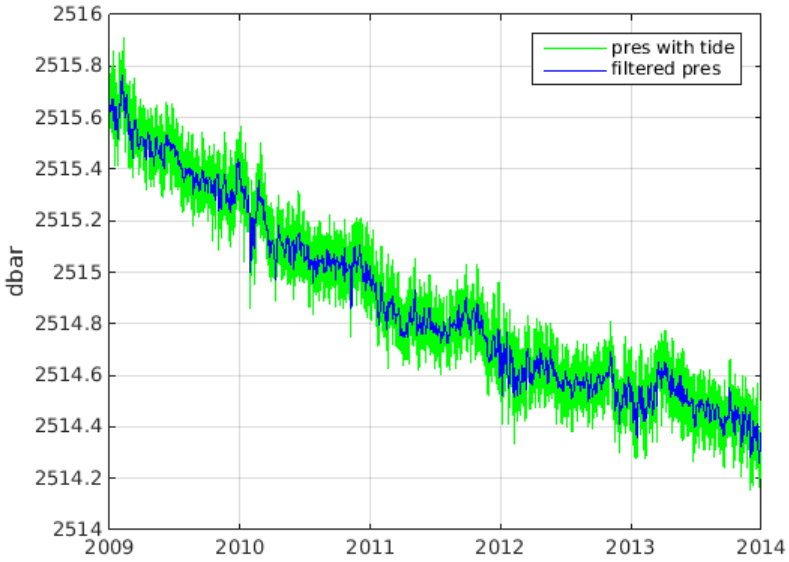

Figure 3.22: Overlay of RTS and detided RTS using Doodson Filter.

Figure 3.23: Detided RTS using Doodson Filter.

3.5 Detrending

The series presented an apparent long-drift. The mathematical representation of this drift is:

$$p_{drift} = -p_1 t + p_4 - p_2 e^{-p_3 t} \tag{3.4}$$

where p_1 describes the slope of the series, $p_2 e^{-p_3 t}$ the exponential growth and p_4 the intercept with the ordinate axis. The detrended series results from $P_{observed} - P_{drift}$.

3.5.1 Detrending on three days averaged

At the detided series, obtained averaging on three days, has been applied this function. The resultant coefficients are $p_1 = -0.0007\, dbar\, days^{-1}$, $p_2 = -5\, dbar$, $p_3 = 0.0004\, dbar\, days^{-}1$, $p_4 = 2511\, dbar$.

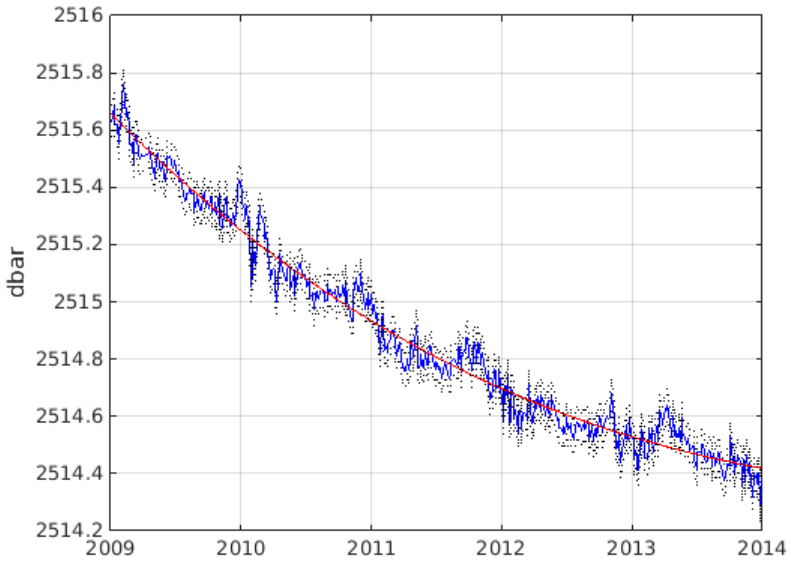

Figure 3.24: Detided RTS and its trend. $RMSD = 0.0541 dbars$.

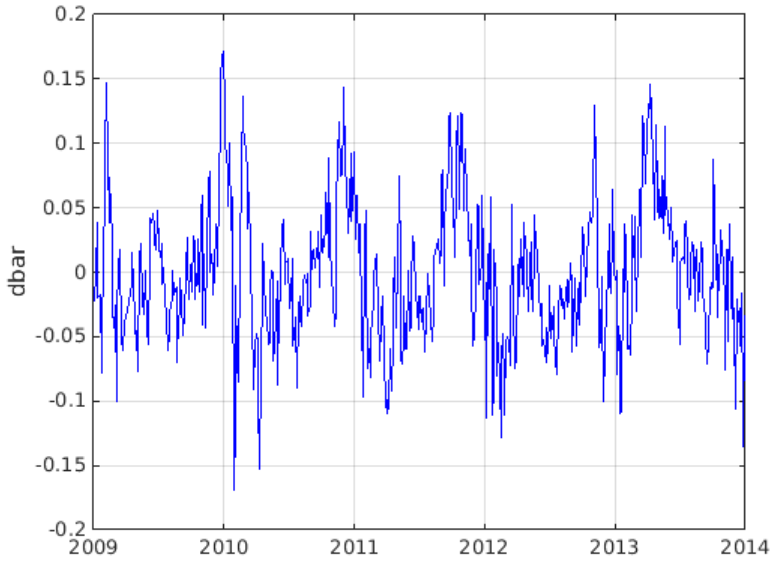

Figure 3.25: Detided averaging and detrended RTS

3.5.2 Detrending on series detided with Doodson filter

The function applied to the series detided with Doodson method gives coefficients $p_1 = -0.0010\,dbar\,days^{-1}$, $p_2 = -6.99\,dbar$, $p_3 = 0.0003\,dbar\,days^{-1}$, $p_4 = 2509\,dbar$.

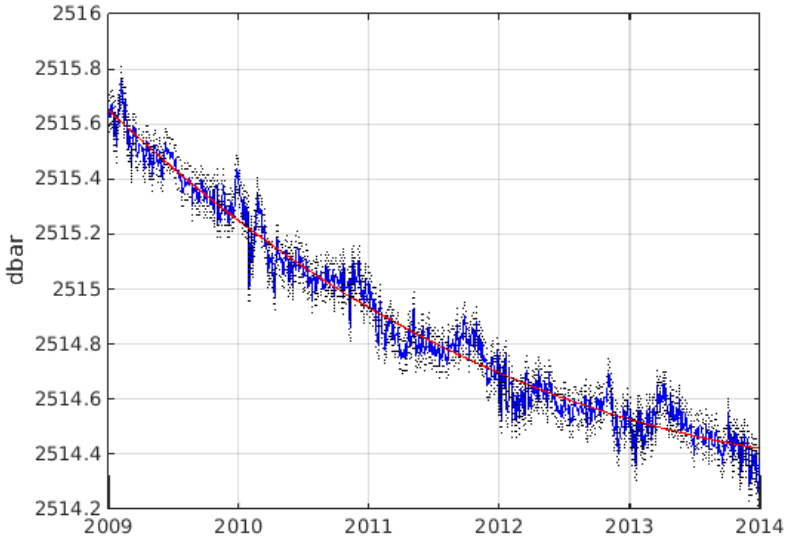

Figure 3.26: Detided RTS and its trend. $RMSD = 0.0569 dbars$.

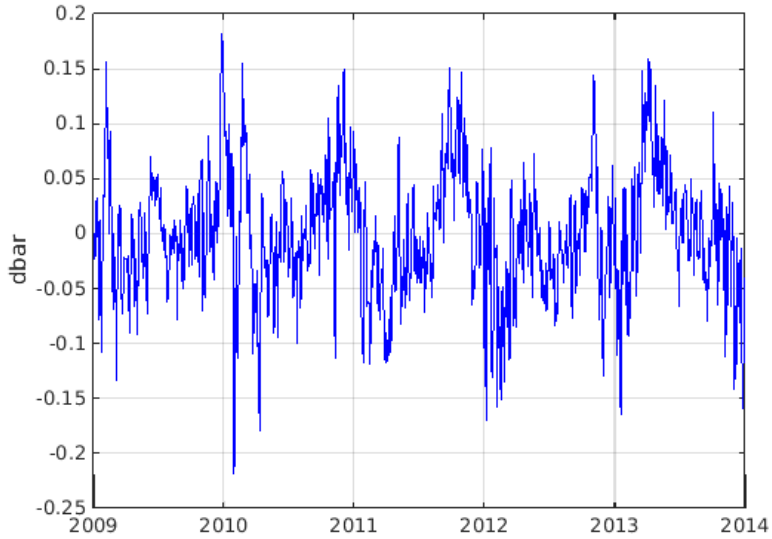

Figure 3.27: Detided filtering and detrended RTS

3.5.3 Intercomparison of trends

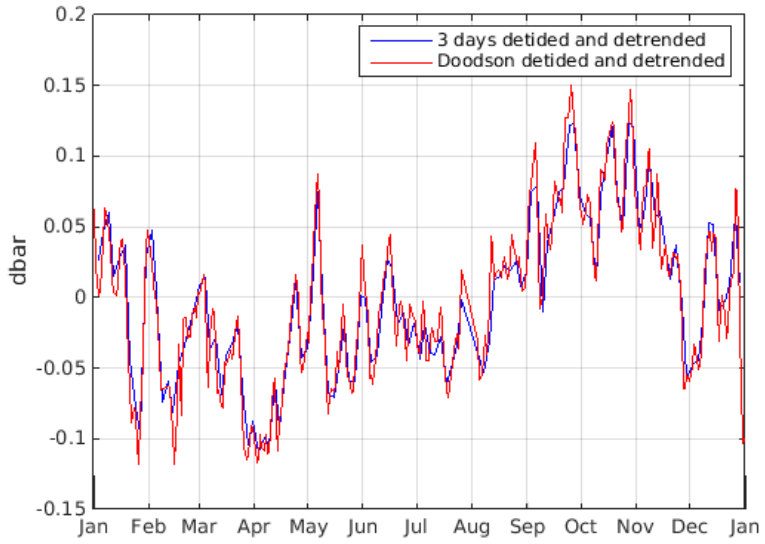

Figure 3.28: Intercomparison between detided and detrended series in 2011 with the two methods. The blue line represents the averaged RTS. The red line represents the filtered RTS.

The RMSD=0.0136 dbars on the five years 2009-2013.

coefficients	3d average	Doodson	
p_1	-0.0007	-0.0011	$dbar\,days^{-1}$
p_2	-4.7595	-7.0677	$dbar$
p_3	0.0004	0.0003	$dbar\,days{-}1$
p_4	2510.9	2508.6	$dbar$

Table 3.5: Values of the coefficients that describe the trends for the averaged RTS and the filtered RTS.

3.6 Coupled detrending-detiding

In this section it will be inverted the order of working doing firstly the detrending and secondly the detiding.

3.6.1 Detrending

Here it has been done the detrending on RTS (Sec. 3.3.1). The data set has a frequency of 30 minutes and covers a period of 5 years from 01 January 2009 to 31 December 2013. The frequencies of the tides are still in the series.

The values of the coefficients that describe the trend are $p_1 = -0.0007\,dbar\,minutes^{-1}$, $p_2 = -4.91\,dbar$, $p_3 = 0.0004\,dbar\,minutes^{-1}$, $p_4 = 2510\,dbar$.

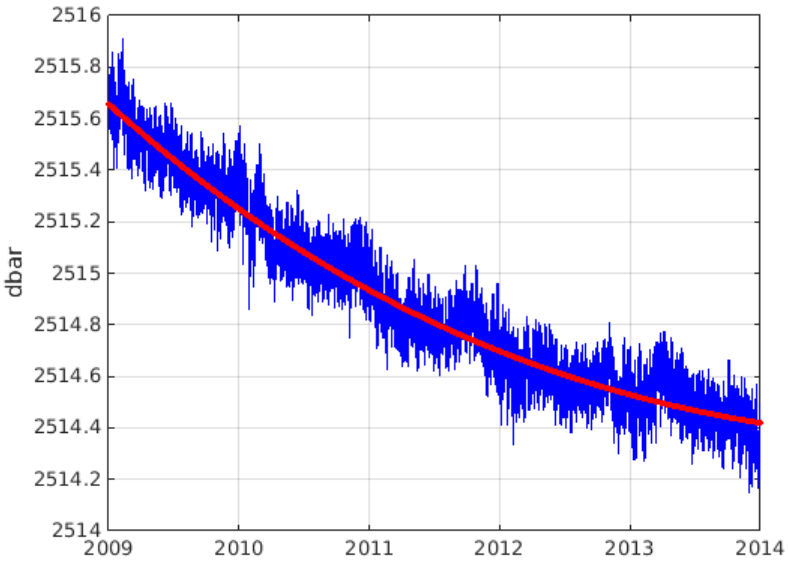

Figure 3.29: RTS with tides and its trend. $RMSD = 0.0871 dbars$.

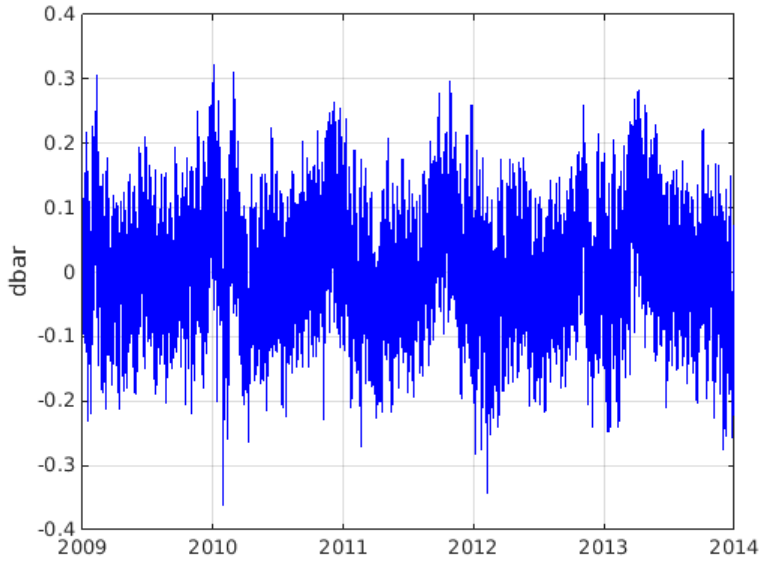

Figure 3.30: Detrended RTS with tides. The frequency of the data point is 30 minutes.

3.6.2 Three days average on detrended series

On the detrended series it has been calculated the mean every three days. In Fig. 3.32 the result. The frequency of the data in the output is three days.

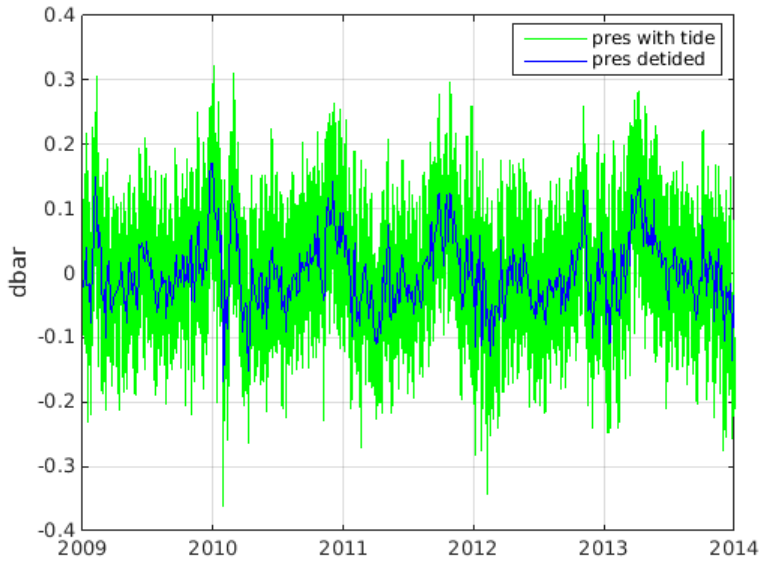

Figure 3.31: RTS with tides and averaged on three days RTS.

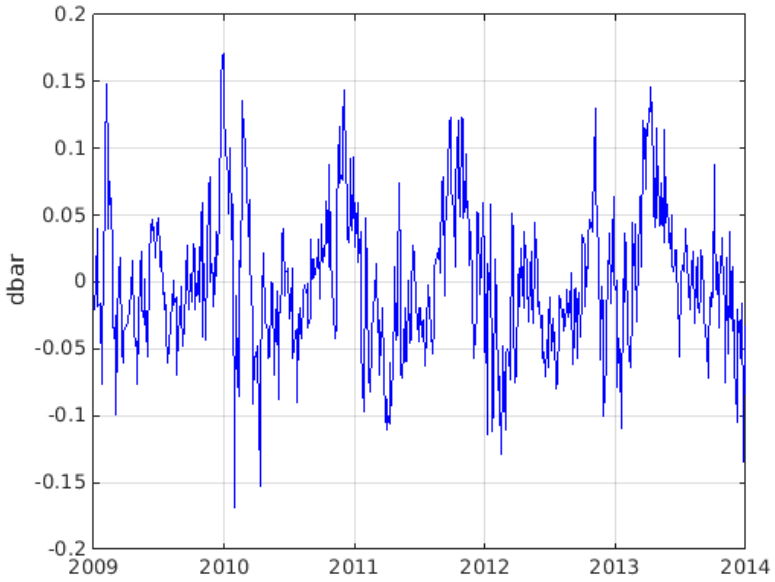

Figure 3.32: Detided RTS averaging. The frequency of the data point is 3 days.

3.6.3 Doodson Filter on detrended series

For applying the Doodson filter it has been necessary to do hourly averaging. The resulting detiding is shown in Fig 3.34, that are daily data on five years.

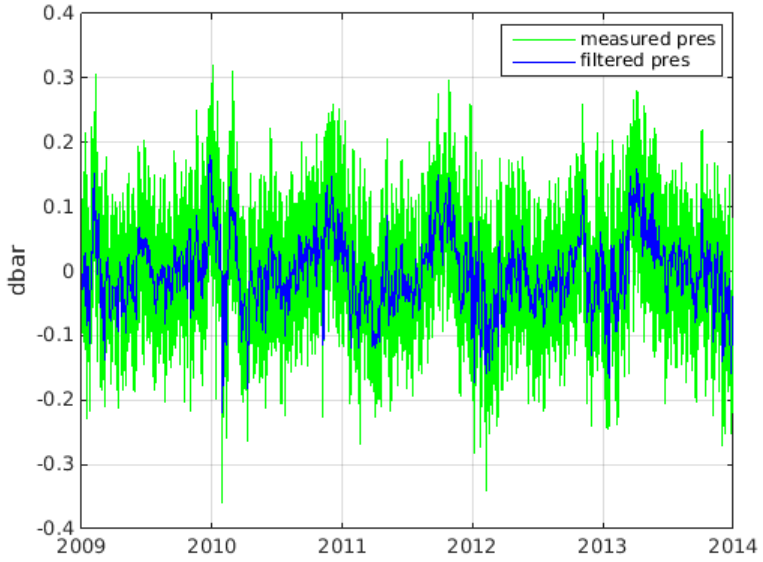

Figure 3.33: RTS with tides and filtered RTS

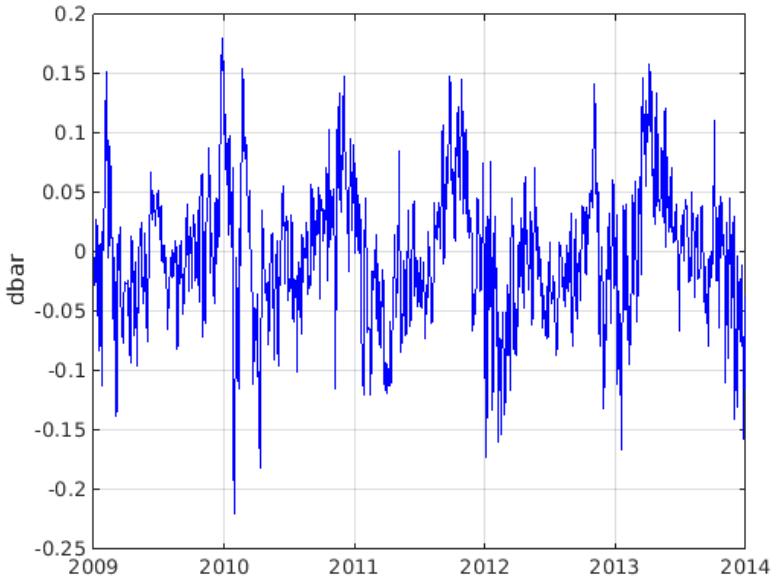

Figure 3.34: Detided RTS with Doodson Filter with daily frequency.

3.6.4 Detrending and detiding with harmonic analysis

An harmonic analysis for the separation of tidal from non-tidal components in a series has been proposed by Rich Pawlowicz in his article (Pawlowicz,2002). The code applied in this section has been made available on line by Pawlowicz and is called T_TIDE. The deterministic nature of tidal processes promotes research of methods to identify astronomical tidal frequencies. The tidal forcing is modelled as a set of spectral lines, that is the sum of a finite set of sinusoids at that frequencies. A least-square fit has been used to determine the relative phase and the amplitude of each frequency. This analysis is typically used for obtaining astronomical tides components for a series of sea surface elevation data. To approach as more as possible at the aim of the code, deep pressure data have been converted in elevation data. The frequency of half an hour of this dataset has been specified in the code as well as the latitude of ANTARES Observatory. The series has been detrended before to prevent the influence of the trend. It has been noticed that gaps played an important role in the analysis, perturbing drastically the research of the frequencies. For that reason it has been decided to concentrate the study on selected intervals (explained in Tab. 3.4). From the analysis of various detided results it has been noticed that the series were well solved for time series of 32 days. A re-reading of Tab. 3.4 has been done to find intervals of 32 days with few gaps.

The output detided series will be $p_{detided} = p_{detrended} - p_{tidal}$ where the tidal series has been constructed from the significant components. To define what components can be considered significant, the code applies a signal-to-noise power ratio (SNR) that is the squared ratio of amplitude to the error of amplitude and uses

those components whose $SNR > 1$ for the construction of the tidal series . The error is calculated analyzing the noise level in spectra: 9 frequencies bands are chosen (bracketing M0, M1...M8). In each band the amplitude of the residual power spectrum is estimated. It is then assumed that this noise contaminates the components of the harmonic fit. Errors are determined through a linearized analysis in which variances are summed (for more details see T_TIDE code).

NAME	INTERVAL RANGE	GAP ($hour\, days^{-1}$)
Interval 1	18/12/2012-18/01/2013	1.5
Interval 2	19/02/2013-22/03/2013	3.5
Interval 3	02/05/2013-02/06/2013	2.5
Interval 4	03/06/2013-04/07/2013	1.5
Interval 5	30/07/2013-30/08/2013	1.5
Interval 6	25/10/2013-25/11/2013	2

Table 3.6: Sub-intervals selected for the harmonic analysis.

In the next figures the calculated tidal harmonic wave and the detided series together with the starting series are plotted:

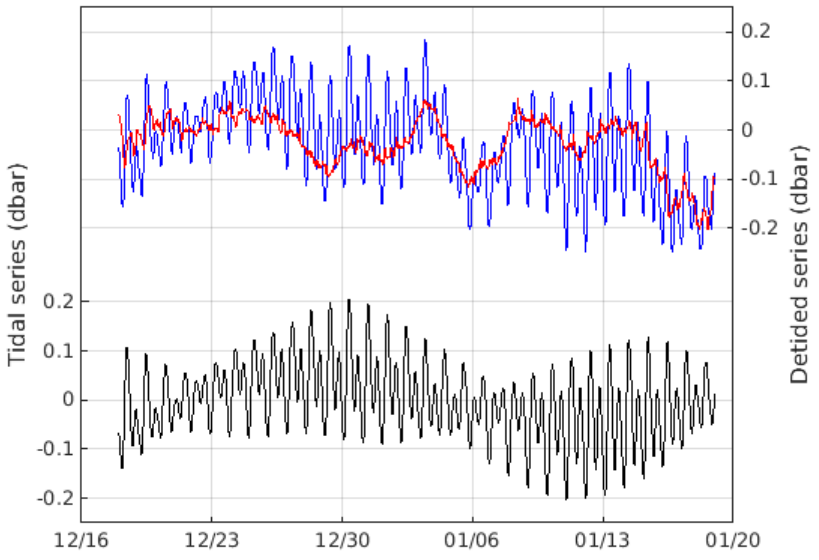

Figure 3.35: The blue line represents the observed bottom pressure, the black line represents the tidal series and the red line represents the detided series for the interval 1 (18/12/2012-18/01/2013).

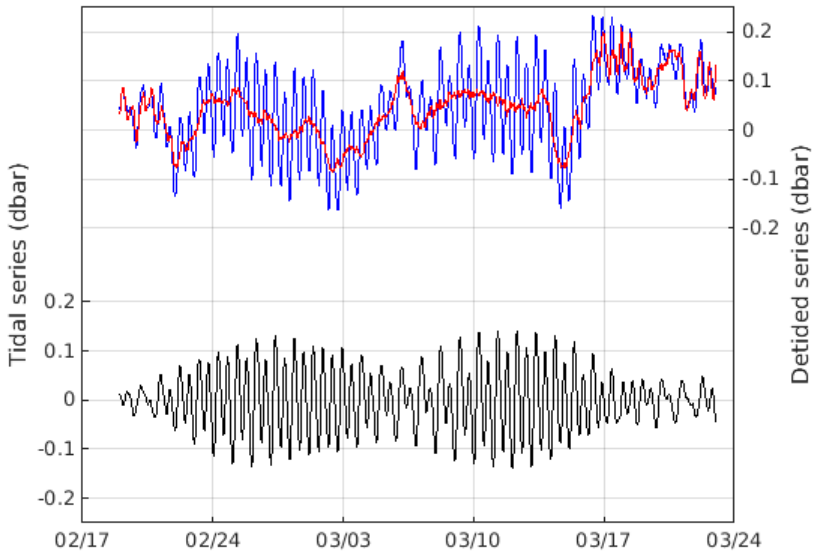

Figure 3.36: The blue line represents the observed bottom pressure, the black line represents the tidal series and the red line represents the detided series for the interval 2 (19/02/2013-22/03/2013).

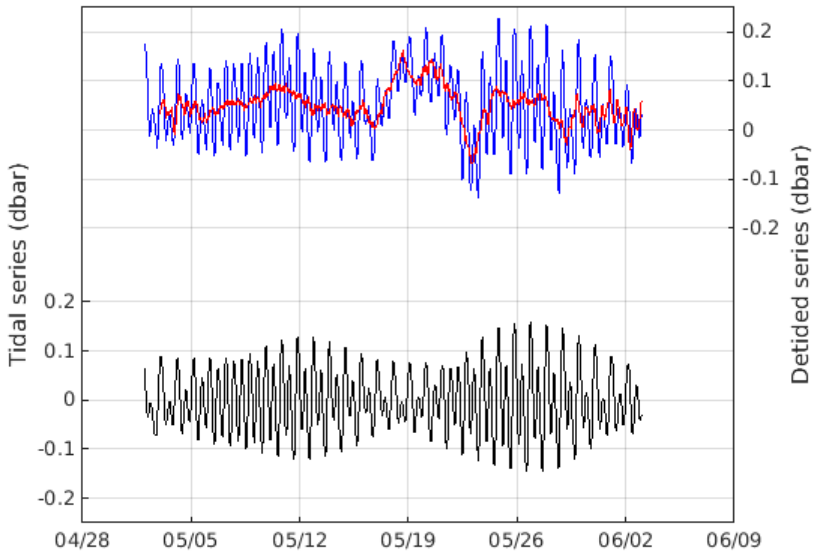

Figure 3.37: The blue line represents the observed bottom pressure, the black line represents the tidal series and the red line represents the detided series for the interval 3 (02/05/2013-02/06/2013).

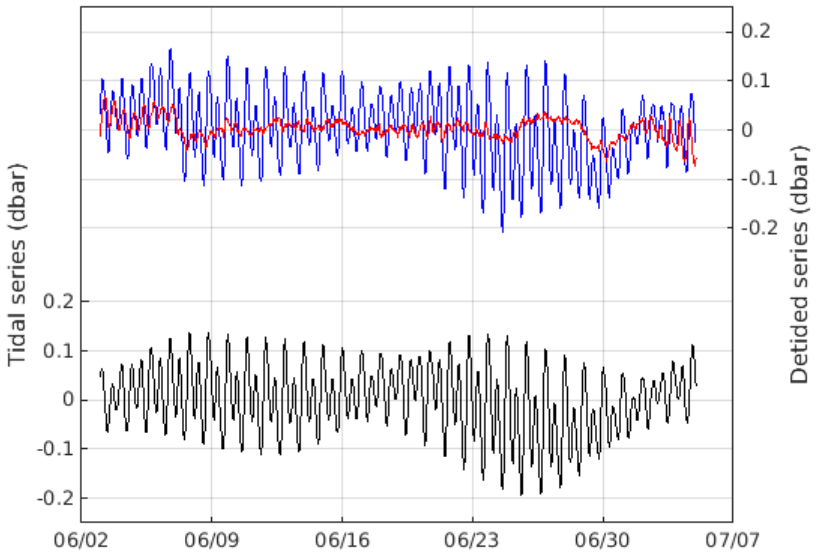

Figure 3.38: The blue line represents the observed bottom pressure, the black line represents the tidal series and the red line represents the detided series for the interval 4 (03/06/2013-04/07/2013).

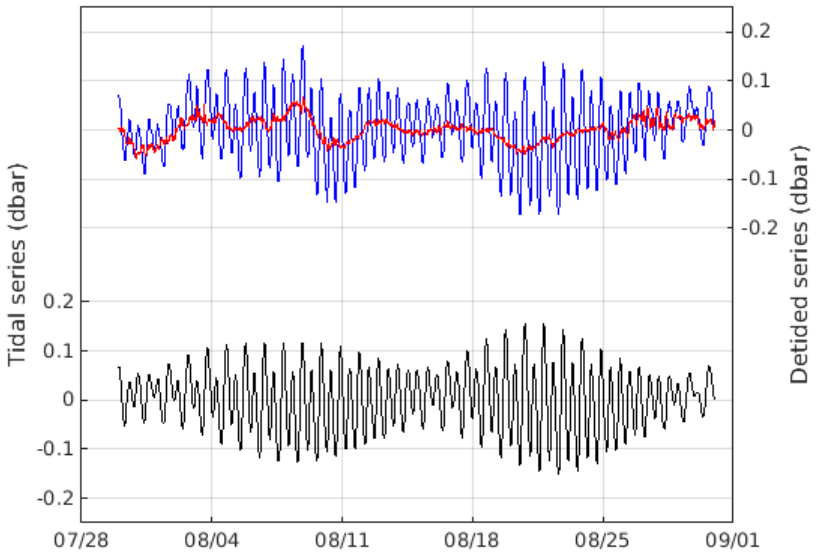

Figure 3.39: The blue line represents the observed bottom pressure, the black line represents the tidal series and the red line represents the detided series for the interval 5 (30/07/2013-30/08/2013).

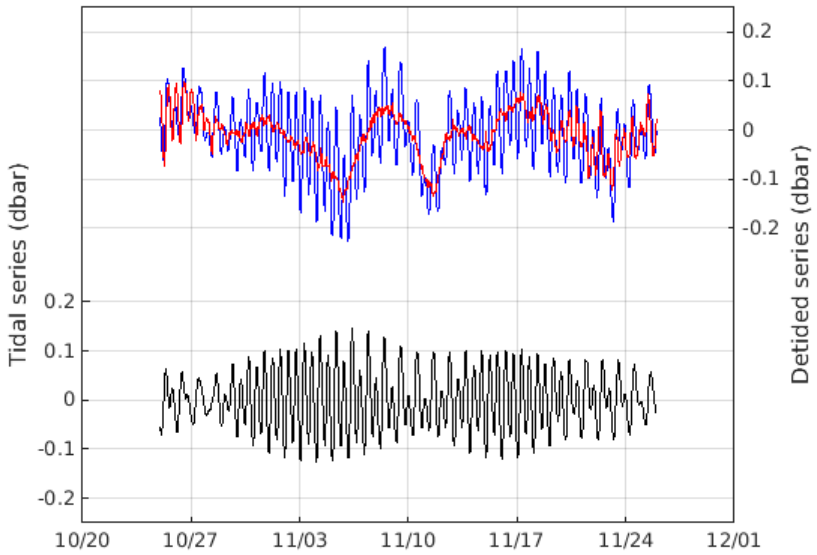

Figure 3.40: The blue line represents the observed bottom pressure, the black line represents the tidal series and the red line represents the detided series for the interval 6 (25/10/2013-25/11/2013).

The intervals 1,3 and 5 can be considered the best detided cases and provide important informations about the observed series. The intervals 2, 4 and 6 show a worst analysis particularly on the boundaries; however the central part of the series is in line with the result expected.

Tab. 3.7, 3.8 and 3.9 show the amplitude of the main components in the six intervals.

NAME	PERIOD(hours)	AMPLITUDE 1(dbar)	AMPLITUDE 2(dbar)
MM	661.30	0.0505 ± 0.038	
Q1	26.87	0.0009 ± 0.0009	0.0063 ± 0.003
O1	25.82	0.0155 ± 0.0009	0.0192 ± 0.003
P1	24.07	0.0129 ± 0.0009	0.0108 ± 0.003
K1	23.93	0.0389 ± 0.0009	0.0327 ± 0.003
N2	12.66	0.0165 ± 0.001	0.0166 ± 0.002
M2	12.42	0.0676 ± 0.001	0.0655 ± 0.002
S2	12.00	0.0388 ± 0.001	0.0346 ± 0.002
K2	11.97	0.0106 ± 0.001	0.0094 ± 0.002
M4	6.21	0.0051 ± 0.0009	0.0051 ± 0.0009
MS4	6.10	0.0032 ± 0.0009	0.0042 ± 0.0009

Table 3.7: Amplitude values of the main components from the harmonic analysis of the intervals 1 and 2.

NAME	PERIOD(hours)	AMPLITUDE 3(dbar)	AMPLITUDE 4(dbar)
MM	661.30		0.0265 ± 0.005
Q1	26.87	0.0065 ± 0.004	0.0044 ± 0.001
O1	25.82	0.0225 ± 0.004	0.0188 ± 0.001
P1	24.07	0.0102 ± 0.004	0.0108 ± 0.001
K1	23.93	0.0309 ± 0.004	0.0327 ± 0.001
N2	12.66	0.0201 ± 0.002	0.0149 ± 0.002
M2	12.42	0.0636 ± 0.002	0.0666 ± 0.002
S2	12.00	0.0291 ± 0.002	0.0324 ± 0.002
K2	11.97	0.0079 ± 0.002	0.0088 ± 0.002
M4	6.21	0.0031 ± 0.0009	0.0042 ± 0.0009
MS4	6.10	0.0017 ± 0.0009	0.0030 ± 0.0009

Table 3.8: Amplitude values of the main components from the harmonic analysis of the intervals 3 and 4.

NAME	PERIOD(hours)	AMPLITUDE 5(dbar)	AMPLITUDE 6(dbar)
MM	661.30		
Q1	26.87	0.0034 ± 0.0009	0.0045 ± 0.003
O1	25.82	0.0172 ± 0.0009	0.0129 ± 0.003
P1	24.07	0.0111 ± 0.0009	0.0094 ± 0.003
K1	23.93	0.0334 ± 0.0009	0.0284 ± 0.003
N2	12.66	0.0133 ± 0.0006	0.0155 ± 0.002
M2	12.42	0.0690 ± 0.0006	0.0602 ± 0.002
S2	12.00	0.0322 ± 0.0006	0.0364 ± 0.002
K2	11.97	0.0088 ± 0.0006	0.0099 ± 0.002
M4	6.21	0.0054 ± 0.0006	0.0045 ± 0.001
MS4	6.10	0.0042 ± 0.0006	0.0037 ± 0.001

Table 3.9: Amplitude values of the main components from the harmonic analysis on the intervals 5 and 6.

It has just been explained the importance of the continuity of the series, that is the presence of few gaps. This last analysis introduces a new requirement, the cyclicity. As said, it has been identified that an interval of 32 days provided good results from the filtering of the observed pressure series. Longer or shorter series didn't show a good detiding. Observing the periods of the main components in Tab. 3.7, 3.8 and 3.9, there are four diurnal components, four semi-diurnal components and two components around six hours. An arithmetic mean of that main components produces an effective period of 16.21 hours. That means that every 32.42 hours two effective tidal cycles occur. If the first signal of this hypothetical time series is applied at the 00.00 of the first day, the second will be at about the 8.00 of the next day, then at the 16.00 of the third day and again at 00.00. This cyclicity reaches,

after 23 cycles, 32 days justifying the importance of such a particular data interval. So, for forward studies, it will be important to search intervals that are multiple of 16, or better 32 days for applying the harmonic analysis.

3.7 Intercomparison

3.7.1 Intercomparison between the detiding methods

An intercomparison of the detided series for the sub-intervals available from the harmonic analysis has been done. In particular, the comparison has been done on interval 1, interval 3 and interval 5. The inefficiency of the first method of detiding, the average on three days, is immediately evident. The series, for this case, are too smooth with the lost of possible informations about non-tidal frequencies. For this reason the three days averaging method will be left.

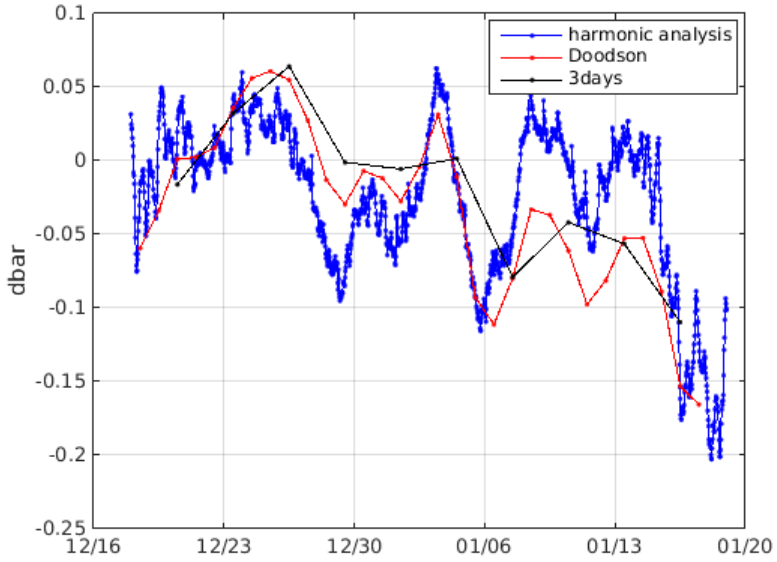

Figure 3.41: Intercomparison between the three different detiding methods for the interval 1 (18/12/2012-18/01/2013).

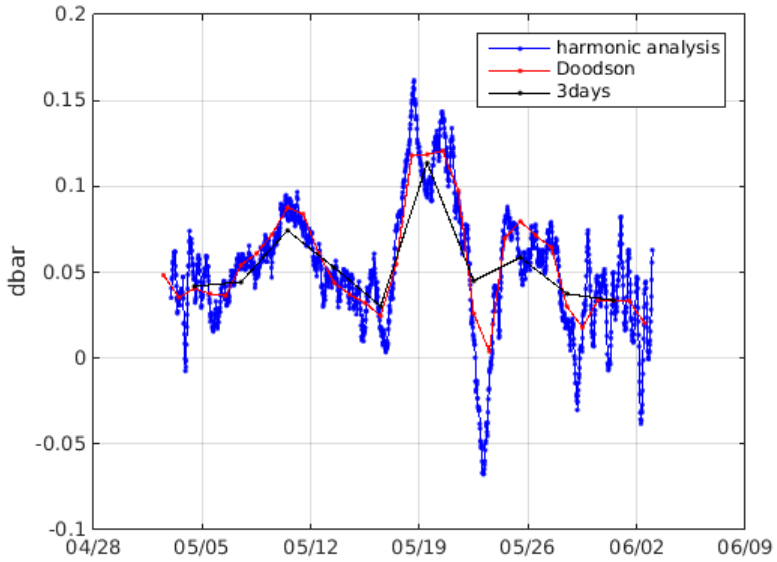

Figure 3.42: Intercomparison between the three different detiding methods for th interval 3 (02/05/2013-02/06/2013).

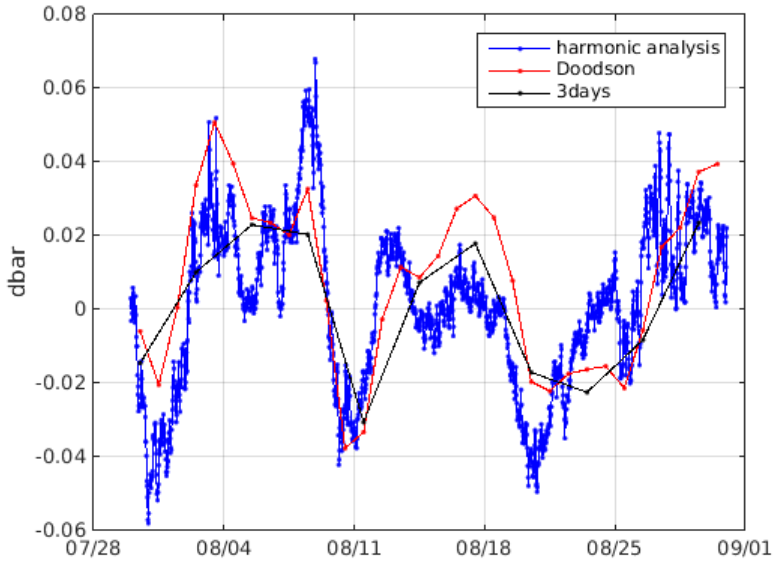

Figure 3.43: Intercomparison between the three different detiding methods for th interval 5 (30/07/2013-30/08/2013).

It follows a comparison between the Doodson method and the harmonic analysis. The starting series is represented as well.

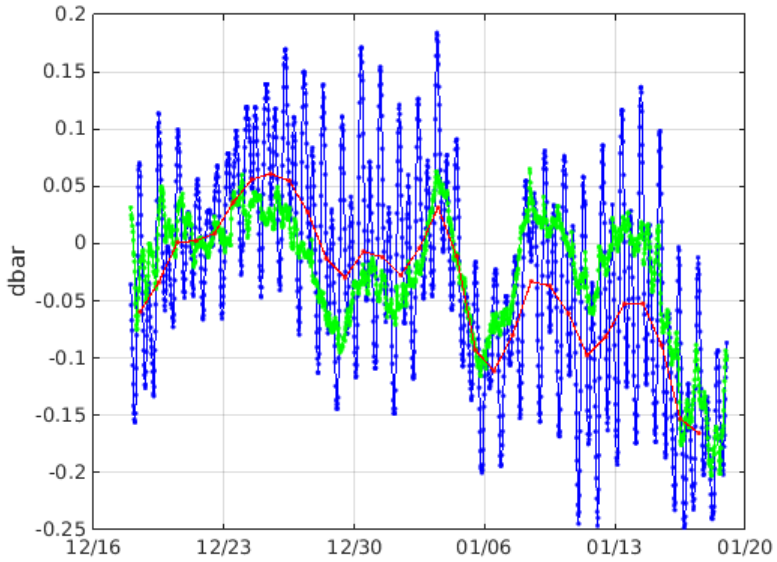

Figure 3.44: The blue line represents the starting RTS with tides. The red line represents the detided RTS with Doodson filter and the green line represents the harmonic analysis for interval 1 (18/12/2012-18/01/2013.

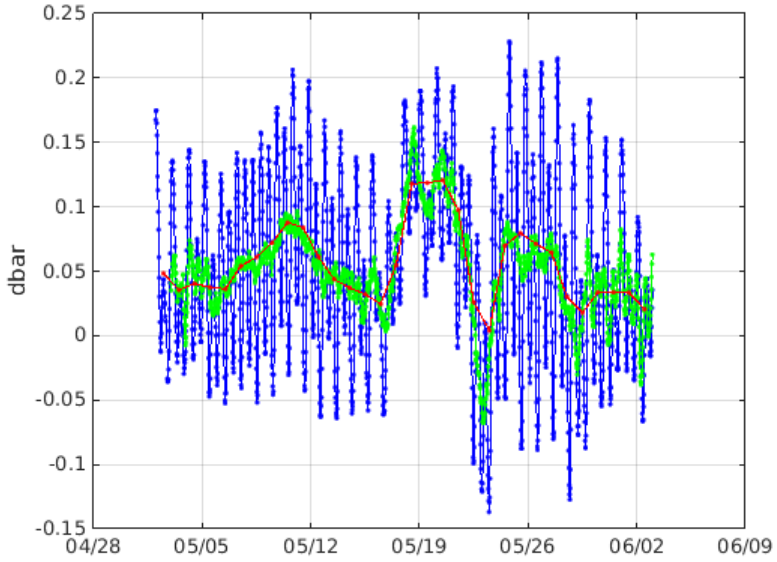

Figure 3.45: The blue line represents the starting RTS with tides. The red line represents the detided RTS with Doodson filter and the green line represents the harmonic analysis for interval 3 (02/05/2013-02/06/2013).

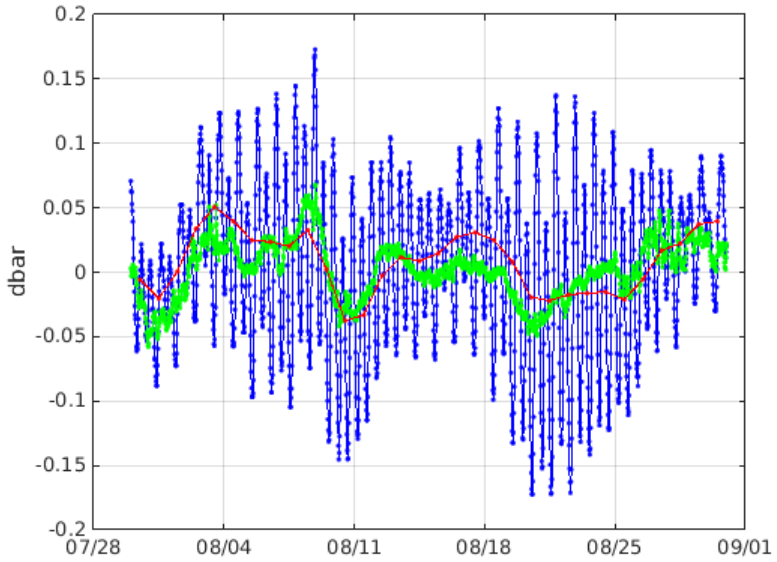

Figure 3.46: The blue line represents the starting RTS with tides. The red line represents the detided RTS with Doodson filter and the green line represents the harmonic analysis for period 5 (30/07/2013-30/08/2013).

Some long frequencies are not recognized by Doodson filter and so not detided. In fact, it is to remember that Doodson filter act only on the most important constants, the diurnal and the semidiurnal tides. Another fact to consider is that an harmonic analysis of about thirty days cannot consider longer frequencies. The limited number of example doesn't permit to clarify the reason of these difference but the solution has probably to be searched in the three months or semi-annual frequencies. Here, it has been possible to apply the harmonic analysis only for short intervals in 2013. The comparison with other intervals in the same season of different years and a further comparison with the original series could give more information about this phenomena. The fact that, in some cases, the Doodson filtered series is well compared with the harmonic analysis justifies the validity given to this method. The desire would be to use the harmonic analysis to continue the study but the limited intervals would make it not representative. For this reason it has been decided to prosecute with the RTS detided through Doodson method. As previously said, the main problems in harmonic analysis are due to the many gaps in the series. Some of them come from the removed spikes that created gaps of three hours, others have no explanation here. However, it is clear that gaps come from instrumentations failure in situ. The analysis of the series in Sec.3.3.1 showed a decreasing of the number of the gaps in the years (134 gaps in 2009, 23 in 2013) probably due to an improvement of data acquisition. This make hope in more continuously data set and will preserve the possibility of a new analysis with harmonic analysis in the next future.

3.7.2 Intercomparison between sea surface and bottom pressure

It is now possible to compare the tide gauge sea surface elevation in Toulon with the bottom pressure observed by ANTARES. The data set is available from 1 January 2008 to 16 October 2013 so that the common interval to analyze is from 1 January 2009 to 15 October 2013. Some data set are represented.

In the Fig. 3.47, 3.48 and 3.49 is evident that the two series are in phase. The standard deviation of the sea surface elevation in Toulon is 0.1131 m, while the standard deviation of bottom pressure by ANTARES is 0.0870 dbar. The relationship between depth and pressure is about 1m:1dbar.

The Pearson correlation coefficient from 1 January 2009 to 15 October 2013 is 0.7172.

$$\rho_{xy} = \frac{\sigma_{xy}}{\sigma_x \sigma_y} \tag{3.5}$$

where σ_{xy} is the covariance and σ_x and σ_y are the standard deviations.

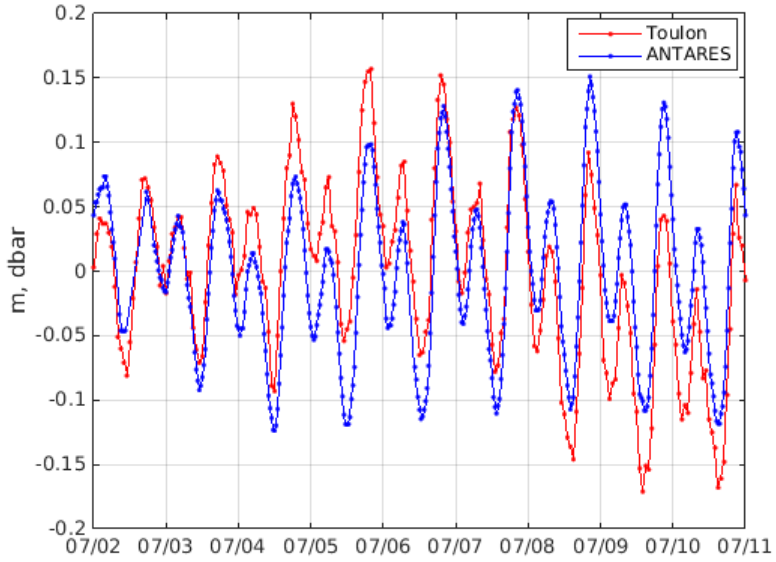

Figure 3.47: Intercomparison between the sea surface elevation at the Toulon tide gauge (m) and bottom pressure by ANTARES (dbar). An extract of the data set from 2 to 10 July 2009.

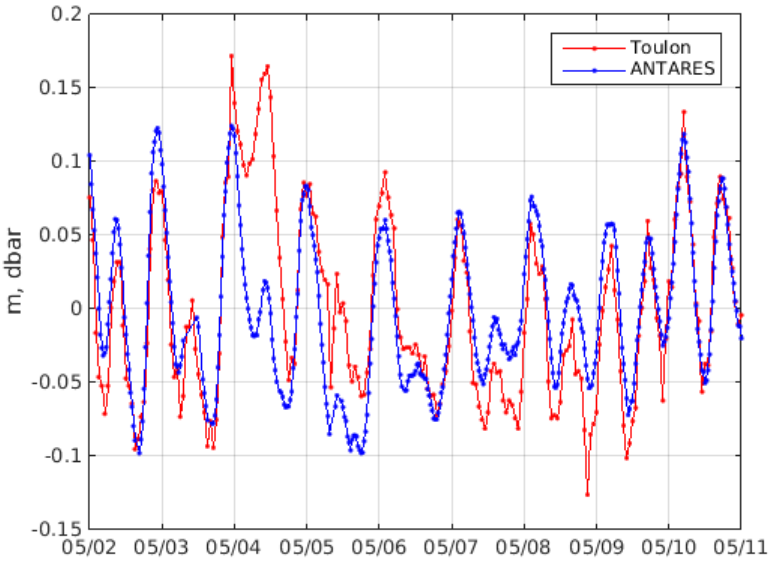

Figure 3.48: Intercomparison between the sea surface elevation at the Toulon tide gauge (m) and bottom pressure by ANTARES (dbar). An extract of the data set from 2 to 10 May 2010.

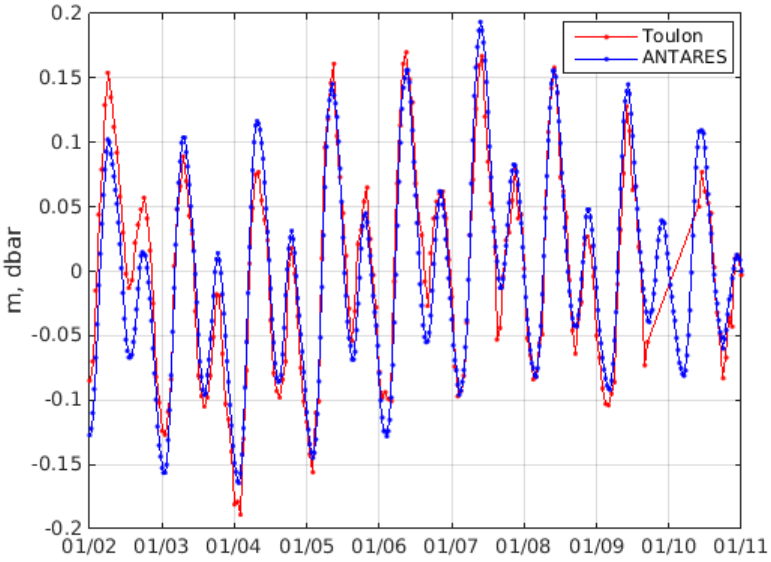

Figure 3.49: Intercomparison between the sea surface elevation at the Toulon tide gauge (m) and bottom pressure by ANTARES (dbar). An extract of the data set from 2 to 10 January 2011.

As said in Sec.2.3 the comparison with tides is very important. They enter, in fact, in the hydrostatic equation and their correlation with the bottom pressure series confirm that this term is the same.

3.8 Spectra

In the Fig. 3.50 are evident the components characterizing the series analyzed. As described in this chapter, this series is the result of a despiking, an averaging over 30 minutes, a filling between three series and a detrending. The Fig. 3.51 focalizes the attention on the main tidal components, the semidiurnal tide and the diurnal tide which are typical of the Mediterranean Sea. A spectra has been done after the detiding through Doodson filter. Fig. 3.52 shows the signals remained in the series and the absence of tides. These remained frequencies are connected with phenomena that strongly shape the circulation in the Gulf Lion. The observation of these signals in deep water at a depth of 2478 m is the first goal of this research by ANTARES.

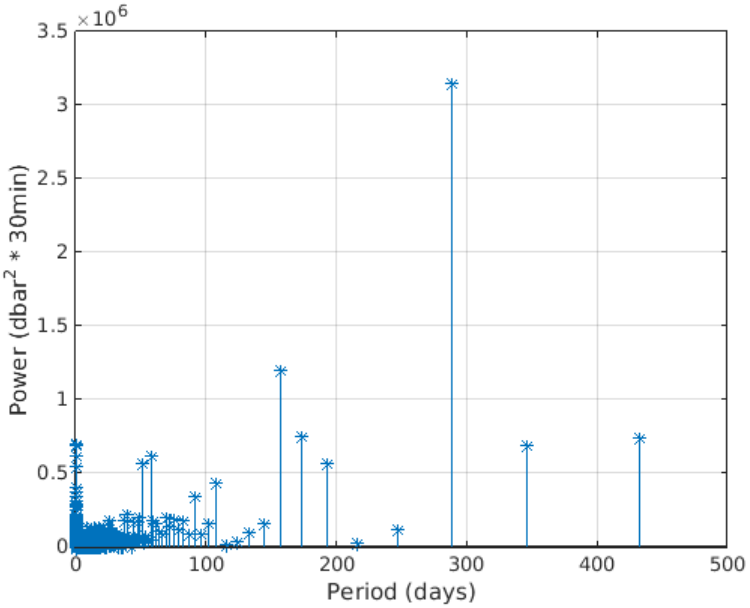

Figure 3.50: RTS with tides and its periods on the whole period of 5 years from 1 January 2009 to 31 December 2013.

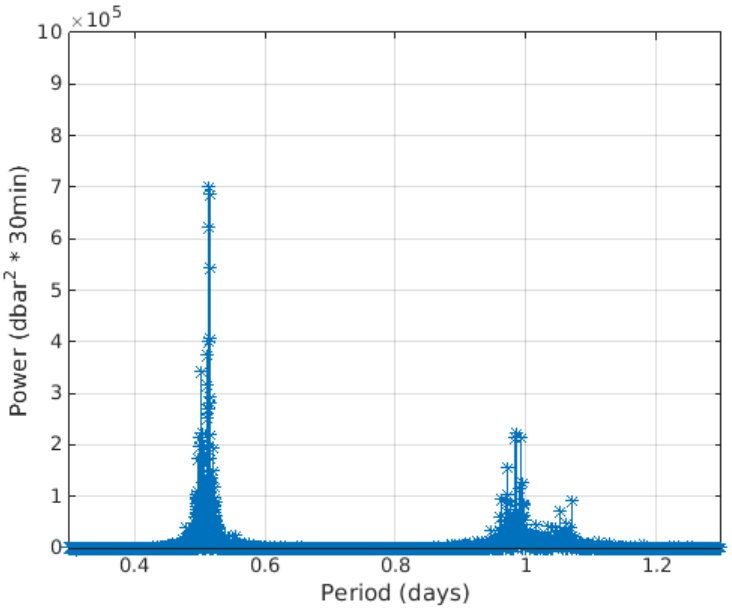

Figure 3.51: Zoom on the RTS with tides. Note the diurnal and semi-diurnal components.

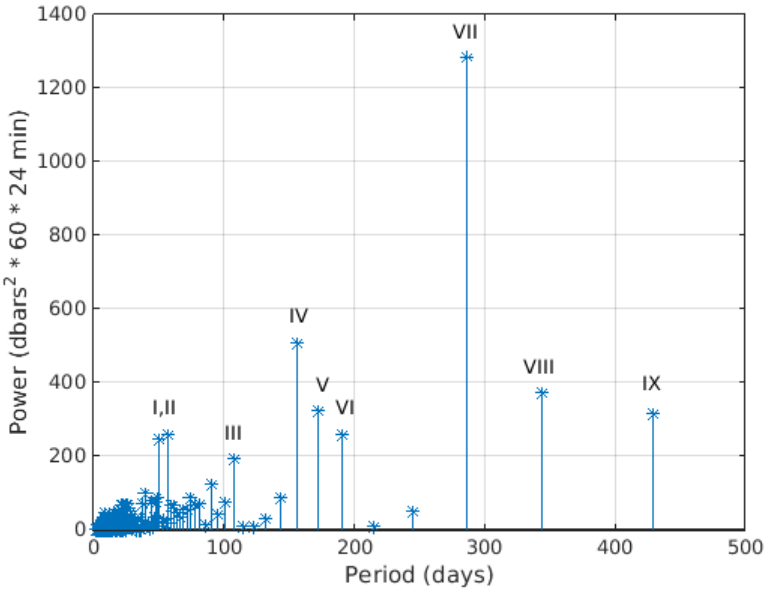

Figure 3.52: Significant frequencies in the series detrended and detided with Doodson filter over the whole temporal series.

The signals identified in the spectra are:

	PERIOD(days)	PHENOMENA
I	51	variations in the Gulf of Lion Gyre
II	57	variations in the Gulf of Lion Gyre
III	107	steric effect
IV	156	steric effect
V	172	steric effect/ Kelvin waved due to the Strait of Gibraltar
VI	191	steric effect/Kelvin waves due to the Strait of Gibraltar
VII	286	Kelvin waves due to the Straits of Gibraltar.
VIII	343	?
IX	429	Chandler wobble

Table 3.10: List of significant phenomena in the observed bottom pressure at the ANTARES observatory. (For reference to Gulf of Lion Gyre see Pinardi et al., 2015)

An investigation of the mean sea level in the Mediterranean Sea (Pinardi et al.,2013) has found that thermal expansion and mass changes may give the same important contribute to the global mean sea level trend. The mean sea level equation (MSLE):

$$\frac{d\langle\eta\rangle}{dt} = -\underbrace{\frac{T_r}{\Omega}}_{1} - \underbrace{\langle q_w\rangle}_{2} - \underbrace{\frac{\rho_f}{\rho_0}\langle\beta S_0 q_w\rangle}_{3} + \underbrace{\frac{1}{\rho_0}\left\langle \alpha_T \frac{Q}{C_w}\right\rangle}_{4} - \underbrace{F_\rho}_{5} \tag{3.6}$$

where term 1 is the net volume transport that changes the mass in the domain, in this case the transport at Gibraltar. Term 2 is the net addition or loss of water by surface processes, the net fluxes. These terms correspond to the mass tendency term and are called incompressible terms. Term 3 is the halosteric effect term, that is the salinity vertical flux. Term 4 is the thermosteric term, that is the heat flux term. Term 5 is the density flux out of the domain, that is the changes of density advected in or out the domain. These three terms are called compressible terms.

The MSLE can be solved as two separate problems, the sum of the incompressible dynamics and the steric contribution

$$\langle\eta\rangle = \langle\eta_i\rangle + \langle\eta_s\rangle \tag{3.7}$$

where

$$\frac{d\langle\eta_i\rangle}{dt} = -\frac{T_r}{\Omega} - \langle q_w\rangle \tag{3.8}$$

and

$$\frac{d\langle\eta_s\rangle}{dt} = -\frac{\rho_f}{\rho_0}\langle\beta S_0 q_w\rangle + \frac{1}{\rho_0}\left\langle \alpha_T \frac{Q}{C_w}\right\rangle - F_\rho \tag{3.9}$$

Pinardi, in her article, explained the role of the MSLE terms for the case of the Mediterranean Sea for a study from 1999 to 2008. The Gibraltar transport and water flux terms are approximately in phase but with opposite sign and their sum show a highly varying stochastic-like term. The steric terms are instead almost periodically around zero. The stochastic-like term regard the mass transport, in particular, the imbalanced equilibrium on seasonal and annual periods between the Gibraltar an the surface water flux. In fact, it is known that on the long period, the Mediterranean Sea loses water from the surface (q_w positive) and receives water from the Atlantic Ocean (T_r negative) and, for a steady state in the long-term mean, this two fluxes balance perfectly each others. This balance is not yet achieved on the annually and seasonally mean and give place to a tendency in the mean sea level.

The other contribution to sea level is due to steric terms, which show a sort of periodicity on seasonal time scales with some anomalies that will be the contributors to the long-term tendency.

In other words, the Mediterranean Sea level tendency is dominated by an almost periodic steric component superimposed on a stochastic-like mass contribution. The stochastic term is the dominant term, giving fluctuations in the range of $\pm 1000\, mm\, yr^{-1}$.

The signal identified by I e II in Tab. 3.10 have periods of about two months. They have been attributed to variations in the gyres of the Gulf of Lion probably due to wind-stress and atmospheric phenomena. These most important wind in this area are the Mistral which blows down from the Rhone Valley (cold and dry), the Levant which comes from the eastern Mediterranean (moist wind), the Tramontane which blows from the Massif Central mountains to the Mediterranean (cold and dry). The Marine blows from the south and is warm and moist. The Scirocco comes from south-east and can bring heavy precipitations.

The signals in the range from three to six months in Fig.3.10 that correspond to III, IV, V an VI have been imputed to the steric effect, that lead to the so called steric sea level. It is due to the changes in the density of the water column that brings to an expansion or a contraction of the column itself. As just said, changes in steric level give an important contribute to local changes in sea level on seasonal scales and also on climatic scales. The colder air brings to a colder and more dense surface water in winter with a consequently contraction of the water column and a decrease of the sea level. On the contrary, the warmer air in summer heat the sea surface; warm and less dense water lead to an expansion of the sea level and an increase of the sea level.

The signals identified as V,VI and VII correspond to periods from 6 to 10 months. This signals are due to the of the Strait of Gibraltar and its influence on the Kelvin waves and by the wind stress that drives the Mediterranean circulation. The Kelvin waves are non-dispersive waves due to the balance of the Coriolis force against the coastline. The water mass entering through the Strait of Gibraltar flows firstly along the coastline of Africa for arriving along the coastlines of the eastern basin and successively along the European coasts. To flow around each sub-basin in the Mediterranean this waves take about six months and this periodicity is seen at

bottom pressure from the periods in Tab. 3.10 identified as V and VI. That waves travel with the coast to the right and in the anticlockwise direction.

An investigation on the effect of wind driven circulation in Mediterranean Sea has been done (Molcard et al., 2002). The aim of this research was the explanation of large scale sub-basin gyres and their variability. It is known that there are some important permanent structures of general circulation that are the Gulf of Lions cyclonic gyre, the Rhodes gyre, the Gulf of Syrte anticyclone and it is also known that this structures are induced by permanent wind stress curl structures. The variability of wind is also important to determine the presence or not of Tyrrhenian anticyclonic gyre, Balearic anticyclonic gyre and Ionian cyclonic gyre. In the cited article it has been found that interannual variability of wind-forcing changes the amplitude and the phase of the seasonal cycle in the sub-basin scale gyres and boundary currents. The process of adjustment to winds produces a train of coastally gravity waves that travel around the eastern and western basin respectively in about 6 months.

The signal VIII has a periodicity of 343 days. It is supposed to be a tidal component that the filter didn't remove. The long periods, in fact, are more difficult to identify especially on short series as the astronomy influence is not the only factor that shape the wave.

An interesting result comes from the presence of a period of 14 months (IX). This period has been conferred to the Chandler wobble. Chandler wobble is a deviation of the Earth's axis of rotation of about 9 meters and with a period of about 14 months. This effect is due to the oscillation of the geoid causing a redistribution of the weights. In particular, the Chandler wobble is excited by a combination of atmospheric and oceanic processes and a great role is played by the ocean bottom pressure fluctuations. A study has been done (Gross, 2000) to demonstrate the effective importance of bottom pressure fluctuations. It has been found for the period from 1985-1996 that Chandler wobble is firstly excited by ocean-bottom fluctuations, while the atmospheric pressure fluctuations were about half and oceanic currents has only a minor effect. Atmospheric wind were out-of-phase with the pressure terms and they reduces the Chandler wobble effect. This contributor have a power comparable with the other contributors, such as steric effect. It can be considered to play an important role in the bottom pressure fluctuations and a term to be studied in the next future thanks to the availability of always more data of bottom pressure.

Chapter 4

Analysis of model results

4.1 Reanalysis

, The time series RTS from ANTARES Observatory has been compared with the model data provided by the NextData archive. The latter contains a Reconstruction/Reanalysis (RR) of the physical state variables of the Mediterranean Sea. The reanalysis uses all the historical marine data from 1912-2011 and a model to interpolate between them the RR has been produced for the period 1955-2012.

In situ temperature and salinity observations profiles and remote sensed observations of altimetry have been assimilated by a numerical Ocean General Circulation Model (OGCM). The OGCM has a domain on the whole Mediterranean Sea extending also in the Atlantic with an horizontal resolution of 1/16th of degree and 72 unevenly spaced vertical z-levels. The resolution of the grid is $0.0625'$ that means 7 km. Daily data are provided for 3D fields of temperature, salinity and horizontal velocity components.

4.2 Calculation of bottom pressure

The data of potential temperature and salinity provided by the RR have been subsampled in a rectangle ranging from 41-45.937°N, 4-8°E and for the period from 1 January 2009 to 31 December 2013.

The RR data are used to calculate pressure at the bottom near the ANTARES Observatory the first step is to calculate density and subsequently calculate pressure.

The selected subgrid has $80 \times 65 \times 72$ points, respectively the latitude, the longitude and the depth levels. The density has been calculated at every grid point with the UNESCO seawater formula from WHOI.

Having density, it is possible to calculate pressure at the chosen depth levels at the nearest point to the ANTARES coordinates (42°47.935′N, 06°09.942′E, 2478 m). Three grids have been selected to do an average of the pressure from the model, two composed of 9 grid-points and one composed of 16 grid-points.

Fig. 4.1 shows the three averaging grids.

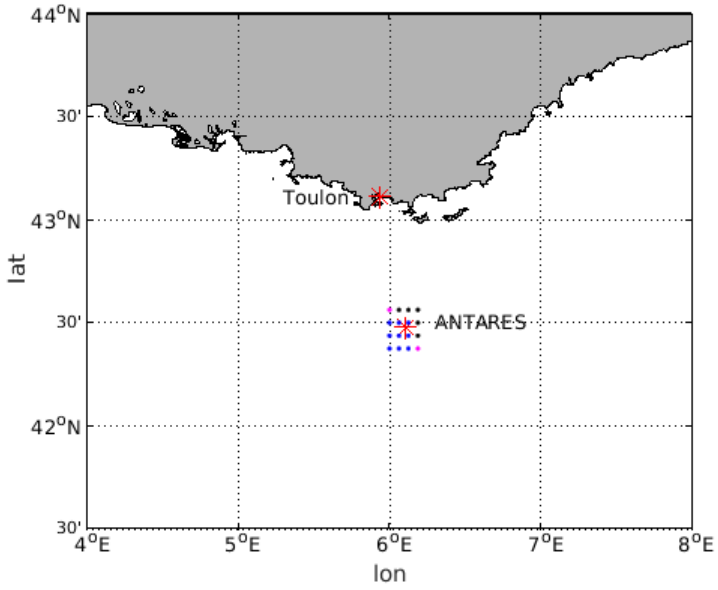

Figure 4.1: ANTARES central point and three different grids used for the average of the model results.

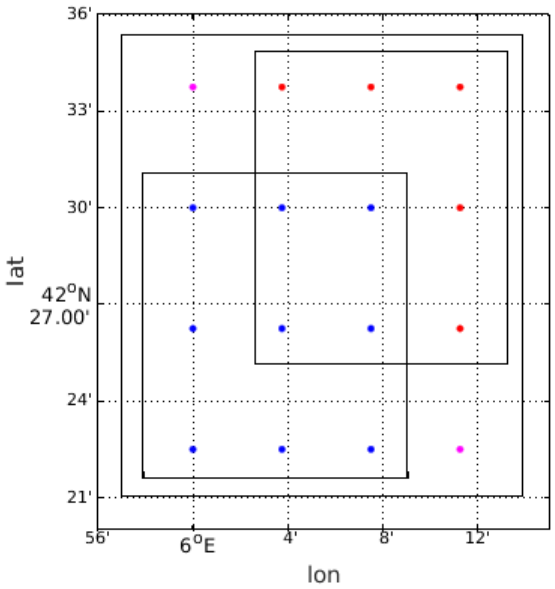

Figure 4.2: Disposition of the three grid-points. The blue points represent G1, the added red points G2 and the big square represents G3. ANTARES stands in the intersection.

Pressure is calculated through the hydrostatic equation introduced in Sec. 1.2.3, Eq. 1.6.

Since the model doesn't consider the atmospheric pressure, the pressure calculation is done only with

$$p(-H) = \rho_0 g\eta + g\int_{-H}^{0} \rho dz' \tag{4.1}$$

The series obtained from the model pressure presented a trend that has been removed (Fig. 4.3).

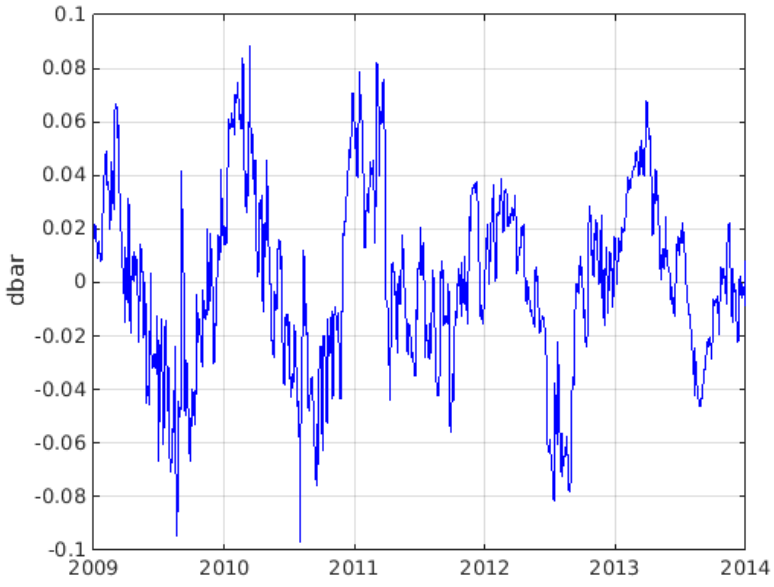

Figure 4.3: Detrended model series of the G1 grid from 1 January 2009 to 31 December 2013.

In agreement with the observed RTS, the model series takes a period from 2 January 2009 to 30 December 2013. The model and RTS dataset have been filtered by a 15 days running mean. This has lead to a further shortening of the series that now starts on the 17 January 2009 and ends on the 15 December 2013.

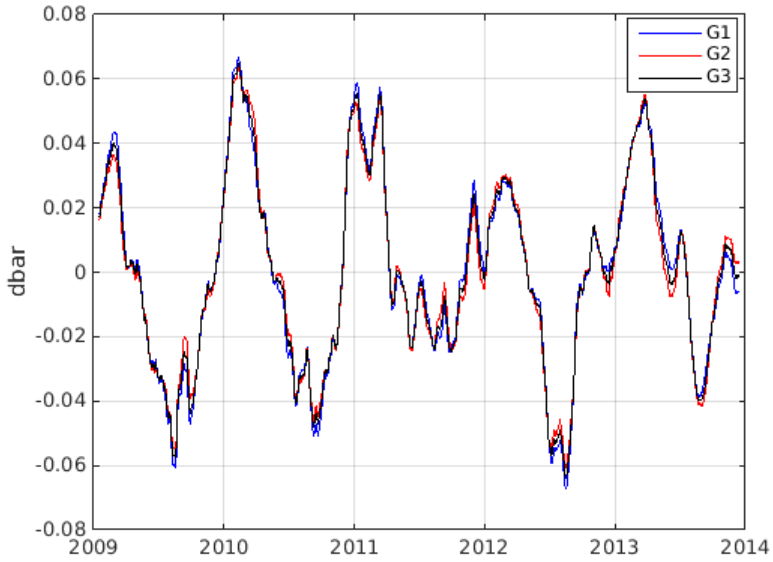

Figure 4.4: Overlay of the three data series of pressure calculated from model referring to grid G1, grid G2 and grid G3.

In Fig. 4.4 the comparison of the detrended and filtered time series is shown. The conclusion is that the three time series do not show significant differences and thereafter the one on the G1 grid will be selected.

4.2.1 Relationship between depth and pressure

The forces acting on the water column are the gradient of pressure and gravity: The downward force of gravity is balanced by an upward pressure gradient force. This means that pressure increases with depth and the balance between the two forces, with no motion, is the hydrostatic balance. The pressure at a given depth depends on the mass of water which is above it and it is commonly demonstrated that there is an increase of 1 dbar every 1 m of depth for water. This is true until a depth of about 990 m. Below that level the relation between pressure and depth change due to the compressibility of water.

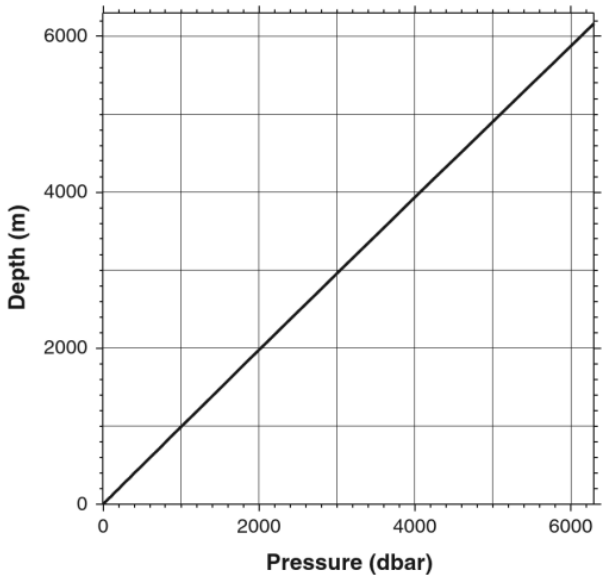

Figure 4.5: Relation between depth and pressure [L. Talley,Descriptive Physical Oceanography].

Pressure(dbar)	Depth(m)	Difference(%)
0	0	0
100	99	1
200	198	1
300	297	1
500	495	1
1000	990	1
1500	1453	1.1
2000	1975	1.3
3000	2956	1.5
4000	3932	1.7
5000	4904	1.9
6000	5872	2.1

Table 4.1: $Percent\,difference = (pressure - depth)/pressure \times 100$ [L. Talley,Descriptive Physical Oceanography].

Position	depth	unit of measure
ANTARES pressure sensor	2478	m
RTS values	2509	dbar
Model level (60)	2448,2	m

Table 4.2: Depth of ANTARES pressure sensors, pressure value deduced from RTS and depth of the model level.

The pressure sensor by ANTARES is positioned at a depth of 2478 m, while the observational value of pressure is 2.509 m as deduced from the detrending done in Sec. 3.5.2. The difference between the depth of the sensor and the value of pressure measured is 31 m, that means 1.24% of difference that is due to the compressibility of water. The model level is chosen instead to be the closest to the pressure sensor depth.

4.3 Intercomparison of model results to observed data

It is now possible to compare the observed ANTARES pressure data and the model calculated pressure.

An overlay of the calculated model series with the observed series in Fig. 4.6, 4.7, 4.8, 4.9, 4.10 is shown.

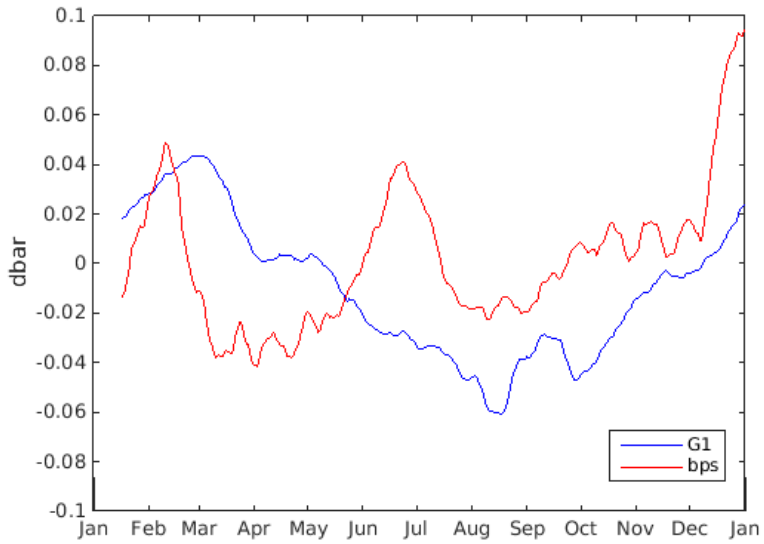

Figure 4.6: Overlay of G1 grid and observed data in 2009 starting from the 17 January 2009.

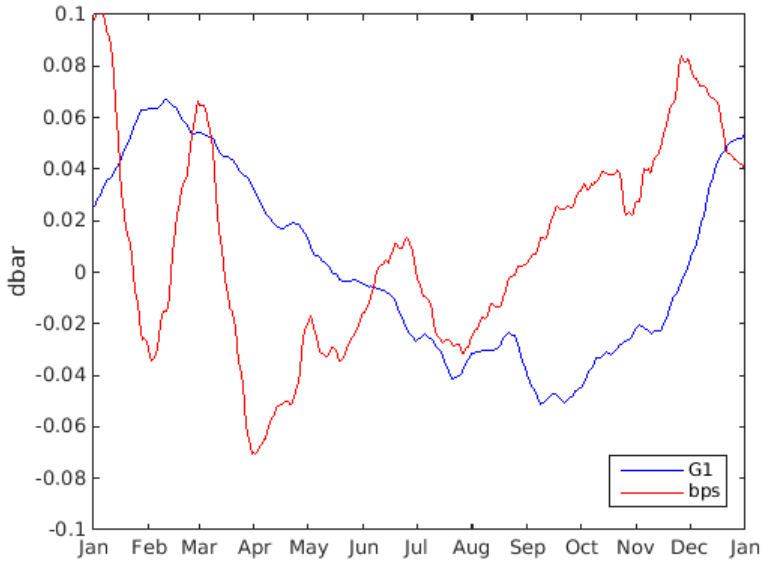

Figure 4.7: Overlay of G1 grid and observed data in 2010 starting from the 1 January 2010.

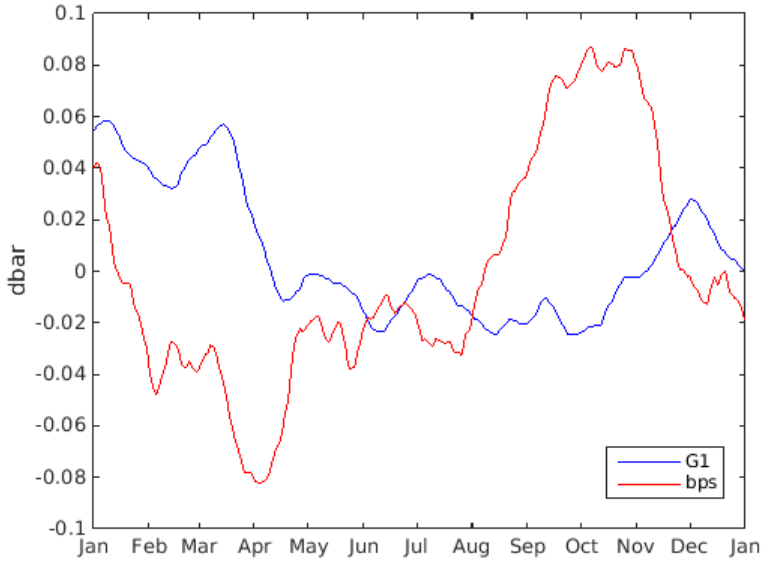

Figure 4.8: Overlay of G1 grid and observed data in 2011 starting from the 1 January 2011.

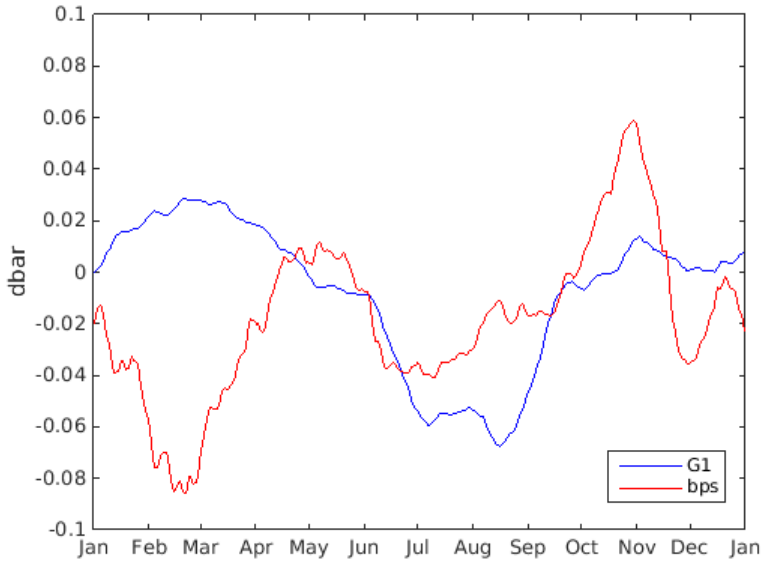

Figure 4.9: Overlay of G1 grid and observed data in 2012 starting from the 1 January 2012.

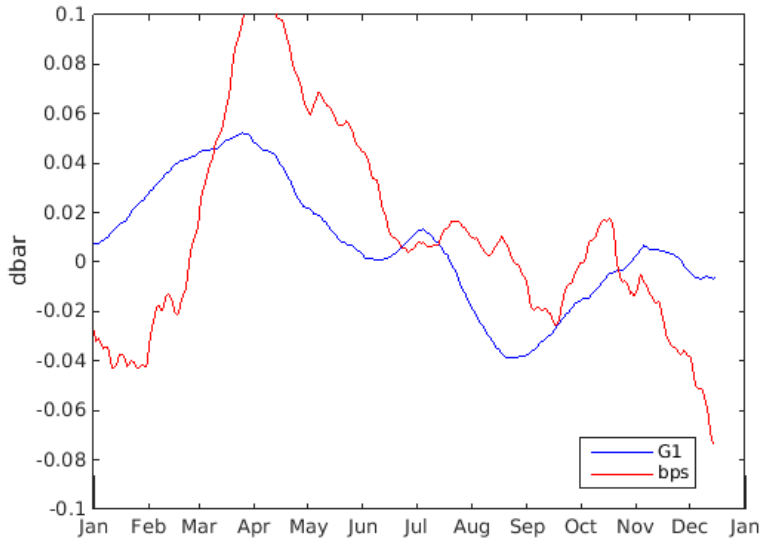

Figure 4.10: Overlay of G1 grid and observed data in 2013 starting from the 1 January 2013 and ending the 15 December 2013.

The series show a low correlation in general depending on the year.

The Pearson correlation coefficient between the two series for all of the five years is 0.0700. It is necessary to divide the series in shorter intervals and compare the

observed data to the model data in order to extract some correlation. Four sub-intervals of three months for each year have been selected. The first period contains January, February and March (winter). The second April, May and June (spring). The third July, August and September (summer) and the last one comprehends October, November and December (autumn).

Season	Intervals	2009	2010	2011	2012	2013
Winter	Jan-Feb-Mar		-0.3098	0.6087	-0.7618	0.8302
Spring	Apr-May-Jun	-0.9491	-0.9092	-0.6295	0.6630	0.8813
Summer	Jul-Aug-Sep	0.4728	-0.6208	-0.5611	0.6223	0.4975
Autumn	Oct-Nov-Dec	0.7249	0.4474	-0.8043	0.3887	

Table 4.3: Pearson correlation coefficients for the correlation of model data and observed data for the three months interval, winter, spring, summer and autumn. The first and the last intervals have been eliminated because the three months were not complete. The 95% significance level is reached for correlation values $> \pm 0.20$.

RMSD between the observed and model time series is 0.05 dbars. Taking the absolute value of the range from Fig. 4.6 equal to 0.01 dbar it is clear that the RMSD is 50% of the overall signal. It is interesting to note that the two time series are anti-correlated in 2010-2011, spring and summer. Thus make conclude that it is not yet possible to use the model to interpret the data. However for the sake of completeness the model output will be analyzed to better understand the variability around ANTARES.

4.4 Temperature, salinity and density

As in the case of pressure it has been applied a mean on the nine point of the grid G1 (longitude from 6 to 6.1250 E and latitude from 42.3750 to 42.5000 N) on temperature and salinity. The mean has been done at the nearest level to ANTARES depth (2.448,2 m). The data set has been displayed in function of the time from 17 January 2009 to 15 December 2013. Temperature and salinity values are extracted directly from the reanalysis model.

All the three series showed a trend that has been removed and a mean have been done:

$$T' = T - \langle T \rangle \, ; \; S' = S - \langle S \rangle \, ; \; \rho' = \rho - \langle \rho \rangle \, ; \; p' = p - \langle p \rangle \, ; \tag{4.2}$$

Intercomparisons between the values of temperature, salinity and pressure have been done.

The intercomparison between temperature and salinity for the 5 years in Fig. 4.11 shows a correlation of 0.4073. Dividing in sub-intervals, the years 2009, 2010, 2011 show high correlation of 0.7898. Anti-correlation takes place in 2012 and 2013 with values of -0.3933.

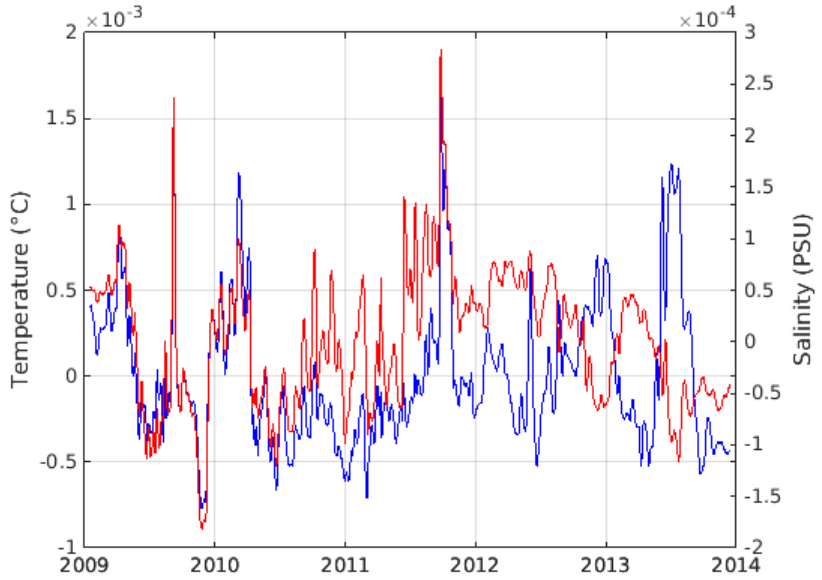

Figure 4.11: Intercomparison between the mean temperature and the mean salinity as a function of time for the bottom level at 2448 m on the area identified as G1. The blue line represents the temperature and the red line represents the salinity.

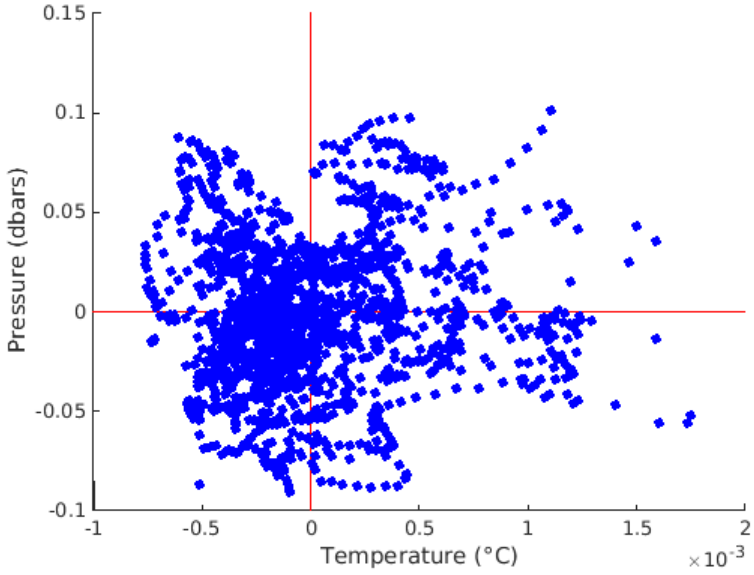

Figure 4.12: Scatter-plot of the model pressure and the temperature in grid G1 at the bottom.

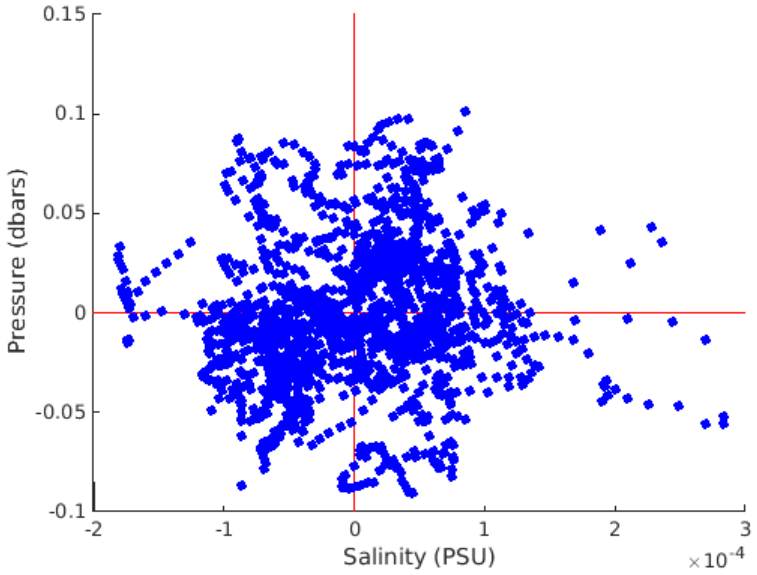

Figure 4.13: Scatter-plot of the model pressure and the salinity in grid G1 at the bottom.

4.5 Model temperature, salinity and currents

The aim is now to map the variability near the ANTARES Observatory for temperature, salinity and currents at different depths. The model provides 60 useful levels of data above 2448 m and it is necessary to select some significant levels. To decide what level are significant, mean profiles of temperature and salinity have been computed.

4.5.1 Mean temperature and mean salinity time series

The temporal mean of temperature and salinity profiles are shown in Fig. 4.14, 4.15, 4.16 and 4.17. Fig. 4.14 shows the mean over three months intervals over the temperature and each year. Secondly a climatological mean has been computed and it is shown in Fig. 4.15. Fig. 4.16 shows the mean over three months intervals over the salinity and each year. Secondly a climatological mean has been computed and it is shown in Fig. 4.17.

The next figures represent the temporal evolution of temperature and salinity. The climatological mean, done over five years, is also represented.

Figure 4.14: Three months mean of T from 2009 to 2013. All the 60 depths for grid G1 are represented. The lower and more constant values correspond to the bottom layers. The higher and more variable values correspond to the top layers.

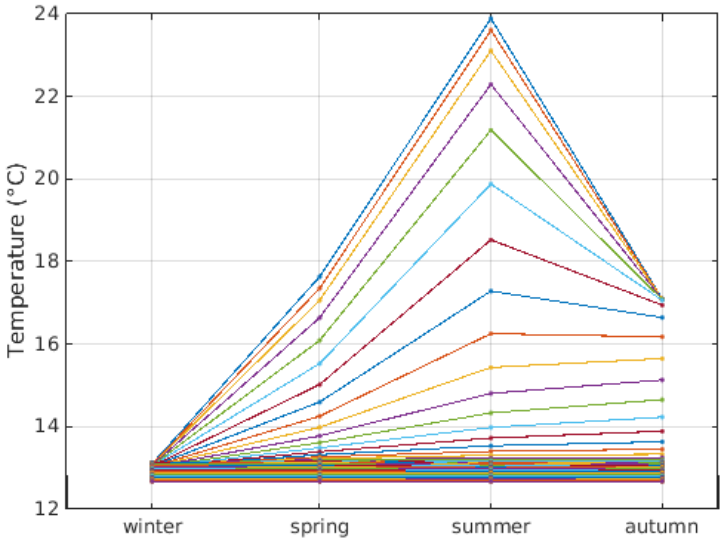

Figure 4.15: Three months climatological mean of T from 2009 to 2013. All the 60 depths for grid G1 are represented. The lower and more constant values correspond to the bottom layers. The higher and more variable values correspond to the top layers.

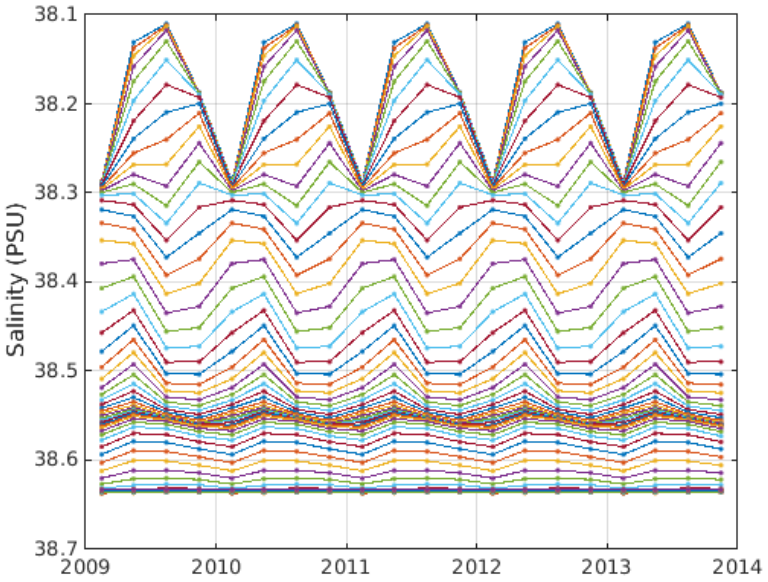

Figure 4.16: Three months mean of S from 2009 to 2013. All the 60 depths for grid G1 are represented. The higher and more constant values correspond to bottom layers. The lower and more variable values correspond to the top layers.

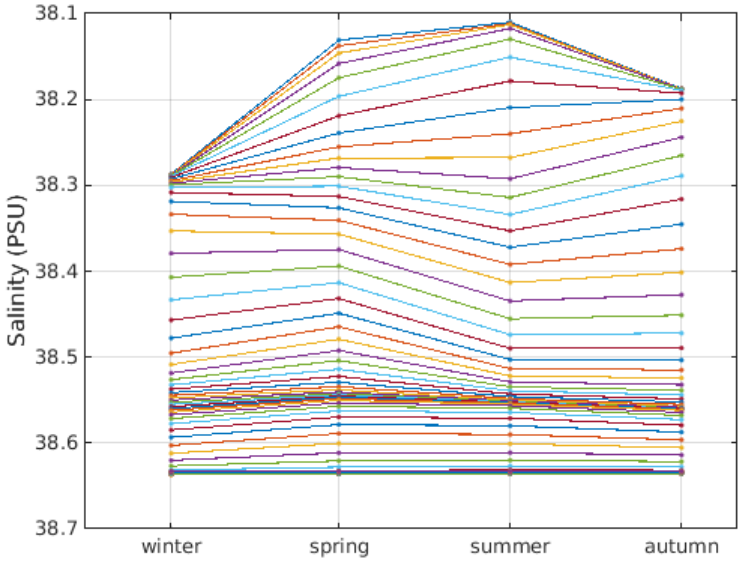

Figure 4.17: Three months climatological mean of S from 2009 to 2013. All the 60 depths for grid M1 are represented. The higher and more constant values correspond to bottom layers. The lower and more variable values correspond to the top layers.

It is interesting to note the strong dependence of the surface water from the seasons. The temperature fluctuates from values around $13°C$ in autumn and winter to maximum values of $24°C$ in summer. The water temperature at the bottom oscillates around $13°C$ without strong variations. Three levels have been identified: the first from the surface to 24 m of depth, strongly influenced by the atmosphere, the second, from 24 to 74 m where the thermocline develops almost constant throughout the year. The salinity has this strong dependence too. A minimum of salinity is expected in summer with values of 38.1 PSU (the so-called Atlantic Water) and an increase toward the bottom is seen up to 38.6 PSU. For salinity it is possible to identify three layers as well: the first, strongly influenced by the atmosphere, from the surface to 66m. The second layer, weakly influenced by the atmosphere, from 66 to 366 m. The bottom layer that is not influenced.

4.5.2 Vertical profiles

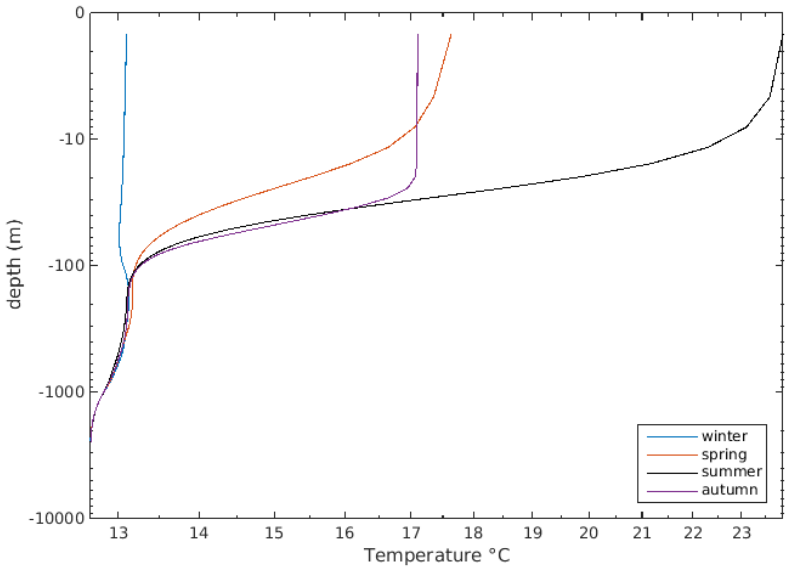

Figure 4.18: Vertical profile of T, time averaged from 1 the January 2009 to the 31 December 2013. Climatological means for winter, spring, summer and autumn are represented.

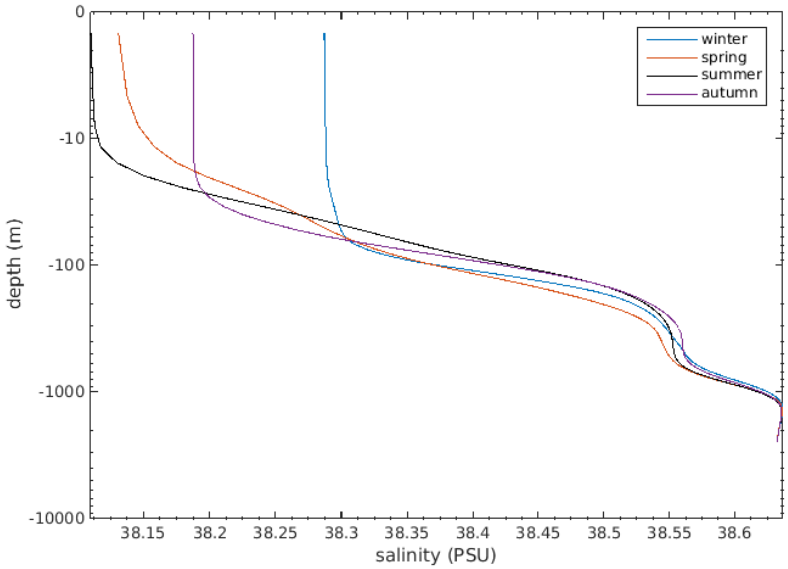

Figure 4.19: Vertical profile of S, time averaged from 1 the January 2009 to the 31 December 2013. Climatological means for winter, spring, summer and autumn are represented.

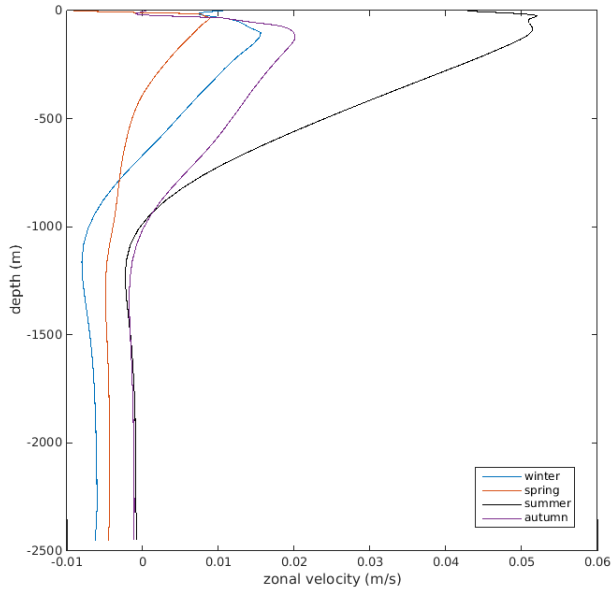

Figure 4.20: Vertical profile of zonal velocity, time averaged from 1 the January 2009 to the 31 December 2013. Climatological means for winter, spring, summer and autumn are represented.

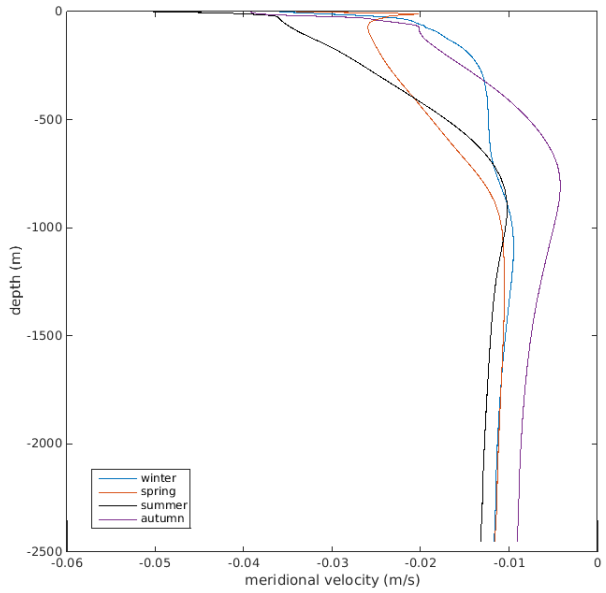

Figure 4.21: Vertical profile of meridional velocity, time averaged from 1 the January 2009 to the 31 December 2013. Climatological means for winter, spring, summer and autumn are represented.

Observing the vertical profiles of temperature and salinity one can identify in the seasonal thermocline until a depth of about 100 m that layer in which temperature and salinity balance each other. In the deep thermocline and transitions water the advective component is predominant.

Climatological means have been done for zonal velocity, meridional velocity and density as well and the vertical profiles have been represented. The zonal and the meridional velocities are uniform from a depth of about 1000 m until the sea-floor.

4.5.3 Oceanographic conditions around ANTARES

For every layer of the column it is now possible to do maps to describe the distribution of temperature and salinity and the associated velocities. It is plausible to think that intervals where high correlation is found, are that intervals in which the model better describes the situation. For that reason one map for each season in that intervals have been done. For each season the one with higher correlation has been chosen. From Tab. 4.3

	INTERVAL	SEASON	CORRELATION
C1	Oct-Nov-Dic 2009	autumn	0.7249
C2	Jan-Feb-Mar 2013	winter	0.8302
C3	Apr-May-Jun 2013	spring	0.8813
C4	Jul-Aug-Sep 2012	summer	0.6223

Table 4.4: Intervals of the grid G1 with higher correlation with the observed data.

Maps at the bottom for each season are represented.

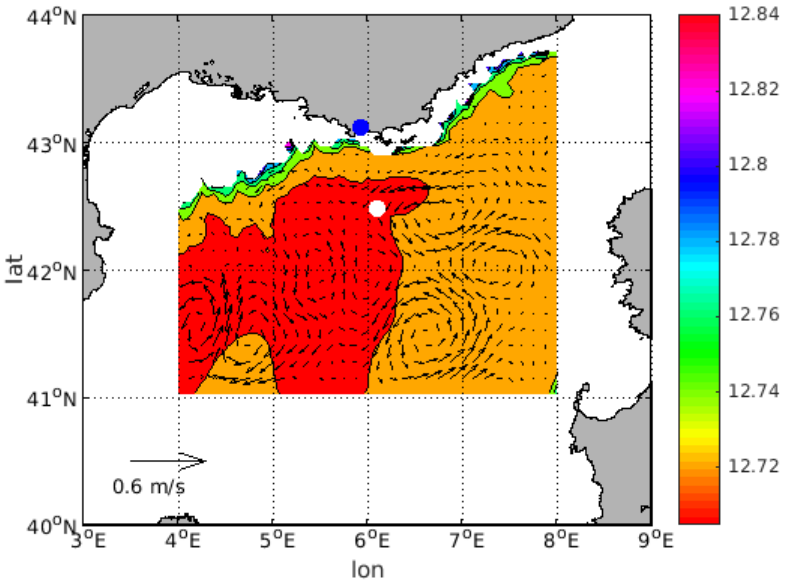

Figure 4.22: Map of temperature (°C) and velocity (m/s) in autumn 2009 for the period C1 at the bottom.

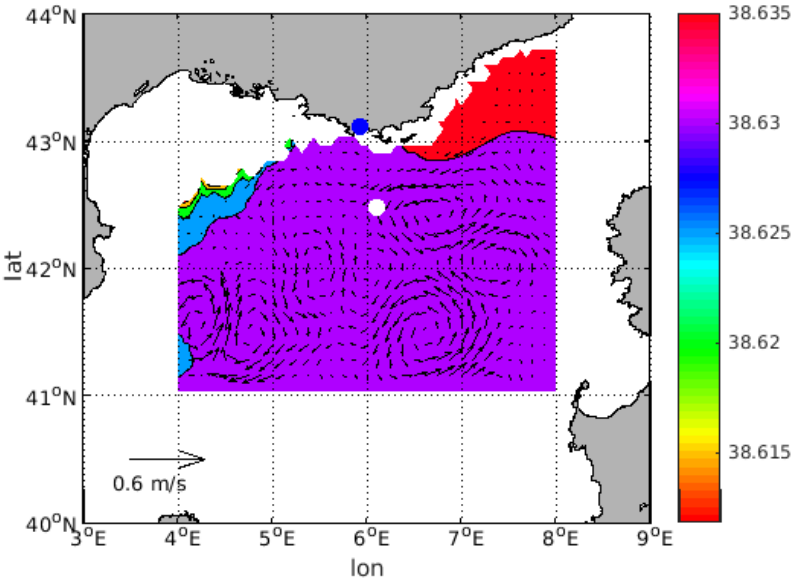

Figure 4.23: Map of salinity (PSU) and velocity (m/s) in autumn 2009 for the period C1 at the bottom.

The map of autumn shows that the ANTARES Observatory is at the boundary of a cyclone. The intensity of the velocity is less than 0.1 ms^{-1}. The temperature

is about 12.70 $°C$ with a salinity spatially constant of 38.63 PSU.

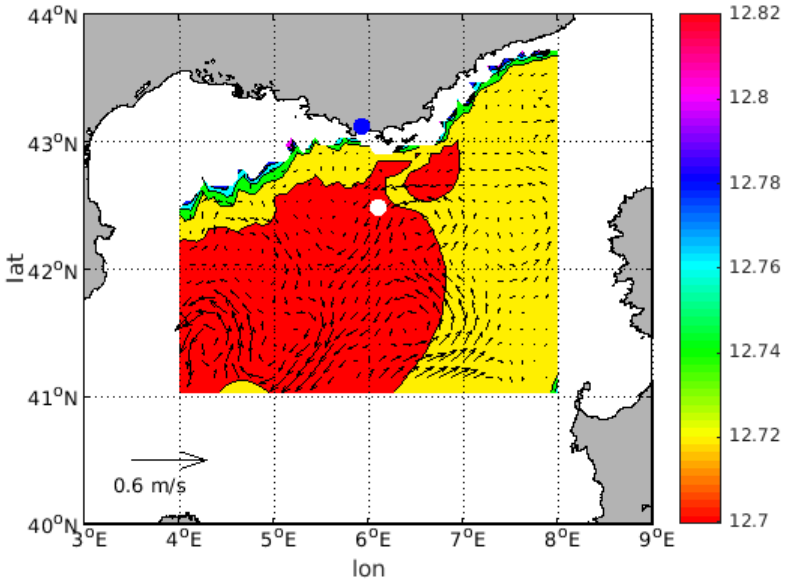

Figure 4.24: Map of temperature (°C) and velocity (m/s) in winter 2013 for the period C2 at the bottom.

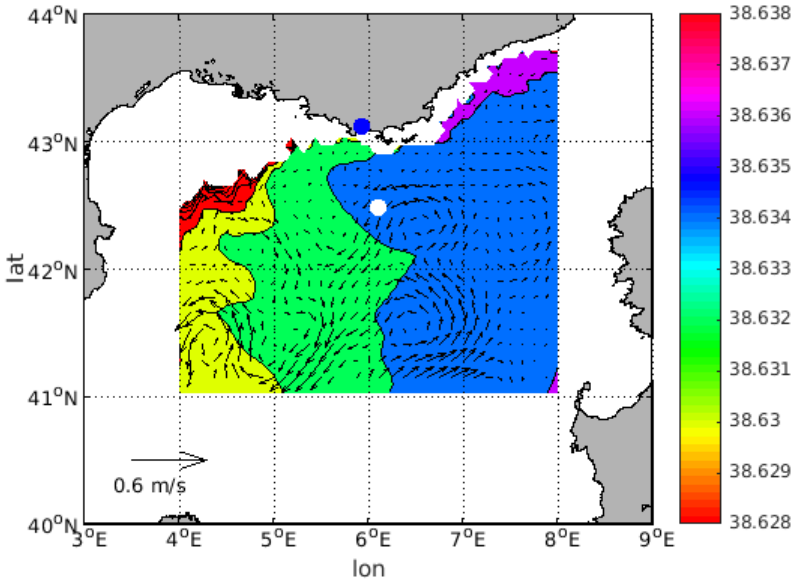

Figure 4.25: Map of salinity (PSU) and velocity (m/s) in winter 2013 for the period C2 at the bottom.

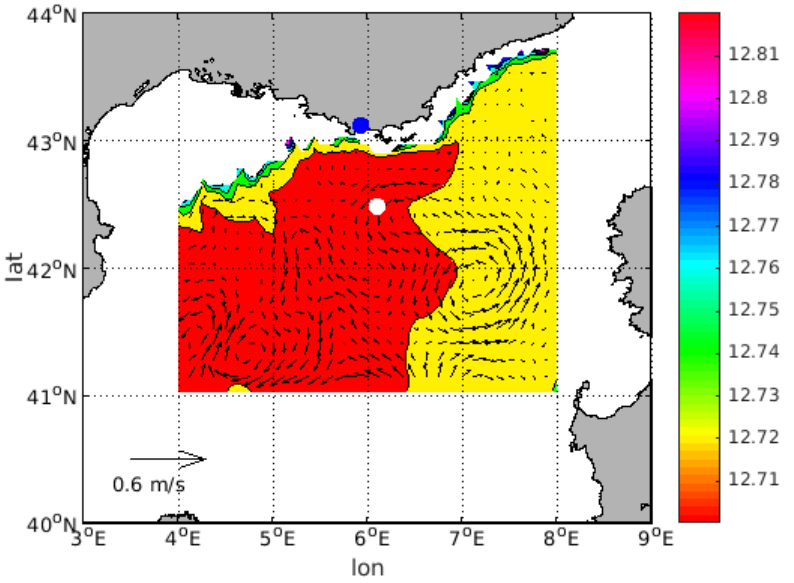

Figure 4.26: Map of temperature (°C) and velocity (m/s) in spring 2013 for the period C3 at the bottom.

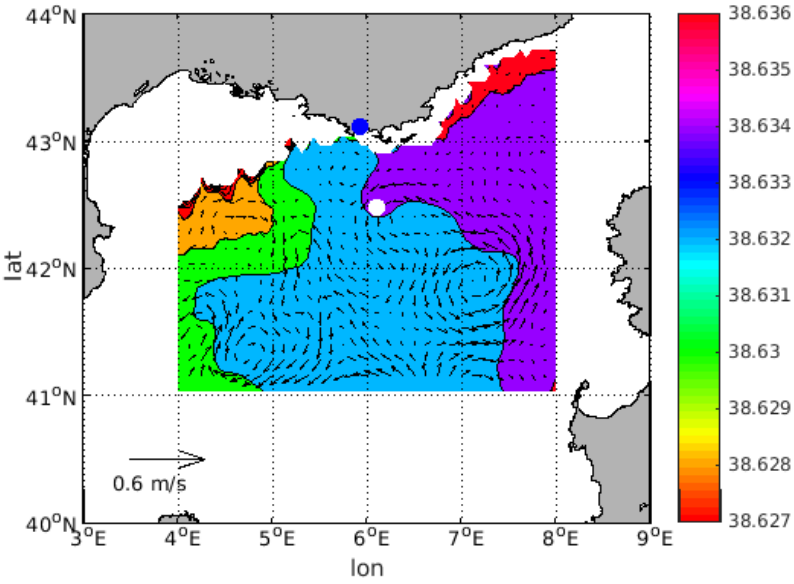

Figure 4.27: Map of salinity (PSU) and velocity (m/s) in spring 2013 for the period C3 at the bottom.

In winter and spring the ANTARES Observatory is again at the border of a cyclone.

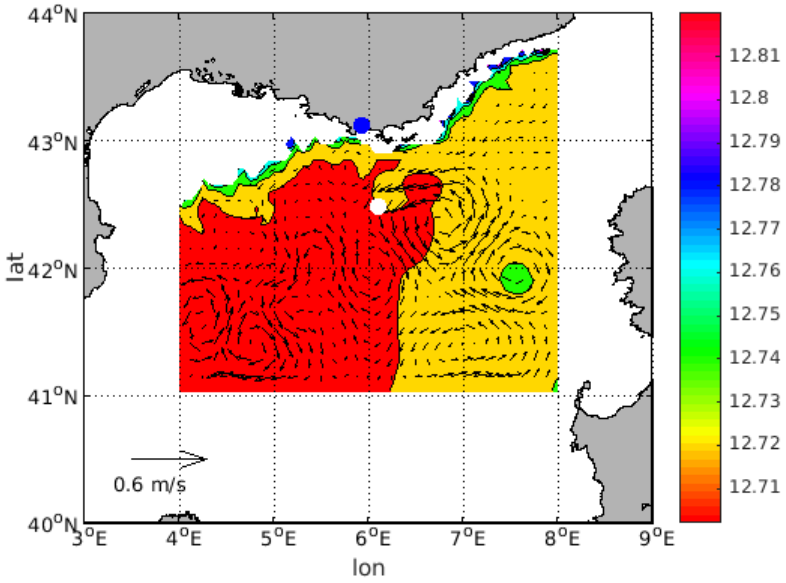

Figure 4.28: Map of temperature (°C) and velocity (m/s) in summer 2012 for the period C4 at the bottom.

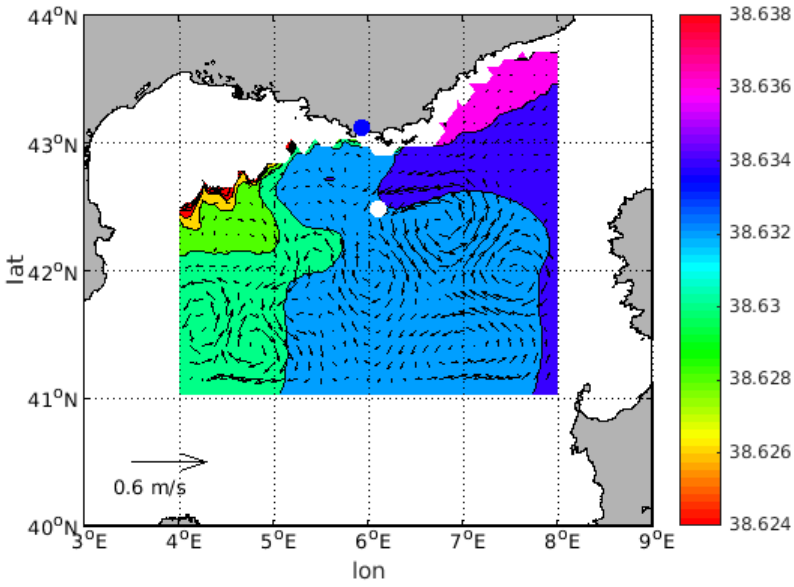

Figure 4.29: Map of salinity (PSU) and velocity (m/s) in summer 2012 for the period C4 at the bottom.

In summer ANTARES is again at the boundary of a cyclone that is stronger than in the other seasons.

All these maps show that ANTARES is located in an area in the Mediterranean Sea strongly influenced by the eddies. The eddy variability in space and time is high and in the maps it is shown that the cyclones and anticyclones are coupled. Their motion is dominant and they distribute along the path of the Liguro-Provencal current. In Fig. 4.30 the circulation structure in the Mediterranean Sea shows the dominance of the Gulf of Lion Gyre and the Liguro-Provencal-Catalan Current near the ANTARES observatory.

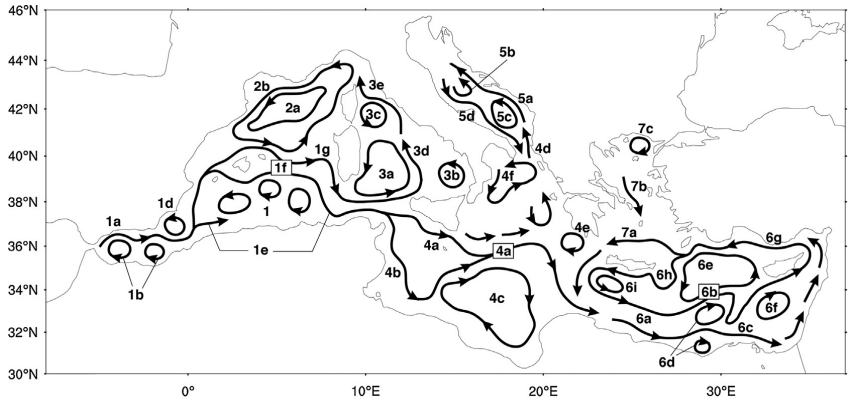

Figure 4.30: Mean surface circulation structure. The system 2a and 2b represent respectively the Gulf of Lion Gyre (GLG) and the Liguro-Provencal-Catalan Current (LPCC) (Pinardi et al.,2015)

Chapter 5

Conclusions

The first result of this thesis is the development of an analysis method for the ANTARES bottom pressure time series. The raw data of L1, L3 and L8 bottom pressure sensors have been treated removing the spikes due to power outages in the cabling systems of the sensors, averaging on 30 minutes to remove the steps due to data recording and transmission and filling the gaps of one time series with the data from the complementary sensor time series where data was available. An unique series has been obtained, the Reconstructed Time Series that is used for an analysis of the bottom pressure signal. The RTS shown in Fig. 3.15, 3.16, 3.17, 3.18, 3.19 in Sec. 3.3.1 display different energy-containing frequencies and a trend that is due to the sensor drift, well documented in the literature.

In the second part of the thesis, different methods to subtract the trend from the RTS and differentiate among its different frequencies have been developed. The method developed is overviewed in 3.1.

In order to understand the nature of the different frequencies composing the sea bottom pressure, the hydrostatic equation was used. From Eq. 1.6 the bottom pressure in the ocean can be written as:

$$\underbrace{\frac{p(-H)}{\rho_0 g}}_{h_{eq}} = \underbrace{\frac{p_a}{\rho_0 g}}_{(1)} + \underbrace{\eta}_{(2)} + \underbrace{\frac{1}{\rho_0}\int_{-H}^{0}\rho(z)dz'}_{(3)} \tag{5.1}$$

where the atmospheric contribution (1) and the tidal-barotropic contribution (2) will be removed. The detiding had exactly the role to remove the high frequencies signals, that is term (1) and (2). The remaining term (3) is the Columnar Density Content, that is the contribution to the bottom pressure due to the low-frequencies phenomena.

Two methods of detiding have been applied, one averaging on three days, the other through the Doodson Filter obtaining a daily frequency. The detrending has been applied on the two detided RTS. An harmonic analysis for the detiding of the RTS detrended series has been also carried out. The presence of many gaps in the five-year data set, didn't permit to apply this method on a long enough time series. Considering the harmonic analysis as the best method of detiding, an intercomparison with three days averaged RTS and filtered RTS has been done. The filtered series is closer to the harmonic analysis time series so that the Doodson Filter is considered the best one for this analysis. A spectra has then been done to find the residual frequencies.

The signal that is left due to the contribution (3) in **??** is caused by many potential phenomena affecting the bottom pressure that are listed in Tab. 3.10 and reported here.

	PERIOD(days)	PHENOMENA
I	51	variations in the Gulf of Lion Gyre
II	57	variations in the Gulf of Lion Gyre
III	107	steric effect
IV	156	steric effect
V	172	steric effect/ Kelvin waved due to the Strait of Gibraltar
VI	191	steric effect/Kelvin waves due to the Strait of Gibraltar
VII	286	Kelvin waves due to the Straits of Gibraltar.
VIII	343	?
IX	429	Chandler wobble

Table 5.1: List of significant phenomena in the observed bottom pressure at the ANTARES observatory. (For reference to Gulf of Lion Gyre see Pinardi et al., 2015)

The last chapter of the thesis has been dedicated to a preliminary analysis of the intercomparison between the bottom pressure calculated from a reanalysis data set and the observed bottom pressure signals. Even if correlation is found significant for most of the periods, overall the observed bottom pressure time series and the model do not agree sufficiently. Thus at the present time it is not possible to use the model to understand the low frequency variability signal in the Mediterranean Sea bottom pressure. Nevertheless the reanalysis deep water flow velocity, temperature and salinity field around the ANTARES observatory have been analyzed and it has been found that the Observatory is located within a very intense mesoscale eddy field, typical of the deep western Mediterranean Sea flow field.

Further analysis is required before interpreting all the signals found in the bottom pressure time series but without a numerical model it would be impossible to really understand the nature and causes of the different energy-containing signals of the bottom pressure in the Western Mediterranean Sea. Thus the priority shoud be to have a reanalysis that would better compare with the data and then have a longer time series since yearly variability is large.

One of the goals reached by this work is the evaluation of tides in open ocean for the case of the Mediterranean Sea. Open ocean is intended to be that part of the sea that starts from the bottom of the continental escarpment. It is interesting to note that it is the first time that deep water tides have been studied in the Mediterranean Sea since commonly tide gauges are positioned on the coasts.

Bibliography

[1] Eble M.C. et al., 'Instrumentation, field operations, and data processing for pmel deep ocean bottom pressure measurements', NOAA Technical Memorandum ERL PMEL-89, Pacific Marine Environmental Laboratory, Seattle (Washington), 1989, pp.7-8.

[2] Favali P. et al., 'Seafloor Observatories', Springer Praxis Books, Springer-Verlag Berlin Heidelberg, 2015, cap. 3-15.

[3] Filloux J.H., 'Pressure Fluctuations on the Open Ocean Floor Over a Broad Frequency Range: New Programme and Early Reults', Journal of Physical Oceanography, Volume 10, 1980, pp.1959-1971.

[4] Greatbatch R.J., 'A note on the representation of steric sea level in models that conserve volume rather than mass', Journal of Geophysical Research, Volume 99, 1994, pp.12,767-12,771.

[5] Gross R.S., 'The excitation of the Chandler wobble', Geophysical Research Letters, Volume 27, 2000, pp.2329-2332.

[6] Hughes C.W. et al., 'Weighing the ocean: Using a single mooring to measure changes in the mass of the ocean', Geophysical Research Letters, Volume 39, 2012, L17602.

[7] Marcos M., 'Ocean bottom pressure variability in the Mediterranean Sea and its relathionship with sea level from a numerical model', Global and Planetary Change (124), 2015, pp.10-21.

[8] Molcard A. et al., 'Wind driven general circulation of the Mediterranean Sea simulated with a Spectral Element Ocean Model', Dynamics of Atmospheres and Oceans (35), 2002, pp.97-130.

[9] Madec G. et al., NEMO ocean engine, 2016.

[10] Pawlowicz R. et al., 'Classical tidal harmonic analysis including error estimates in MATLAB usign T_TIDE', Computer & Geosciences 28, 2002, pp.929-937.

[11] Pinardi et al., 'The Mean Sea Level Equation and Its Application to the Mediterranean Sea', Journal of Climate, Volume 27, 2013, pp.442-447.

[12] Pinardi et al., 'Mediterranean Sea large-scale low-frequency ocean variability and water mass formation rates from 1987 to 2007: A retrospective analysis', Progress in Oceanography (132), 2015, pp.318-332.

[13] Talley L. et al., 'Descriptive Physical Oceanography', Elsevier, 2011, pp.29-31.

[14] Unesco, 'Algorithms for computation of fundamental properties of seawater', Unesco technical papers in marine science 44, 1983.

[15] Watts D. R., Kontoyiannis H., 'Deep-Ocean Bottom Pressure Measurement: Drift Removal and Performance', Journal of Atmospheric and Oceanic Technology, Volume 7, 1989, pp.296-306.